Alternative Bases for Gradient Based Optimization of Parameterized FM Radar Waveforms

By
Bahozhoni White

Submitted to the graduate degree program in Electrical Engineering and Computer Science and the Graduate Faculty of the University of Kansas in partial fulfillment of the requirements for the degree of Master of Science.

Dr. Shannon Blunt, Chairperson

Committee Members

Dr. Christopher Allen

Dr. James Stiles

Date defended: _____

This work was supported by the Office of Naval Research under Contract #N00014-20-C-1006.

The thesis committee for Bahozhoni White certifies that this is the approved version of the following thesis:

Alternative Bases for Gradient Based Optimization of Parameterized FM Radar Waveforms

Dr. Shannon Blunt, Chairperson

Date approved: _____

Abstract

Even for a fixed time-bandwidth product there are infinite possible spectrally-shaped random FM (RFM) waveforms one could generate due to their being phase-continuous. Moreover, certain RFM classes rely on an imposed basis-like structure scaled by underlying parameters that can be optimized (e.g. gradient descent and greedy search have been demonstrated). Because these structures must include oversampling with respect to 3-dB bandwidth to account for sufficient spectral roll-off (necessary to be physically realizable in hardware), they are not true bases (i.e. not square). Therefore, any individual structure cannot represent all possible waveforms, with the waveforms generated by a given structure tending to possess similar attributes. Unless of course we consider over-coded polyphaser-coded FM (PCFM), which increases the number of elements in the parameter vector, while maintaining the relationship between waveform samples and the time-bandwidth product. Which presents the potential for a true bases, if there is a constraint either explicit or implicit that will constrain the spectrum. Here we examine waveforms possessing different attributes, as well as the potential for a true basis which may inform their selection for given radar applications.

Acknowledgements

I'm forever thankful for the opportunities provided to me by my professors here at the University of Kansas. Thank you Dr. Salandrino and Dr. Stiles for not only being amazing educators, but for seeing my potential and providing me with the connections to continue my education. Thank you Dr. Blunt for all the support and guidance you have provided and of course for waving the wheat with me. As well as all the other students at the lab, I appreciate all of you for always being available to ask questions.

I also have to extend thanks to my family for all of the prayers, love, and unwavering support they have provided throughout this journey. Thank you little edamame for always providing a listening ear during stressful times and for being my biggest cheerleader during the good. Thank you dad for the engineering mind and all your prayers. Thank you to my brothers for making sure I was tough. Lastly, thank you Anthony for your encouragement, laughter, and love. I appreciate you all greatly. This work was supported by the Office of Naval Research under Contract #N00014-20-C-1006. DISTRIBUTION STATEMENT A. Approved for Public Release.

Contents

List of Figures

Chapter 1 Introduction

1.1 Radar Background

Radar was developed in the early 1900s independently by several different countries [1,2,3]. By 1922 the Naval Research Laboratory, was using radar to detect wooden ships on the Potomac and would accidentally detect aircraft by 1930. Radar, which is an acronym for Radio Detection And Ranging, sends out a signal and listens for an echo or reflection from a target. Using the reflected signal and various processing techniques, the target location and velocity can be determined. From the 1930's, radar technologies has improved leaps and bounds spreading their use across a variety of applications. This led to an increase in popularity over the years, from being used by law enforcement for traffic radars to various applications in sports. As a result most people know what radars are, but they do not know the complicated concepts and technologies composing the system. Therefore, the goal of this chapter is to introduce the necessary background information in order to assist the reader in understanding the topic of this thesis.

1.2 Radar Ranging

Beginning with the basics of radar, for a monostatic radar operating in a pulsed-Doppler mode the radar will transmit a signal and listen for a reflection from a target. The range from the radar to the target can be determined by the roundtrip travel time, τ_o it takes the signal to travel there and back [2,3],

$$R_o = \frac{c\tau_o}{2}, \tag{1.1}$$

where the signal, due to electromagnetics, propagates at the speed of light, $c \approx 3 \times 10^8$ m/s. But what about the case where there are multiple targets? For two targets, that are at R_o and R_1, the reflected signal would return still at time τ_o from the first target and the return from the second target would arrive at τ_1. While this seems simple, there are other factors to consider here, such as

how far the targets are spaced apart and what the pulse duration is. In Figure 1-1, the scenario described above is depicted,

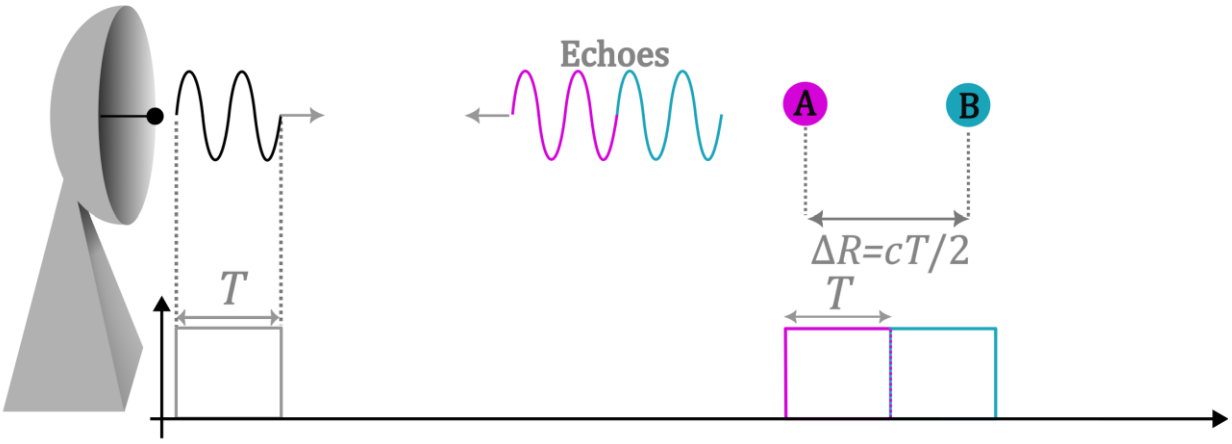

Figure 1-1: Radar reflection from two point targets

If the targets are in close enough proximity, the reflected signals may overlap in time, causing them to interfere with each other. The radar's ability to resolve two targets within close proximity is known as *range resolution* ΔR, from the definition in (*1.7*), we see ΔR is related to the pulse width T, or also inversely the signal bandwidth B,

$$\Delta R = \frac{cT}{2} = \frac{c}{2B}, \tag{1.2}$$

Being a monostatic radar operating in a pulsed mode, there are some impediments that we must consider. Operating in a pulsed mode implies that at a set interval the radar transmits a signal, this is known as the *pulse repetition interval* T_{PRI}. Due to T_{PRI} there is a *maximum range*, defined in (1.3), a target may be from the radar. Every T_{PRI} a new pulse is being sent out, the reflection from the target must return before the next pulse or else it will be considered ambiguous. Therefore, an ambiguous target will appear as if it is closer to the radar system than it really is, this scenario is illustrated in Figure 1-2. As stated previously, there have been a lot of improvements in radar since the 1930's and that includes the disambiguation of targets.

$$R_{max} = \frac{cT_{PRI}}{2}. \tag{1.3}$$

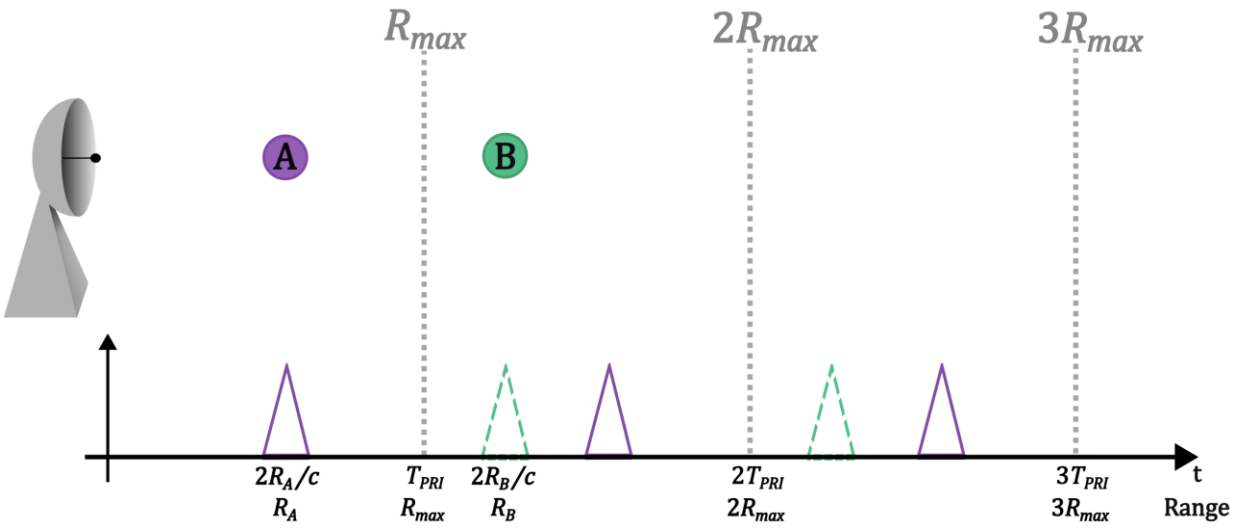

Figure 1-2: Radar reflection from a point target within R_{max} and a point target beyond

1.3 Signal-to-Noise Ratio

When the radar emits a signal, it is not the only electromagnetic signal that is propagating through free space. Once the reflected signal is received, it will have interacted with other electromagnetic waves, such as noise. There are different types of noise and noise sources, for example cosmic noise spawns in outer space, solar noise generated by the sun, and thermal noise. Typically, the main culprit corrupting the reflected signal is thermal noise. Thermal noise stems internally from the receiver itself due to the random movement of thermally charged electrons. Since the noise is considered a random signal due to the randomly varying amplitude and phase, it is uncorrelated sample to sample and uncorrelated with the received signal. Therefore, the signal power and noise power add to determine the total power.

The ability to accurately detect targets is dependent on the *signal-to-noise ratio* (SNR). The higher the signal power relative to the noise power, the higher the SNR, which facilitates the detection and

keeps *false alarms* to a minimum. As seen in Figure 1-3, as the noise power increases the underlying transmitted signal becomes harder to distinguish,

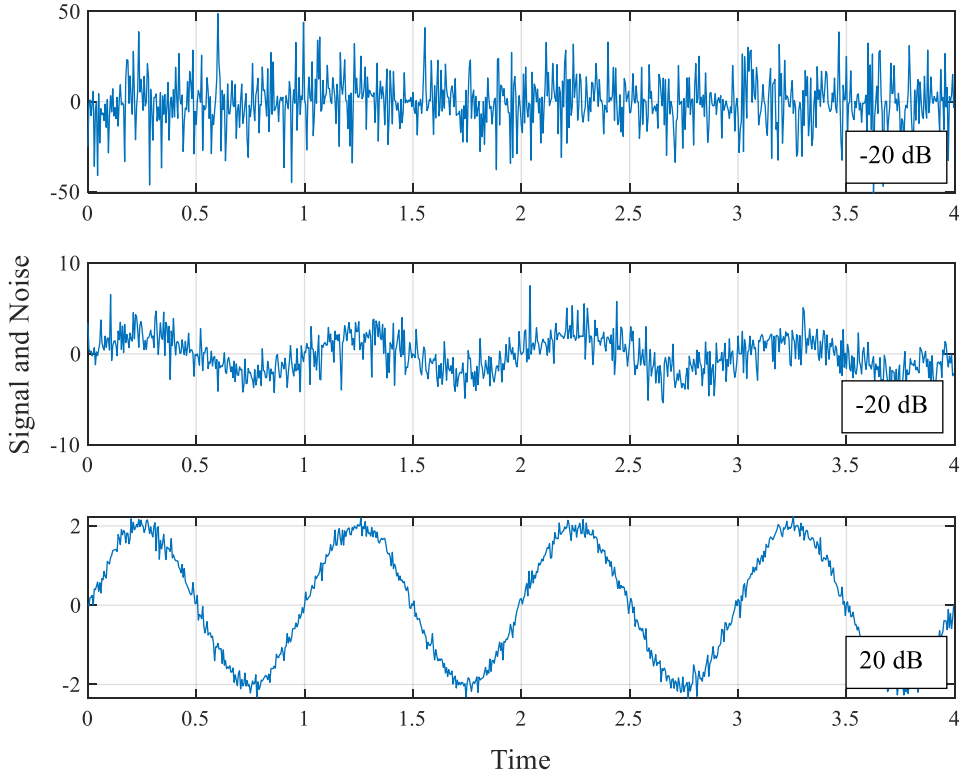

Figure 1-3: Different noise powers and effect on the *signal-to-noise ratio* (SNR)

While the SNR is simply the received signal power to the noise power, there is a little more to calculating the power ratio than that. The received power is derived from the *radar range equation*, which considers transmitted power P_t, antenna gain(s) G_t, carrier wavelength λ_c, target *radar cross section* (RCS) σ, and the target range R. Due to noise being uncorrelated sample to sample, the thermal noise power can be taken as uniformly distributed over the operating bandwidth. Thus the SNR for a monostatic radar can be calculated as,

$$SNR = \frac{P_r}{P_n} = \frac{P_t\, G_t^2\, \lambda^2\, \sigma}{(4\pi)^3 R^4\, kT_o FB}, \tag{1.4}$$

where $k = 1.38 \times 10^{-23}$ J K^{-1} is *Boltzmann's constant*, $T_o = 290\ K$ is the absolute temperature, and F is the receiver *noise figure*.

For a radar system that has poor SNR, there are options to make improvements the easiest being to increase the transmitted power. Conceivably by increasing the pulse duration T, the transmitted power is also increased, but this is at the cost of range resolution. Thankfully, there are other options to increase the transmit power, which will be discussed shortly. From (1.4) we can infer other options to increase SNR, one could increase the antenna gain G, decrease the target range R, decrease the noise figure F, decrease the receiver bandwidth B, or change the operating frequency. While these are potential options, their feasibility is questionable as they may require changes in hardware or adversely affect performance elsewhere.

1.3.1 Pulse Integration

As discussed previously, there is another option to increase the transmit power without adversely affecting ΔR. When the radar is operating in a pulsed mode, the transmitted energy can be increased by emitting more pulses [1,2]. Processing of the received pulses is then performed through coherent, noncoherent, or binary integration. For this thesis, only coherent and noncoherent integration will be discussed. Coherent integration utilizes the amplitude and phase information from the individual pulses to average the received data. The underlying objective of coherent integration is for the signal phase to add constructively from pulse to pulse, allowing the signal amplitude to multiply by the number of pulses emitted. It also operates under the assumption that the noise will be uncorrelated from pulse to pulse. In the case that a target is moving and the pulses are out of phase, there are processing techniques that can be performed prior to coherent integration to mitigate this issue. By utilizing coherent integration, we are thus improving the SNR from (1.4) to,

$$SNR_{coh} = \frac{P_t\ G_t^2\ \lambda\ \sigma\ N_p}{(4\pi)^3 R^4 k T_o\ BF}. \tag{1.5}$$

Improving the SNR by a factor of the number of pulses N_p.

Another option is to perform noncoherent integration, which only requires the magnitudes from the measured samples. By discarding the phase information of the individual pulses, processing the pulses from a moving target is easier. On the other hand, the SNR cannot be wrapped up into a nice equation like (1.5), because the signal and noise components are no longer easily separated. Therefore, in order to determine the SNR improvement, knowledge about the probability density functions (PDF) for the noise-only case and the signal-plus-noise-only case is required. In general you can count on the SNR improvement from noncoherent integration to be,

$$\sqrt{N_p}\, SNR_{coh} \leq SNR_{nc} < N_p\, SNR_{coh}. \tag{1.6}$$

While SNR_{nc} is more difficult to determine, noncoherent integration is easier to perform than coherent.

1.4 Pulse Compression

What else can be done to increase the transmit power? Of course there is always the option to use a transmitter that outputs more power, but this change presents several undesirable repercussions. Increasing the bandwidth appears to be a good alternative, but as stated previously because of the inverse relationship with the pulse width T, this would adversely affect ΔR. Thankfully, a technique was developed to decouple T and ΔR known as *pulse compression*. *Pulse compression* uses various types of modulation in the interest of increasing signal bandwidth B, while still transmitting a longer pulse. Then once the echo is received, a *matched filter* is applied to the return to compress the long pulse to approximately $1/B$. Typically the modulation employed is frequency or phase modulation, due to the detrimental effects amplitude modulation has on the transmitter and detection efficiency. By utilizing pulse compression, a radar can have its cakes and eat it too, by still achieving the energy of a longer pulse but retaining ΔR of a short pulse.

One of the most widely known pulse compressed radar waveforms is the linear-frequency modulated (LFM) waveform. The LFM waveform transmits a constant amplitude rectangular pulse of length T. Which is then frequency modulated such that the frequency linearly sweeps the

bandwidth B. Also referred to as a *chirp* waveform, the frequency can linearly increase or decrease, denoted as an *up-chirp* illustrated in Figure 1-4 or *down-chirp*, respectively. The LFM is defined by,

$$s(t) = \begin{cases} \exp\left(j\pi \frac{B}{T} t^2\right), & 0 \le t \le T \\ 0, & otherwise \end{cases}. \tag{1.7}$$

The *matched filter* is exactly as the name implies, it is a filter that is matched to the transmitted signal. Using the transmitted signal, the matched filter becomes the time reversed, complex conjugate, as shown in (1.8). By using the matched filter on the received signal, we are essentially determining the correlation and for this case, it is known as the autocorrelation response.

$$h(t) = a\, s^*(t), \qquad 0 \le t \le T. \tag{1.8}$$

To visualize the improvement pulse compression provides, the autocorrelation and power spectral densities (PSD) of a simple unmodulated pulse is shown in comparison to an LFM waveform in Figure 1-4. Not only is there an improvement in ΔR, but employing the matched filter in (1.8) also maximizes the SNR therefore, also improving detector efficiency.

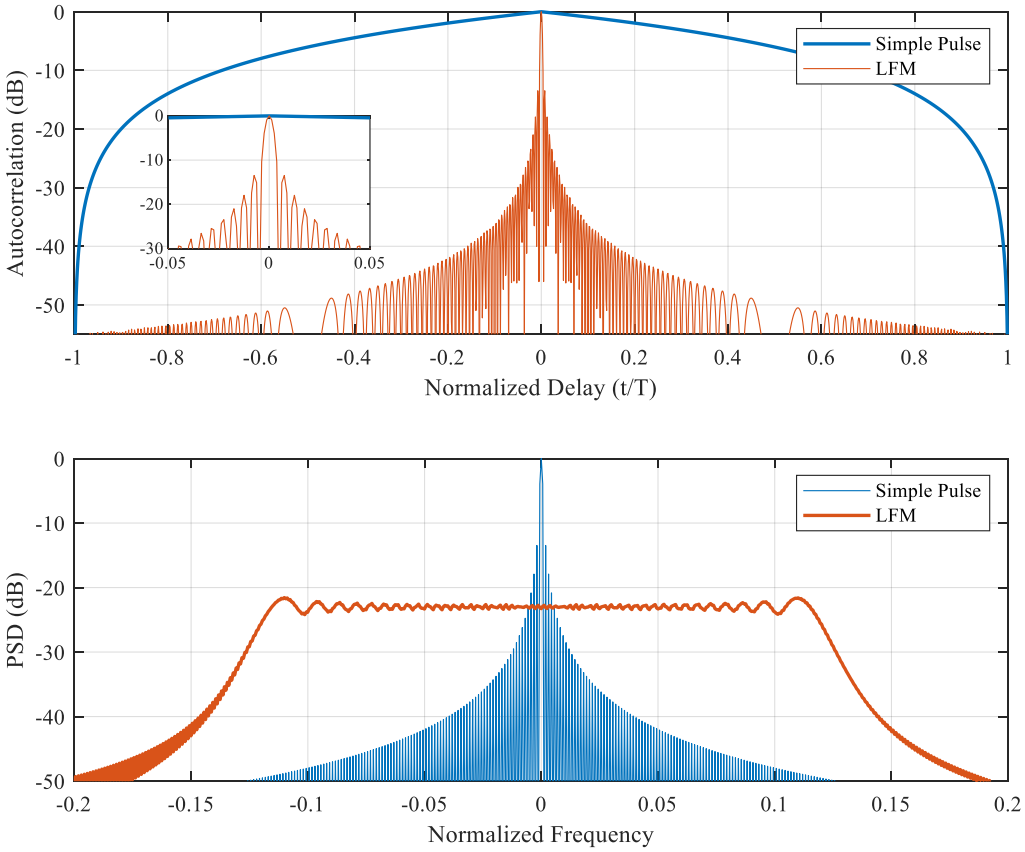

Figure 1-4: Autocorrelation response (top) and power spectral density (PSD) (bottom) of a simple unmodulated pulse and linear FM (LFM) waveform

1.4.1 Autocorrelation Sidelobes

The autocorrelation shown in Figure 1-4 illustrates great ΔR, but ΔR is not the only factor that affects the ability to detect targets. From Figure 1-4, we see that the peak sidelobe level (PSL) for the LFM waveform falls at -13.2 dB and is completely independent of BT. This sidelobe level poses issues when there is more than one target present, especially in the case that one has a much larger return than the other. As demonstrated in Figure 1-5, the return from a large scatterer at a delay of 5 μs nearly mask the return from a smaller scatterer at 5.5 μs.

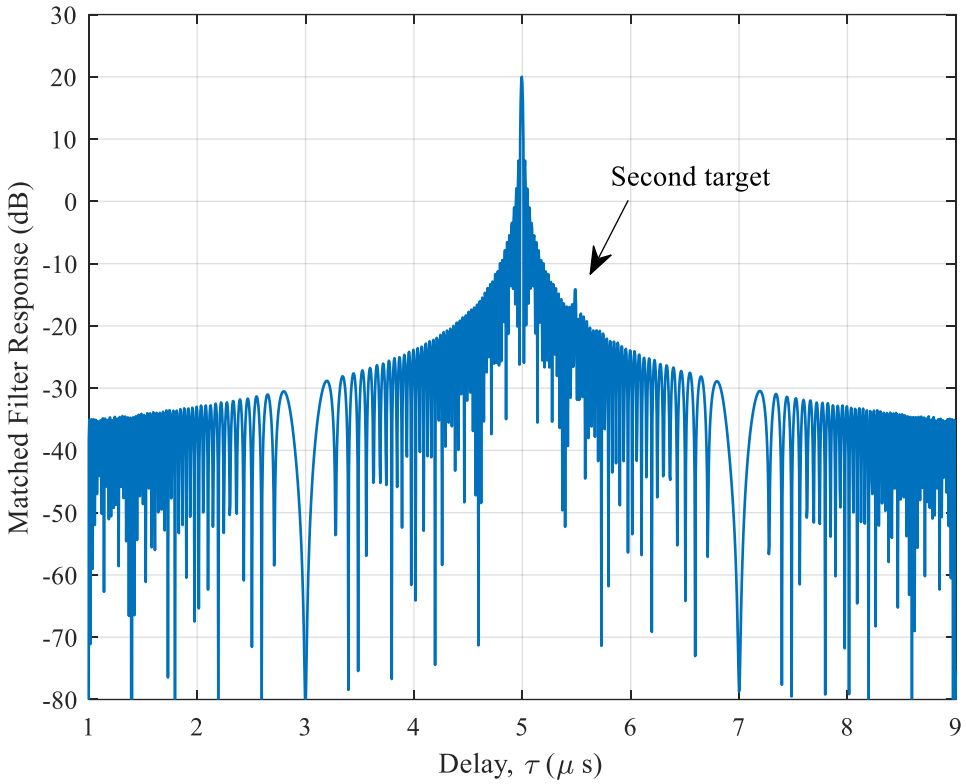

Figure 1-5: Return of LFM waveform when two targets are present with large difference in power returned

Of course, there are options to mitigate this type of issue, but as usual they come at a cost. For example, in the case of LFM waveforms, mismatch filtering can be applied to the received signal but recall that the matched filter is the filter that provides the maximum SNR. Therefore, the cost of using the mismatch filter comes at the price of a degraded SNR with a loss of,

$$SNR_{MMF\ Loss} = -10\log_{10}\left(\frac{\sum_{n=1}^{NK}|w(n)|^2}{NK\ \sum_{n=1}^{NK}w^2(n)}\right), \tag{1.9}$$

where N is equivalent to BT and K is the over-sampling factor relative to the 3 dB bandwidth. Customarily, the mismatch filter is formed from the matched filter where a window function, such as a *Hamming*, *Hanning*, or *Taylor* window, replaces the arbitrary constant amplitude a in (1.8). Or instead, the spectrum of the received data is tapered with a window function prior to filtering. Along with degraded SNR performance, the ΔR will deteriorate as well.

1.4.2 Random Frequency Modulated Waveform (RFM)

Ambiguity of targets, whether that be in range or Doppler are a nuisance for processing. As defined back in (1.3), there is a maximum range that a target can extend to before it is considered ambiguous. There are a few detection techniques that can solve for the targets true location, such as *M of N* detection, but even so there are still range and Doppler values that are ambiguous. A waveform however, that possess random attributes, such as noise radar, is capable of alleviating these ambiguities [5,6]. Random FM (RFM) waveforms not only diminish the number of ambiguities, but they are constant amplitude and continuous in phase, making them amenable to high-power transmitters. The random nature of the RFM waveform implies a non-repeating structure which naturally provides the additional sidelobe suppression! Along with the favorable characteristics of RFM, there are downfalls, such as range sidelobe modulation (RSM). There are various versions of RFM waveforms that have been optimized and experimentally demonstrated in different manners. Such as the spectrally-shaped versions of RFM [10] that exhibited improved spectral containment and achieved lower range sidelobes. A subclass that utilizes a parameterized structure will be the main character in the next few chapters.

Chapter 2 Radar Signals

2.1 Radar Phase Codes

There are different methods to generating a pulse compressed radar waveform and one such method is by utilizing phase codes. For a phase-coded waveform, the pulse to be transmitted is divided into subsections, for example a pulse of width T can be divided into N constant-amplitude subpulses, also called chips. Each subpulse will have a width $T_{\mathrm{p}} = T/N$, and will be modulated by a phase value θ_n, as shown in Figure 2-1. The discretized phase values elicited to modulate each subpulse is based on a phase constellation. The phase constellation may be composed of two states

(symbols) or a continuity of symbols that are limited only by the systems numerical precision, known as biphase codes and polyphase codes, respectively.

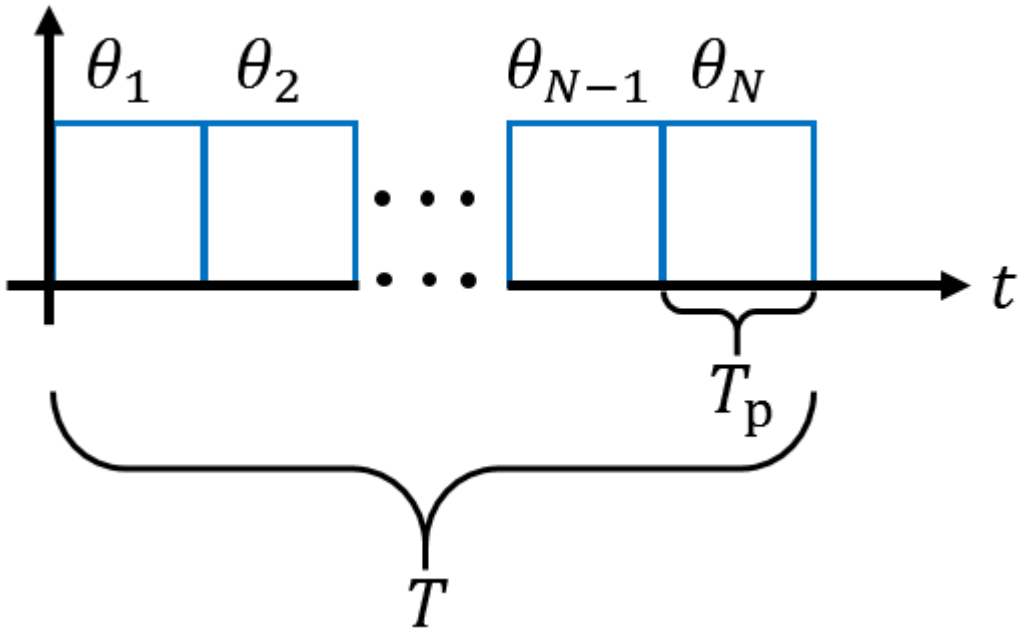

Figure 2-1: Phase-coded waveform structure

Over the years plenty of research has gone into finding optimal phase codes for radar applications. Whether that be biphase or polyphase codes, various families of codes exist that examine sidelobe response, sequence length, and in some cases Doppler tolerance. For example, Barker codes were discovered in 1953 and achieve a peak sidelobe to mainlobe ratio equivalent to the code length [1,2,13]. Granted the maximum code length known at this time for Barker codes is 13.

2.2 Polyphase-Coded Frequency Modulation

With phase codes, the abrupt phase transition between subpulses results in spectral spreading with $\sin(x)/x$ roll-off that diminishes the spectral containment. An offshoot of phase codes is polyphase-coded frequency modulation (PCFM), which utilizes techniques from communications to realize continuous smooth phase transitions, thus improving spectral containment. Nearly identical

to continuous phase modulation (CPM), PCFM follows similar implementation style but disregards aspects that are irrelevant to radar design. Specifically, CPM encodes information for communications between users, while PCFM radar waveforms are concerned with designing signals that optimally glean information from the illuminated environment.

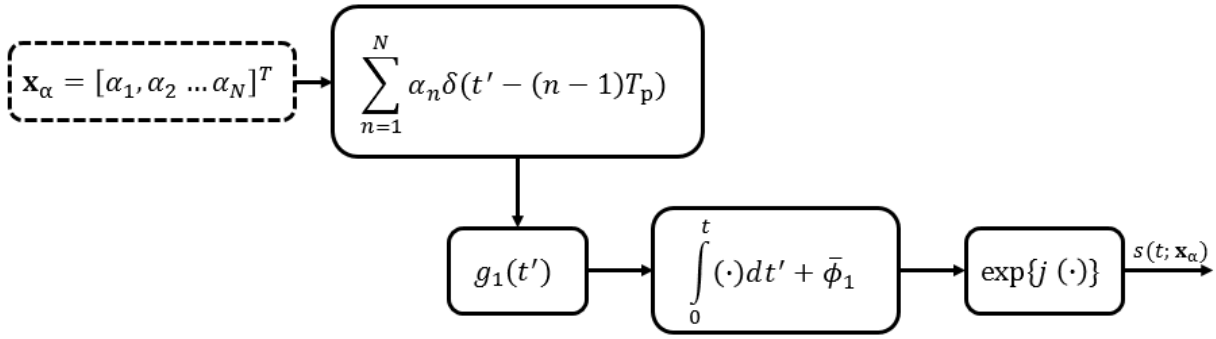

Figure 2-2: PCFM Radar waveform implementation

The PCFM waveform implementation, splits the pulse width T, into N consecutive impulses separated in time by $T_\mathrm{p} = T/N$, to form an impulse train. This impulse train is then weighted by a vector $\mathbf{x}$ containing the time-varying digital frequency, i.e., the n^{th} pulse is weighted by α_n. The weighted impulse train is convolved with a shaping filter $g(t')$, where $g(t')$ integrates to one over the defined interval $[0, T_\mathrm{p}]$. After which, to attain a continuous phase function, an integration stage occurs thus forming the contents of the exponential that establish the PCFM waveform. We can condense this process and express it as,

$$s(t; \mathbf{x}) = \exp\left\{ j \left(\int_0^t g_1(\tau) * \left[\sum_{n=1}^{N} \alpha_n \, \delta\big(\tau - (n-1)T_\mathrm{p}\big) \right] d\tau \right) \right\}, \tag{2.1}$$

where $*$ denotes convolution. While the implementation in Figure 2-2 and (2.1) pertains to first-order PCFM, this is easily extensible to higher-orders, which will be further discussed in later sections.

2.2.1 First-Order PCFM

As discussed previously first-order PCFM follows the implementation show in Figure 2-2, but what makes it specifically first-order? In order to be first-order PCFM the phase needs to be differentiable. In the case a rectangular filter is employed as the shaping filter, the phase trajectories after integration of the first-order PCFM, are simply piecewise linear. Along with the requirement of differentiability, the span of the parameters is also indicative of the PCFM order and in the first-order case, $\alpha_n \in [-\pi, \pi]$. While this requirement can be relaxed to exceed this interval, which is known as *over-phasing*, this expansion is correlated with a spread in the spectrum.

When the phase $\phi(t; \mathbf{x}_\alpha)$ is evaluated, we recognize that the benefit of the PCFM waveform structure extends past the basic desires of a radar waveform, like constant amplitude, continuous phase, and transmitter amenable implementation,

$$\phi_1(t; \mathbf{x}_\alpha) = \sum_{n=1}^{N} \alpha_n \, b_n(t). \tag{2.2}$$

Due to the discrete parameter structure, PCFM also facilitates the optimization of the waveform parameters, which will be explored in Chapter 3. In (2.2), the phase function is composed of both the discretized parameters and the continuous quasi-basis functions. By proper discretization, i.e., through adequate oversampling to ensure sufficient spectral containment, the discretized PCFM model becomes,

$$\mathbf{s} = \exp(j \, \mathbf{B} \, \mathbf{x}_\alpha). \tag{2.3}$$

Where columns of the matrix $\mathbf{B}$, are composed of the quasi-basis functions that are simply delay-shifted versions of the integrated shaping filter and the vector $\mathbf{x}_\alpha$ contain the first-order parameters. Again, in the case that the shaping filter utilized is rectangular, the quasi-basis functions become,

$$b_n(t) = \begin{cases} 0, & 0 \le t < (n-1)T_\mathrm{p} \\ \big(t - (n-1)T_\mathrm{p}\big)/T_\mathrm{p}\,, & (n-1)T_\mathrm{p} \le t < n\,T_\mathrm{p}, \\ 1, & n\,T_\mathrm{p} \le t \le N\,T_\mathrm{p} \end{cases} \tag{2.4}$$

i.e., for first-order PCFM the quasi-basis functions are a linear ramp to a constant, as shown in Figure 2-3.

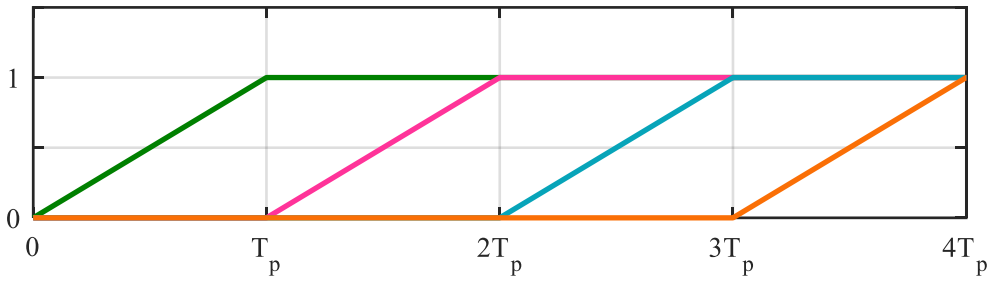

Figure 2-3: First-order PCFM quasi-basis functions

From (2.4), we see that first-order PCFM has piecewise linear phase trajectories, which will play a role in first-order's ability to represent an LFM waveform. For an LFM upchirp, it is known that the frequency linearly sweeps the bandwidth during the pulse width. This arises from the phase of an LFM which is,

$$\phi_{LFM}(t) = \pi \frac{B}{T} t^2. \tag{2.5}$$

Taking the derivative of the phase with respect to time, the instantaneous frequency is found as,

$$f_{LFM}(t) = \frac{1}{2\pi} \frac{d}{dt} \left(\phi(t)\right)$$

$$= \frac{B}{T} t. \tag{2.6}$$

On the other hand, when first-order is used to represent the LFM waveform, the use of the rectangular shaping filter results in a piecewise linear frequency. Therefore, first-order can only approximate an LFM waveform, this behavior is highlighted in Figure 2-4 and Figure 2-5. In these figures, the frequency excursions of the LFM (orange) are smooth and the first-order approximate LFM frequency is observed taking small-steps.

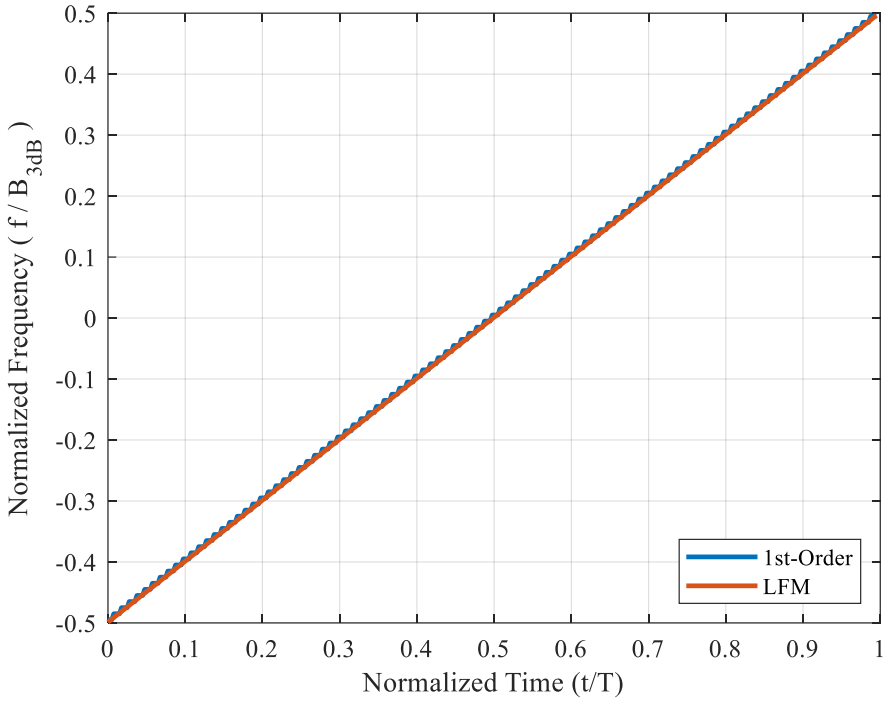

Figure 2-4: Instantaneous frequency of 1st-order approximated LFM and actual LFM

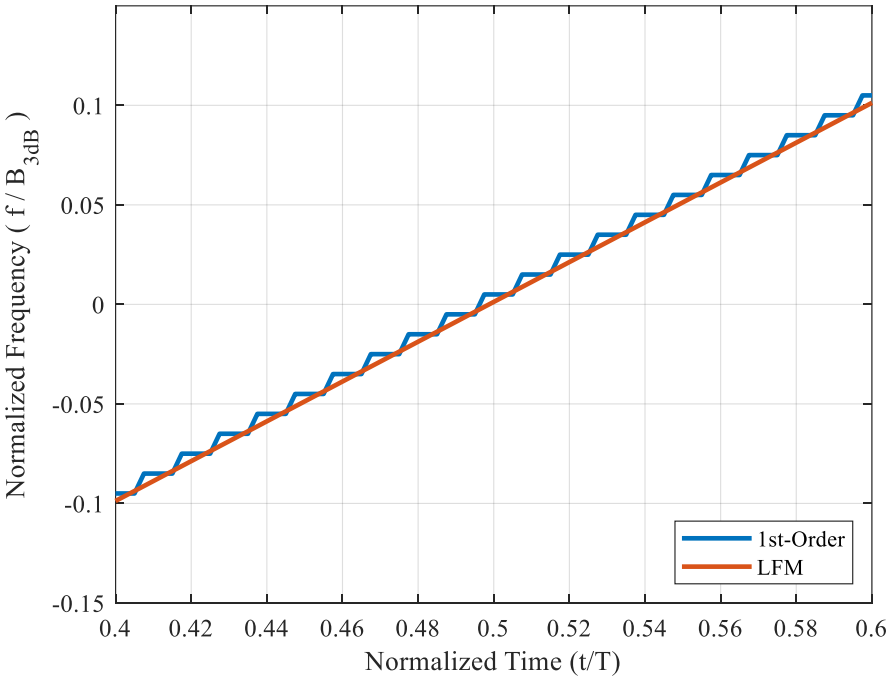

Figure 2-5: Focused instantaneous frequency behavior

The integration in (2.1), produces a continuous phase despite the stair stepping behavior that is shown in Figure 2-4 and Figure 2-5. After all we are dealing with an FM waveform. But the behavior of the instantaneous frequency will be a distinguishing characteristic between the different PCFM orders, along with the instantaneous chirp rate! Where chirp rate is the amount of time or rate that the frequency changes, for example an LFM waveform has a constant chirp rate. The chirp rate is mathematically represented as the derivative of the instantaneous frequency,

$$\psi(t) = \frac{1}{2\pi}\frac{d}{dt}f(t) = \frac{1}{2\pi}\frac{d^2}{dt^2}\phi(t). \tag{2.7}$$

To explore the differences between the different orders of PCFM and Fourier waveform, we can examine the instantaneous phase, frequency, and chirp rate behavior. To ensure a fair comparison between the three quasi-basis types, pseudo-random optimized FM (PRO-FM) waveforms [35] were used to initiate the waveform sets. Followed by a least-squares in phase mapping to produce the appropriate parameters based on the quasi-basis used. Five first-order waveforms were initialized using this method and in Figure 2-6 we have the first-order instantaneous phase, frequency, and chirp rate illustrated. From this we see that just like Figure 2-4 and Figure 2-5, the instantaneous frequency has a step-like behavior, where it is constant and abruptly changes. If we think about how this behavior will influence the derivative, we know that the areas of constant slope will be zero and the abrupt changes will cause discontinuities; which is exactly what we see in the instantaneous chirp rate plot in Figure 2-6.

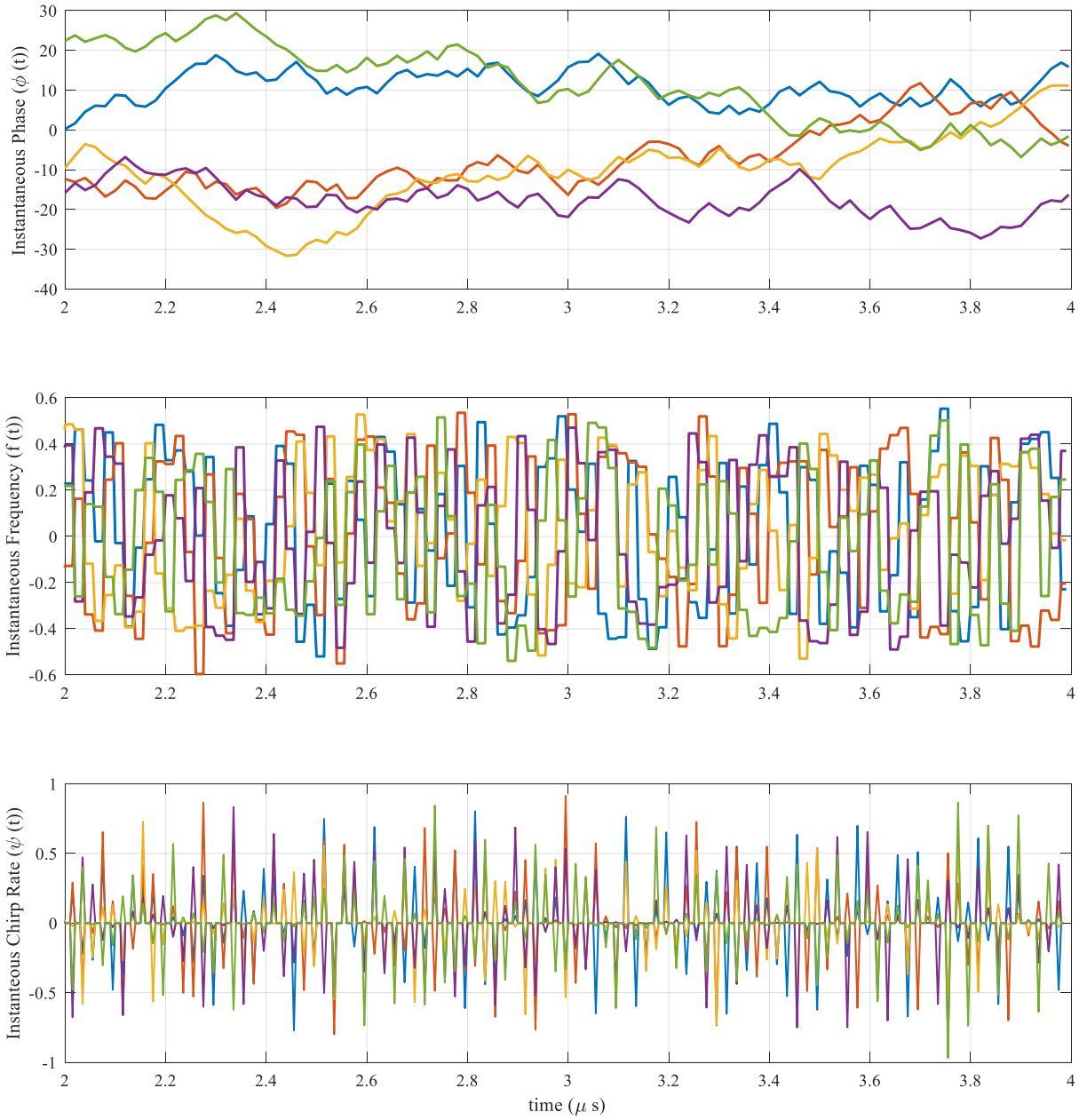

Figure 2-6: Five PRO-FM LS phase mapped initializations of first-order PCFM instantaneous phase (top), instantaneous frequency (middle), and instantaneous chirp rate (bottom)

2.2.2 Second-Order PCFM

Now that 1st-order PCFM has been discussed, higher-order PCFM implementations can be introduced, beginning with second-order PCFM. Higher-order PCFM implementations were first explored in [16], with the notion that the higher-order implementations had the ability to expand the number of physically realizable waveforms. This ability was appealing as it proposed a means to address the growing issue of a congested spectrum because of the increase in design space. But what do these higher-order PCFM implementations look like?

As stated previously, the attributes that discern the PCFM order are the number of integration stages and the span of the parameters, while the latter may be more lax. The implementation is almost identical to first-order, as shown in Figure 2-7. For second-order PCFM the implementation still begins by weighting the impulse train of N pulses, by the second-order parameters contained within the vector $\mathbf{x}_\beta = [\beta_1\ \beta_2 \ldots \beta_N]^T$. Following the convolution of the weighted impulse train with the shaping filter $g(t'')$, there are two integration stages, producing a continuous phase function from the parameters that represent a time-varying chirp rate.

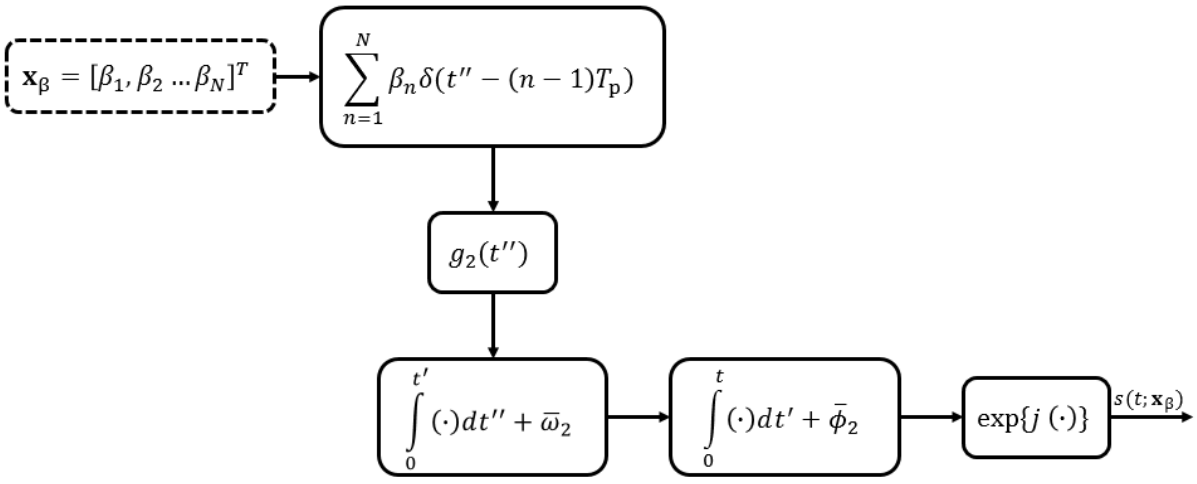

Figure 2-7: Second-order PCFM implementation

The process described in Figure 2-7, can be condensed and summarized into the expression found in (2.8), where $g_2(\tau)$ is the shaping filter, $\bar{\omega}_2$ is the initial frequency, and $\bar{\phi}_2$ is the initial phase.

In [16], the range of permissible second-order parameters is fully derived, finding that $\beta_n \in [-2\pi, +2\pi]$,

$$s_2(t;\mathbf{x}_\beta) = \exp\left\{ j \left(\int_0^t \int_0^{t'} g_2(\tau) * \sum_{n=1}^{N} \beta_n \, \delta\big(\tau - (n-1)T_\mathrm{p}\big) \, d\tau \, dt' + \int_0^t \bar{\omega}_2 \, dt' + \bar{\phi}_2 \right) \right\}. \tag{2.8}$$

Working under the assumption that a rectangular shaping filter is the filter of choice, evaluation of the phase in (2.8) reveals further simplifications can be made similar to those made for the first-order PCFM.

$$\phi_2(t;\mathbf{x}_\beta) = \int_0^t \int_0^{t'} \sum_{n=1}^{N} \beta_n \, g_2\big(\tau - (n-1)T_\mathrm{p}\big) \, d\tau \, dt' + \int_0^t \bar{\omega}_2 \, dt' + \bar{\phi}_2. \tag{2.9}$$

Performing the double integral in (2.9), still assuming a rectangular shaping filter, the second-order PCFM may also be implemented in a discretized form. In previous work such as [12], the first-order PCFM quasi-basis was main focus, in [16] the second-order PCFM implementation was touched on but the quasi-basis was not fully derived. The following shows the development of the second-order quasi-basis used in [17]. To simplify this process, the rectangular shaping filter can be thought of as a piecewise function, i.e.,

$$g_2(\tau) = \begin{cases} 0, & 0 \le \tau < (n-1)T_\mathrm{p} \\ 1/T_\mathrm{p}^2, & (n-1)T_\mathrm{p} \le \tau < n\,T_\mathrm{p} \\ 0, & n\,T_\mathrm{p} \le \tau \le N\,T_\mathrm{p} \end{cases}. \tag{2.10}$$

Therefore, when the double integral is evaluated, we examine each interval individually,

$0 \le \tau < (n-1)T_\mathrm{p}$:	$(n-1)T_\mathrm{p} \le \tau < n\,T_\mathrm{p}$:	$n\,T_\mathrm{p} \le \tau \le N\,T_\mathrm{p}$:
$h_2(t') = \int_0^{t'} 0\,d\tau$	$h_2(t') = \int_{(n-1)T_\mathrm{p}}^{t'} \frac{1}{T_\mathrm{p}^2}\,d\tau$	$h_2(t') = \int_{n\,T_\mathrm{p}}^{t'} 0\,d\tau$
$= 0$	$= \frac{\tau}{T_\mathrm{p}^2}\Big\|_{(n-1)\,T_\mathrm{p}}^{t'}$	$= 0 + C.$
	$= \frac{t'}{T_\mathrm{p}^2} - \frac{n-1}{T_\mathrm{p}} + C$	

(2.11)

Using the constant of integration C we can ensure that at the border of each region the functions are equal, guaranteeing that we have a continuous function, therefore,

$(n-1)\,T_\mathrm{p}$:	$n\,T_\mathrm{p}$:
$0 = \frac{t'}{T_\mathrm{p}^2} - \frac{n-1}{T_\mathrm{p}} + C\Big\|_{t'=(n-1)\,T_\mathrm{p}}$	$\frac{t'}{T_p^2} - \frac{(n-1)}{T_p} = C\Big\|_{t'=n\,T_\mathrm{p}}$
$0 = \frac{(n-1)T_\mathrm{p}}{T_\mathrm{p}^2} - \frac{n-1}{T_\mathrm{p}} + C$	$\frac{nT_\mathrm{p}}{T_\mathrm{p}^2} - \frac{(n-1)}{T_\mathrm{p}} = C$
$0 = C$	$\frac{1}{T_\mathrm{p}} = C.$

(2.12)

This results in the following expression, which will need to be integrated once more,

$$h_2(t') = \begin{cases} 0, & 0 \le t' < (n-1)T_\mathrm{p} \\ t'/T_\mathrm{p}^2 - (n-1)/T_\mathrm{p}\,, & (n-1)T_\mathrm{p} \le t' < n\,T_\mathrm{p}. \\ 1/T_\mathrm{p}, & n\,T_\mathrm{p} \le t' < N\,T_\mathrm{p} \end{cases} \tag{2.13}$$

Performing the same process again and evaluating each region individually, we find the following,

$0 \le t' < (n-1)T_\mathrm{p}$:	$(n-1)T_\mathrm{p} \le t' < n\,T_\mathrm{p}$:	$n\,T_p \le t' \le N\,T_p$:
$h_2(t) = \int_0^t 0\; dt'$	$h_2(t) = \int_{(n-1)\,T_\mathrm{p}}^{t} \frac{t'}{T_\mathrm{p}^2} - \frac{n-1}{T_\mathrm{p}}\; dt'$	$h_2(t) = \int_{n\,T_p}^{t} \frac{1}{T_p} dt'$
$= 0$	$= \frac{t'^2}{2T_\mathrm{p}^2} - \frac{(n-1)t'}{T_\mathrm{p}}\Big\|_{(n-1)\,T_\mathrm{p}}^{t}$	$= \frac{t'}{T_\mathrm{p}}\Big\|_{n\,T_\mathrm{p}}^{t}$
	$= \frac{t^2}{2T_\mathrm{p}^2} - \frac{(n-1)t}{T_\mathrm{p}} + \frac{(n-1)^2}{2}$	$= \frac{t}{T_\mathrm{p}} - n + C.$
	$+ C$	

(2.14)

Determining C to ensure the function is continuous at the boundaries,

$(n-1)T_\mathrm{p}$:	$n\,T_\mathrm{p}$:
$0 = \frac{t^2}{2T_\mathrm{p}^2} - \frac{(n-1)t}{T_\mathrm{p}} + \frac{(n-1)^2}{2}$	$\frac{t^2}{2\,T_\mathrm{p}^2} - \frac{(n-1)\,t}{T_\mathrm{p}} + \frac{(n-1)^2}{2}$
$+ C\Big\|_{t=(n-1)\,T_\mathrm{p}}$	$= \frac{t}{T_\mathrm{p}} - n + C\Big\|_{t=n\,T_\mathrm{p}}$
$0 = \frac{(n-1)^2T_\mathrm{p}^2}{2T_\mathrm{p}^2} - \frac{(n-1)^2T_\mathrm{p}}{T_\mathrm{p}}$	$\frac{n^2\,T_\mathrm{p}^2}{2\,T_\mathrm{p}^2} - \frac{(n-1)\,n\,T_\mathrm{p}}{T_\mathrm{p}} + \frac{(n-1)^2}{2}$
$+ \frac{(n-1)^2}{2} + C$	$= \frac{n\,T_\mathrm{p}}{T_\mathrm{p}} - n + C$
$0 = C$	$\frac{1}{2} = C.$

(2.15)

Finally, this results in the following second-order quasi-basis functions,

$$b_n(t) = \begin{cases} 0, & 0 \le t < (n-1)\,T_\mathrm{p} \\ t^2/2T_\mathrm{p}^2 - (n-1)\,t\,/\,T_\mathrm{p} + (n-1)^2/2\,, & (n-1)\,T_\mathrm{p} \le t < n\,T_\mathrm{p}. \\ t/T_\mathrm{p} + {}^1\!/_2 - n, & n\,T_\mathrm{p} \le t \le N\,T_\mathrm{p} \end{cases} \tag{2.16}$$

Resulting in a piecewise function composed from a quadratic to a linear ramp, as visualized in Figure 2-8,

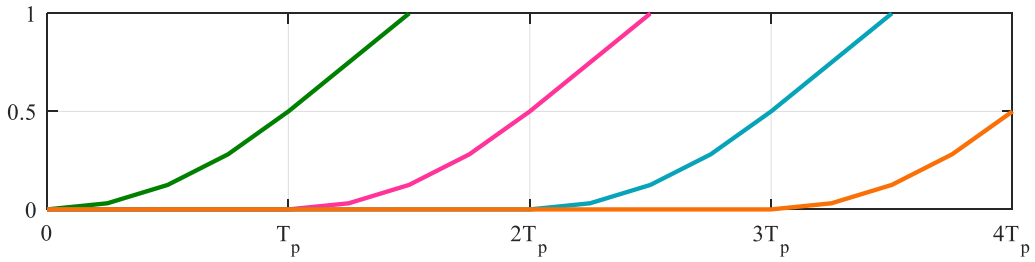

Figure 2-8: Second-order PCFM quasi-basis functions

Figure 2-8 shows that the phase trajectories are quadratic, exactly like the phase of an LFM waveform, which allows second-order to perfectly replicate the well-known Doppler tolerant waveform. An LFM waveform is also known for being spectrally contained, since first-order can only approximate an LFM, the presumption is second-order is better suited for generating spectrally contained waveforms. From the quadratic phase function, we can determine the frequency using a variation of (2.6), which leads to the piecewise linear instantaneous frequency function,

$$\begin{aligned}\omega_2(t) &= \frac{d}{dt}\phi_2(t) \\ &= \int_0^t \left[\sum_{n=1}^{N} \beta_n \, g_2\big(\tau-(n-1)T_{\mathrm{p}}\big)\right] d\tau + \bar{\omega}_2 \\ &= \sum_{n=1}^{N} \beta_n \frac{d}{dt} b_n(t) + \bar{\omega}_2.\end{aligned} \tag{2.17}$$

To determine the instantaneous frequency function exactly, we can substitute in (2.13) to (2.17).

Along with adequate oversampling of the quasi-basis functions in (2.16), recall back in (2.8), there is also an initial frequency $\bar{\omega}_2$ term that must be included in the discretization. A straightforward and simple approach to include this, is by appending it to the quasi-basis matrix and the time-varying chirp rate parameters, i.e., $\mathbf{B} = [\mathbf{b}_1\ \mathbf{b}_2 \ldots \mathbf{b}_N\ \mathbf{t}]$ and $\mathbf{x}_\beta = [\beta_1\ \beta_2 \ldots \beta_N\ \bar{\omega}_2]^T$, where the vector $\mathbf{t}$, is the discretization of continuous time over the pulse duration T and $\bar{\omega}_2$ is the initial frequency. Recall, the time vector is included to account for the integration of the initial frequency

term. Including this initial frequency term will offset the aggregate spectrum to maintain it at zero (at baseband). This produces the second-order PCFM waveform

$$\mathbf{s} = \exp\left(j\,\mathbf{B}\,\mathbf{x}_{\beta}\right), \tag{2.18}$$

Previously, we evaluated the first-order instantaneous phase, frequency, and chirp rate. We saw that the instantaneous frequency had discontinuities and the instantaneous chirp rate was essentially random impulses. How does second-order PCFM compare to first-order? From (2.17), we know that the instantaneous frequency of second-order is piecewise linear, meaning that the behavior results in a continuous frequency function. The behavior of the second-order instantaneous phase, frequency, and chirp rate is displayed in Figure 2-9. Again, PRO-FM was used to initialize a set of five spectrally contained waveform, where least-squares is employed to phase map the second-order approximation. As we see in Figure 2-9, second-order produces a smooth instantaneous frequency function, demonstrating its ability to replicate an LFM waveform. The instantaneous chirp rate on the other hand is analogous to the behavior we examined from first-order's instantaneous frequency.

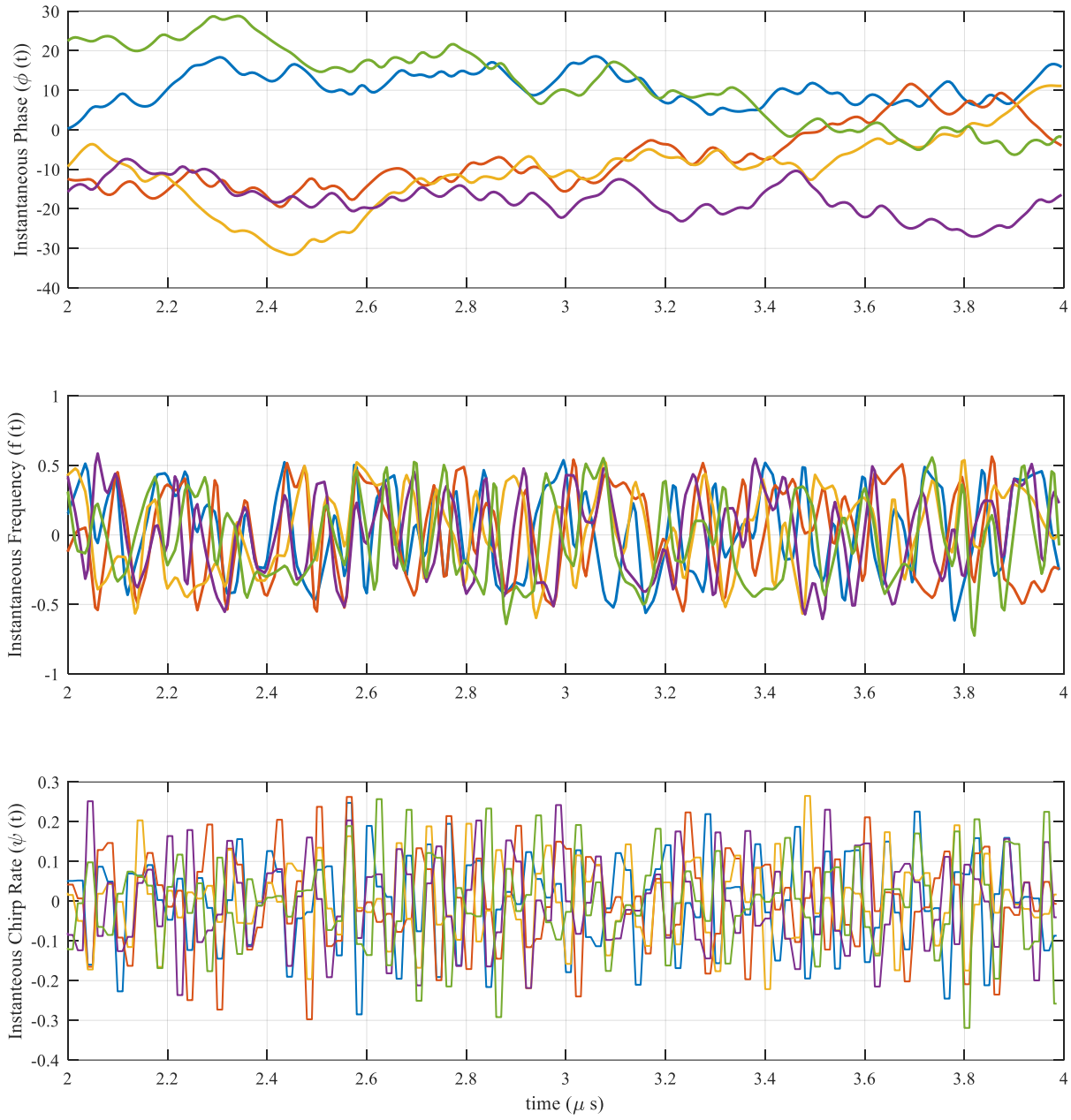

Figure 2-9: Five PRO-FM LS phase mapped initializations of second-order PCFM instantaneous phase (top), instantaneous frequency (middle), and instantaneous chirp rate (bottom)

2.2.3 Over-Coded PCFM

Degrees-of-freedom, when it comes to waveform design, are like nuggets of gold and the perception of extra design freedom is what led to the notion of "over-coded" PCFM. Previously, for first- and second-order PCFM, the pulse width T, contained an impulse train of N consecutive impulses, separated by $T_\mathrm{p} = T/N$. These N subpulses are then weighted by the parameters contained within the vector $\mathbf{x}_\alpha = [\alpha_1\ \alpha_2\ \ldots\ \alpha_N]^T$ and sampled K times.

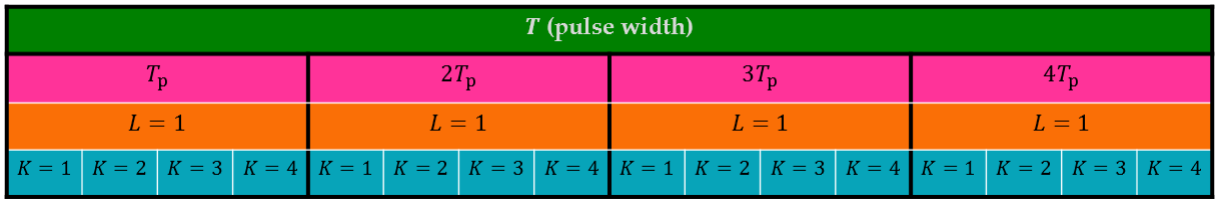

Figure 2-10: Visualization of parameterized sampling structure for $L = 1$

Over-coded further divides T_p by the over-coding factor L, thus increasing the degrees-of-freedom by increasing the number of parameters from $N = BT \rightarrow N = L(BT)$. This division of the time-support T_p signifies that the each impulse in the impulse train will now be separated in time by T_s, where the total pulse width is composed of $T = NT_\mathrm{p} = NLT_\mathrm{s}$. But despite the number of PCFM parameters increasing, the oversampling rate K, stays the same therefore, every T_p interval is still oversampled by K, as shown in Figure 2-11.

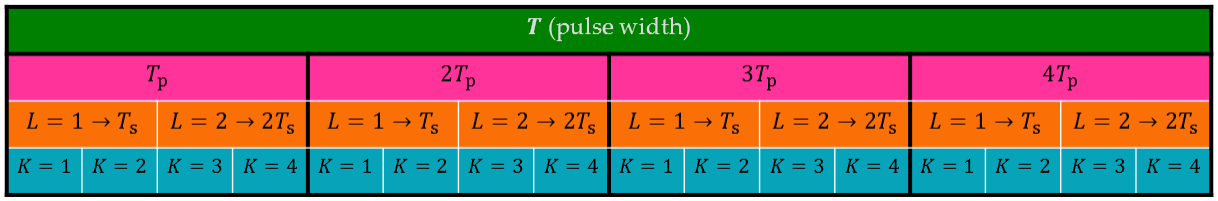

Figure 2-11: Visualization of parameterized sampling structure with an over-coding factor

The degrees-of-freedom have increased by utilizing over-coding and this is due to the partial decoupling of the number of PCFM parameters N, from the time-bandwidth product. Of course, as there are trade-offs for most relationships in radar such as resolution and spectral containment,

there is also a consequence for the decoupling. To maintain the spectral footprint, the relationship of $M = K(BT)$, where M is the number of waveform samples and K is the oversampling factor, must be preserved. Preserving this relationship is addressed by limiting the span of the PCFM parameters, i.e., for first-order PCFM α_n is limited to $[-\pi/L\,, +\pi/L]$. To preserve this relationship, an explicit constraint can be placed on the parameter span during the optimization or as done in [37-38,40], matching the waveform to a spectral template can implicitly constrain the parameters.

The consequences of not limiting the parameter span to $[-\pi/L\,, +\pi/L]$ is displayed in Figure 2-12 and Figure 2-13. In the first figure, we have the autocorrelation and power spectral densities illustrated, where it is clear that the over-coded instantiation lacking the factor of $1/L$ is clearly spread in spectrum, while of course the autocorrelation is thriving. Evaluation of the in-phase and quadrature components is shown in Figure 2-13. From this it is obvious that the phase transitions maintain closer proximity to the edge of the phase circle, when those parameters are limited. Without the factor of $1/L$, those phase transitions begin to cut through the unit circle more and more.

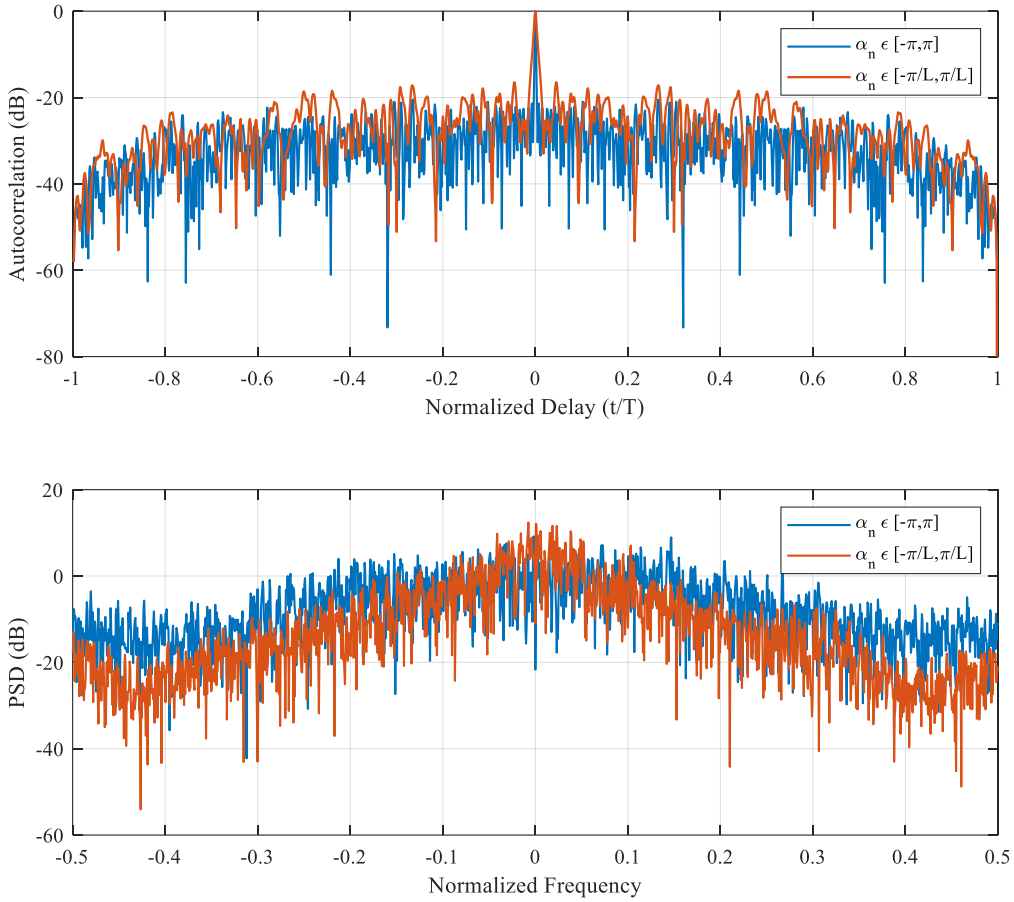

Figure 2-12: Autocorrelation and PSD of over-coded PCFM with and without a limit on parameter span

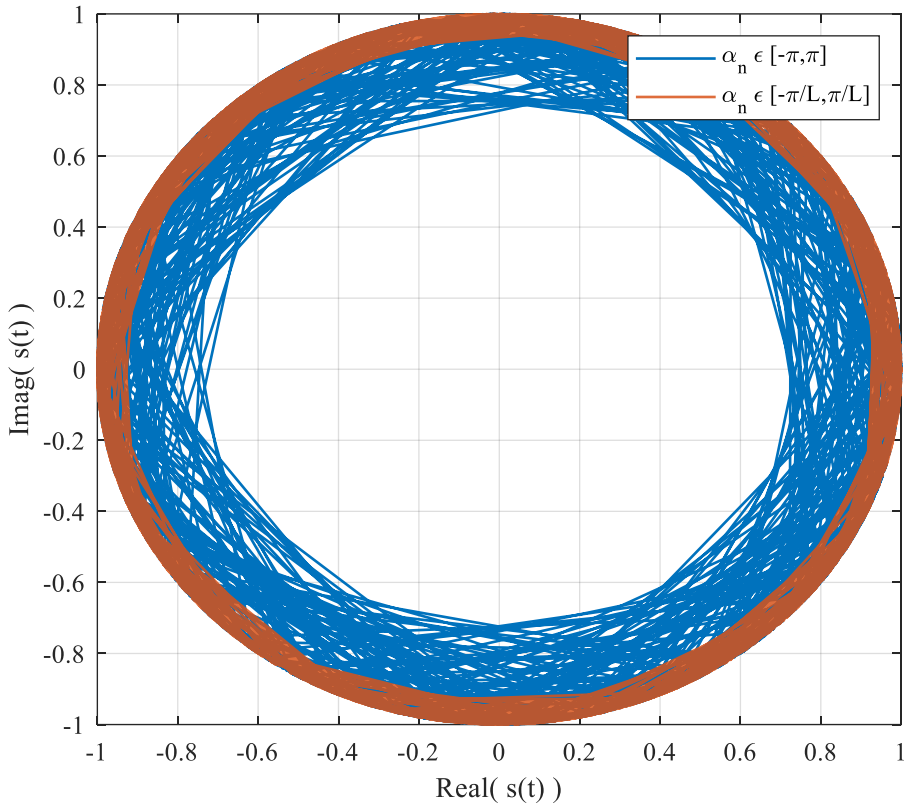

Figure 2-13: In-Phase and quadrature components of over-coded PCFM with and without limit on parameter span

2.3 Fourier

With any order, first, second, or higher-order PCFM the basis-like matrix, **B**, is a quasi-basis structure, which is due to the need to oversample, creating an $M \times N$ non-square matrix. Therefore, these waveforms cannot realize all possible FM structures. While over-coded PCFM poses the possibility of achieving a true basis function, in the case that $K = L$, a constraint either implicit or explicit is necessary to capture sufficient spectral roll-off. Since these are quasi-basis structures that means there are other quasi-bases that could realize other RFM waveform structures possessing different characteristics. Which is what led to the examination of the Fourier-based representation that stems from the constant-envelope OFDM (CE-OFDM) signal model from communications [19,22,25].

The desire here, is to get the Fourier model into the $\exp(j\mathbf{Bx})$ form like the PCFM implementations. Using Euler's formula, the Fourier model may be expressed in terms of sines and cosines. Which then allows for the decomposition of the phase into in-phase/quadrature components,

$$\begin{aligned}\phi_F(t;\,\mathbf{x}) &= \Re\left\{\sum_{n=1}^{N}\gamma_n\exp(j\omega_n t)\right\}\\ &= \sum_{n=1}^{N}\Re\{\,\gamma_n\,\}\cos(\omega_n t) + \Im\{\,\gamma_n\,\}\sin(\omega_n t)\\ &= \sum_{n=1}^{N}\gamma_n^{\Re}\cos(\omega_n t) + \gamma_n^{\Im}\sin(\omega_n t),\end{aligned} \tag{2.19}$$

where $\Re\{\cdot\}$ and $\Im\{\cdot\}$ extract the real and imaginary part of the argument, respectively. Due to this decomposition into sines and cosines, when we form the parameter vector $\mathbf{x}_\gamma$ it is composed of double the number of elements, i.e., $\mathbf{x}_\gamma = \left[\,\mathbf{x}_{\gamma\mathrm{r}}^T\;\mathbf{x}_{\gamma\mathrm{i}}^T\,\right]^T$. Where $\mathbf{x}_{\gamma\mathrm{r}} = \left[\,\gamma_{\mathrm{r},1}\;\gamma_{\mathrm{r},2}\;\ldots\;\gamma_{\mathrm{r},N}\,\right]^T$ and $\mathbf{x}_{\gamma\mathrm{i}} = \left[\,\gamma_{\mathrm{i},1}\;\gamma_{\mathrm{i},2}\;\ldots\;\gamma_{\mathrm{i},N}\,\right]^T$ will now scale $2N$ quasi-basis functions. The quasi-basis functions can easily be discretized by sufficiently sampling the sine and cosine terms and concatenating the resulting two matrices together,

$$\mathbf{B} = [\,\mathbf{B}_\mathrm{C}\;\mathbf{B}_\mathrm{S}\,]. \tag{2.20}$$

Allowing us to form the discretized waveform representation similar to (2.3) and (2.18).

The Jacobi-Anger expansion was previously examined in regards to the CE-OFDM signal in [22,31], it was presented that it could be utilized to determine the spectral properties for a random symbol constellation. To apply this same sentiment to the Fourier-based representation, we need to first evaluate the signal model,

$$s(t) = \exp\left(j\left\{\sum_{n=1}^{N} \gamma_n^{\Re}\ cos(\omega_n t) + \gamma_n^{\Im}\ sin(\omega_n t)\right\}\right)$$

$$= \exp\left(j \sum_{n=1}^{N} \gamma_{\mathrm{r},n}\, cos(\omega_n t)\right) \exp\left(j \sum_{n=1}^{N} \gamma_{\mathrm{i},n}\, sin(\omega_n t)\right). \tag{2.21}$$

If we express the terms as,

$$z_{\mathrm{r},n} = \gamma_{\mathrm{r},n},$$

$$z_{\mathrm{i},n} = \gamma_{\mathrm{i},n}, \tag{2.22}$$

and

$$\theta_n(t) = \omega_n t, \tag{2.23}$$

we can then rewrite (2.21) as,

$$s(t) = \exp\left(j \sum_{n=1}^{N} z_{\mathrm{r},n}\, cos\big(\theta_n(t)\big)\right) \exp\left(j \sum_{n=1}^{N} z_{\mathrm{i},n}\, sin\big(\theta_n(t)\big)\right), \tag{2.24}$$

which is equivalent to,

$$s(t) = \prod_{n=1}^{N} \exp\big(j\ z_{\mathrm{r},n}\ cos\big(\theta_n(t)\big)\big) \exp\big(j\ z_{\mathrm{i},n}\ sin\big(\theta_n(t)\big)\big). \tag{2.25}$$

Thus, leading to the Jacobi-Anger expansion producing,

$$s(t) = \prod_{n=1}^{N} \left\{\left[\sum_{m=-\infty}^{\infty} j^m\, J_m\big(z_{\mathrm{r},n}\big) \exp\big(\, jm\ \theta_n(t)\big)\right]\left[\sum_{m=-\infty}^{\infty} J_m\big(z_{\mathrm{i},n}\big) \exp\big(jm\ \theta_n(t)\big)\right]\right\}, \tag{2.26}$$

where $J_m(\,\cdot\,)$ is the m-th Bessel function of the first-kind. Once we gather the constant terms together, such that $d_{n,m}^{\Re} = j^m\, J_m\big(z_{\mathrm{r},n}\big)$ and $d_{n,m}^{\Im} = J_m(z_{\mathrm{i},m})$, provides us with,

$$s(t) = \prod_{n=1}^{N} \sum_{m=-\infty}^{\infty} d_{n,m}^{\Re}\ \exp(jm\ \omega_n t)\ d_{n,m}^{\Im}\ \exp(jm\ \omega_n t). \tag{2.27}$$

Which can be rewritten as,

$$s(t) = \prod_{n=1}^{N} \sum_{m=-\infty}^{\infty} d_{n,m}^{\Re}\, d_{n,m}^{\Im}\ \exp(j\ 2m\ \omega_n t)\,. \tag{2.28}$$

From (2.28), we are multiplying an infinite sum of complex sinusoids by the Bessel function, the Fourier relationship of which means this product becomes a convolution in the frequency domain. Let's consider the *central limit theorem* (CLT) briefly, where the sum of an infinite sequence of independent random variables has a normal Gaussian distribution [30]. From the CLT, we also know that the probability density of this summation is the convolution of their densities. Thus, drawing a parallel between the CLT and (2.28), we can deduce that the Fourier quasi-basis produces a Gaussian spectral density in the expectation, over a random symbol initialization as the number of parameters N increases.

The Fourier quasi-basis, as discussed is composed of sines and cosines and we know that sine and cosine are infinitely differentiable. Therefore, when we examine the instantaneous phase, frequency, and chirp rate, all three functions will be continuous and smooth. Once again using PRO-FM to generate a random initialization and least-squares to map to the Fourier-representation, the instantaneous phase, frequency, and chirp rate behavior can be observed in Figure 2-14 of a set of five waveforms. In the instantaneous frequency plot, the frequency excursions extend past the 3-dB bandwidth at the end of the pulse width T and similar behavior occurs with the instantaneous chirp rate plot. The least-squares mapping approximates the phase of the Fourier representation with a minimal amount of error, therefore, there is some degradation that is introduced.

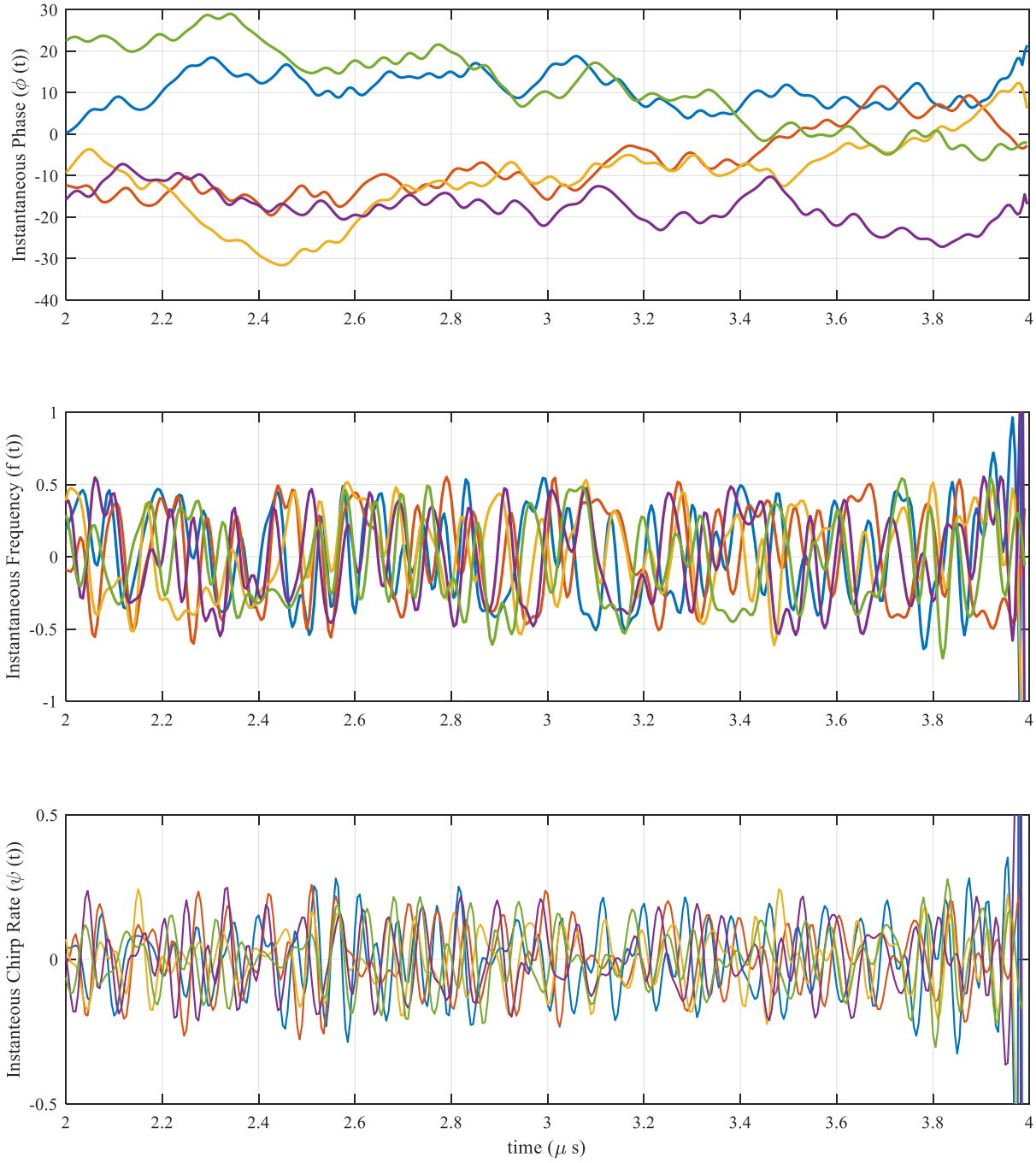

Figure 2-14: Five PRO-FM LS phase mapped initializations of Fourier-based instantaneous phase (top), instantaneous frequency (middle), and instantaneous chirp rate (bottom)

Chapter 3 Optimization

3.1 Purpose and Background

Optimization is used in a wide variety of fields, such as engineering, business, education, science, and even politics. The purpose of optimization is to determine the solution that best fits the given problem through minimizing or maximizing the chosen metric. Whether that be scheduling flight crews for an airline, determining what stocks to buy or sell, or finding parameters that minimize autocorrelation sidelobes. The latter being the goal of the optimization discussed in this chapter. Our goal is to take the waveforms discussed in previous sections and take advantage of their parameterized structure, to generate waveforms with desirable autocorrelation features that have little deviation from the originating 3-dB bandwidth.

In general, an optimization problem will take on the following form,

$$\begin{aligned} &\min f(\mathbf{x}) \\ &\text{subject to } c_i(\mathbf{x}) \geq 0, \qquad i = 1, \dots, m, \end{aligned} \tag{3.1}$$

where the vector $\mathbf{x} = [x_1\ x_2 \dots x_N]$, contains N parameters to be optimized, such that the function $f(\mathbf{x})$ is minimized while satisfying the m constraints, $c_i(\mathbf{x})$. In (3.1), we are considering a minimization problem, but it is important to remember that an optimization problem can either minimize or maximize the desired function. Also, while there are constraints present in (3.1) an optimization problem does not have to have constraints, which is referred to as unconstrained optimization. Now along with constrained and unconstrained optimization problems, there are even more classifiers to describe the type of optimization problem. If the optimization results in a solution such that, $f(\mathbf{x}^*) \leq f(\mathbf{x})\ for\ all\ \mathbf{x} \in \Re^N$ then we have reached a *global* solution, if this is not the case, we have reached a local solution. If a problem has a *global* solution, it is known as a convex problem. There are many more descriptors of optimization problems, but what is important to know here, is that we are dealing with an highly non-convex cost function with no constraints.

3.2 Cost Function

A highly non-convex cost function means that the solution that we obtain is going to be a *local* minimum. In other words, the solution $\mathbf{x}^*$obtained will be a minimum relative to the region $\mathcal{N}$ that it lies within.

$$f(\mathbf{x}^*) \leq f(\mathbf{x}) \; for \; all \; \mathbf{x} \in \mathcal{N}. \tag{3.2}$$

An example of both a *global* and a *local* minimum are shown in Figure 3-1. A global solution implies that the optimal solution that provides the best results is achieved. Therefore, it is gratifying to reach a global solution, but in many cases especially when dealing with highly non-convex cost functions, it cannot be known if the solution obtained is a global solution.

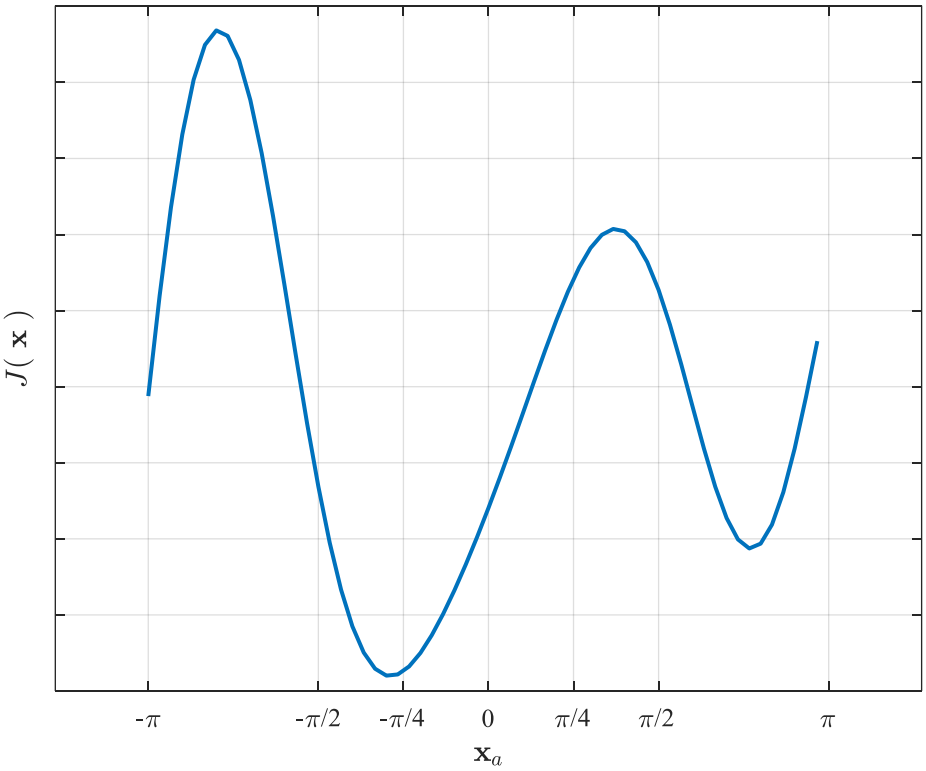

Figure 3-1: *Local* and *global* minimum

The goal of our optimization is to minimize sidelobe levels, while ensuring spectral containment. There are a few metrics that are popular to analyze the sidelobe level of a waveform's autocorrelation, these are the integrated sidelobe level (ISL) and peak sidelobe level (PSL). ISL

evaluates the ratio of the total energy in the autocorrelation sidelobes to the energy in the mainlobe region. While PSL gauges the energy in the largest autocorrelation sidelobe compared to the energy of the mainlobe. These metrics can be written as,

$$\text{ISL} = \frac{\int_{\Delta t}^{T} |\, r(\tau)\,|^2 \, d\tau}{\int_{0}^{\Delta t} |\, r(\tau)\,|^2 \, d\tau}, \tag{3.3}$$

and

$$\text{PSL} = \frac{\max\, \{\, |\, r(\tau)\,|^2 \,\}_{\Delta t}^{T}}{\max\, \{\, |\, r(\tau)\,|^2 \,\}_{0}^{\Delta t}} = \frac{\max\{\, |\, r(\tau)\,|^2\}_{\Delta t}^{T}}{|\, r(0)\,|^2}. \tag{3.4}$$

Both of these equations in (3.3) and (3.4) are highly non-convex and not very well-behaved. To ease the optimization, both (3.3) and (3.4) can be subsumed into [27],

$$\text{GISL} = \left(\frac{\int_{\Delta t}^{T} |r(\tau)|^p \, d\tau}{\int_{0}^{\Delta t} |r(\tau)|^p \, d\tau} \right)^{2/p}, \tag{3.5}$$

where Δt is the peak-to-null width of the autocorrelation mainlobe for $2 \leq p < \infty$. Where when $p = 2$, the GISL metric becomes the ISL and as $p \to \infty$, it becomes the PSL. While we cannot evaluate a value of $p = \infty$, sufficiently large values of p can approximate the PSL metric, in fact a value of $p = 8$, seems to be sufficient.

Recall, that a convex problem is the ideal optimization problem, because it results in a *global* solution. The cost function is evaluating the autocorrelation $r(\tau)$, which is a second-order function of the waveform $s(t)$, therefore when we evaluate the ISL metric, we are evaluating a fourth-order function of the waveform. This results in a highly non-convex cost function, where the solution achieved will be highly dependent on the initialization. There are a few ways to address the initialization, which in this thesis is done by initializing with a waveform that is known to possess "good" waveform characteristics, i.e., the spectrally contained pseudo-random optimized FM (PRO-FM) waveform [35]. PRO-FM is an iterative process that uses alternating time-frequency projections to spectrally match to a Gaussian template. This Gaussian template is defined by a shaping parameter,

for example a shaping parameter value of 2 yields a regular Gaussian but as the shaping parameter approaches ∞, the spectral density becomes rectangular.

3.2.1 GISL Cost Function

The discretized nature of the PCFM parameters still generates a continuous PCFM waveform. The GISL cost function examines the autocorrelation, which examines the waveform, that is formed from the discretized parameters. Therefore, it too is a continuous function, making it a viable candidate to utilize gradient based optimization with respect to the parameters contained in $\mathbf{x}$. This discretization process is discussed in [12], but a short synopsis of the process will be provided here. To optimize, we need to discretize the GISL cost function and that is done by discretizing the autocorrelation first,

$$r[\ell] = \sum_{m=1}^{M} s[m]\, s^*[m+\ell], \tag{3.6}$$

where ℓ is the delay index and $s[m] = 0$ for $m \leq 0$ and $m \geq M$. The conjugate symmetric relationship of $r[-\ell] = r^*[\ell]$ is also maintained. By utilizing the discrete Fourier transform (DFT) and inverse DFT matrices to represent the Fourier transform, the autocorrelation can be expressed in terms of matrix multiplication,

$$\mathbf{r} = \mathbf{A}^H \left[(\mathbf{A}\bar{\mathbf{s}}) \odot (\mathbf{A}\bar{\mathbf{s}})^* \right], \tag{3.7}$$

where $\odot$, $(\cdot)^*$, and $(\cdot)^H$ denote the Hadamard product, complex-conjugate, and Hermitian operations, respectively. To account for circular convolution, $\bar{\mathbf{s}}$ is the zero-padded waveform vector, i.e., $\bar{\mathbf{s}} = \left[\mathbf{s}^T\ \mathbf{0}_{1\times(\mathrm{M}-1)}\right]^T$ and $\mathbf{A}$ and $\mathbf{A}^H$ are the DFT and IDFT matrices, respectively. By writing the autocorrelation is this discretized manner, the GISL cost function becomes,

$$J_p = \frac{\|\mathbf{w}_{\mathrm{SL}} \odot \mathbf{r}\|_p^2}{\|\mathbf{w}_{\mathrm{ML}} \odot \mathbf{r}\|_p^2}, \tag{3.8}$$

where $\mathbf{w}_{\mathrm{SL}}$ and $\mathbf{w}_{\mathrm{ML}}$ are length $(2M-1)$ vectors, composed of zeros and ones responsible for selecting the sidelobe and mainlobe regions of $\mathbf{r}$, respectively.

3.3 Gradient Descent

Optimization is an iterative process and it begins with the initialization, $\mathbf{x}_0$. For a descent optimization, an update needs to be made to the parameters within the vector $\mathbf{x}_i$, which is done via,

$$\mathbf{x}_i = \mathbf{x}_{i-1} + \mu_i \, \mathbf{q}_i, \tag{3.9}$$

where μ_i is a scalar that dictates the current step-size, $\mathbf{q}_i$ is the current search direction, and $\mathbf{x}_{i-1}$ is the vector of the parameters at the $i-1$ iteration. The difference between the types of descent optimization is the method in which the search direction $\mathbf{q}_i$ is selected. Each method will use information about the cost function at the previous iteration to determine how to move for the current iteration, but how this information is used is what differentiates the different optimization styles. For example, some methods may use not only the information from the previous iteration, but also information from iterations past, i.e., $\mathbf{x}_{i-2}, \mathbf{x}_{i-3}, \dots, \mathbf{x}_0$ or they may simply set the search direction to the negative of the gradient, $\mathbf{q}_i = -\nabla_{\mathbf{x}} J$. Recall that the gradient is a direction of ascent, therefore, to achieve a decrease the negative of the gradient is necessary. There are also algorithms that do not require the current iteration to realize an immediate decrease in the cost function, therefore there may be some iterations that an increase occurs, but after a set amount of iterations a decrease will be required.

For a simple explanation, the gradient of the cost function is simply evaluating the partial derivative of the cost function with respect to each parameter, in mathematical notation this is,

$$\nabla_{\mathbf{x}} J = \left[\frac{\partial J}{\partial x_1} \quad \frac{\partial J}{\partial x_2} \quad \cdots \quad \frac{\partial J}{\partial x_N}\right]^T. \tag{3.10}$$

Therefore, $\nabla_{\mathbf{x}} J$ is able to determine the direction to traverse for each parameter in order to obtain a decrease in the cost function. As stated previously, the cost function being evaluated in this thesis is highly non-convex, meaning that there are multiple solutions to the problem. To emphasize this a surface plot is displayed in Figure 3-2; where the cost function was evaluated when two values within the parameter vector were selected at random and varied over the range of permissible values. From

this variation in just two parameters, the cost function surface illustrates several saddle points, substantiating the claim of a highly non-convex cost function and the importance of initialization! This leads to another caveat; how do we know that a decrease in the cost function is happening at each iteration? Which brings us to the *line search*.

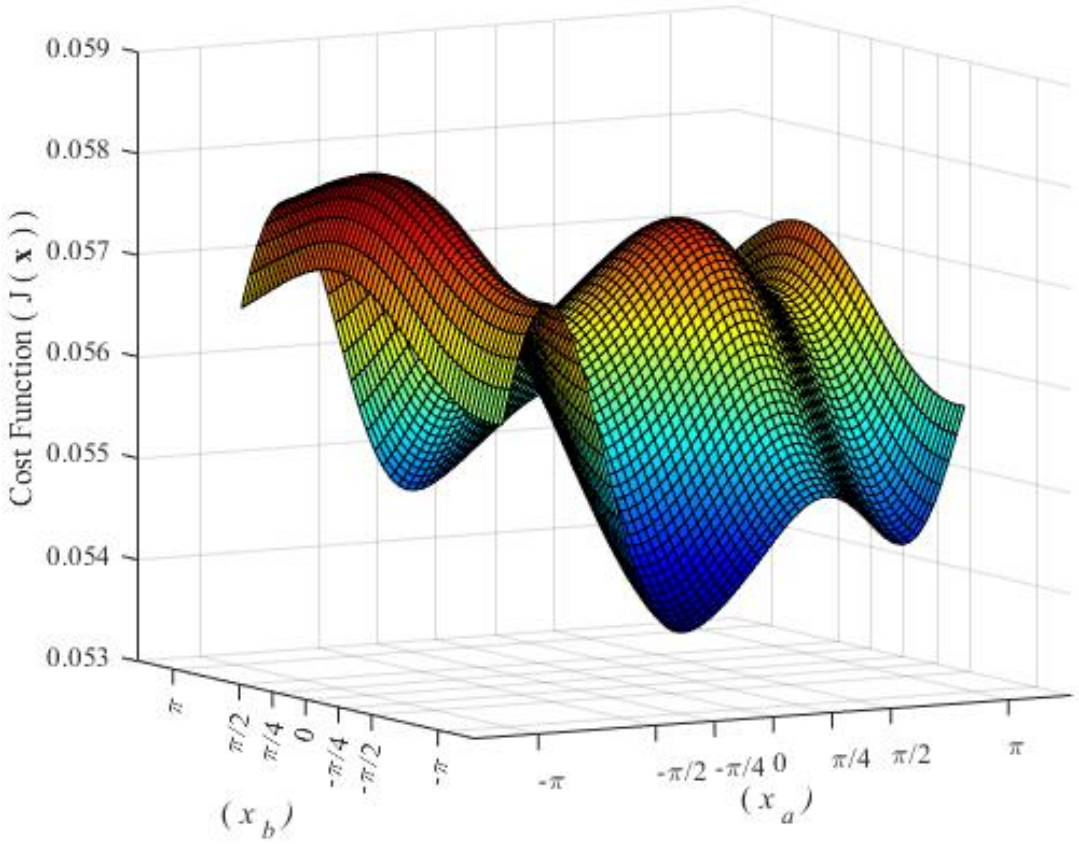

Figure 3-2: Cost function surface plot

3.3.1 Line Search

There are various methods that can be used to determine the search direction for the line search strategy, such as Newton's method. For Newton's method, we utilize curve fitting to determine the Newton Direction, this is done by using the second-order Taylor series approximation to $f(\mathbf{x}_i + \mathbf{q}_i)$, which gives us the following approximation,

$$f(\mathbf{x}_i + \mathbf{q}_i) \approx f_i + \mathbf{q}_i^T \nabla f_i + \frac{1}{2}\, \mathbf{q}_i^T \nabla^2 f_i\, \mathbf{q}_i \stackrel{\text{def}}{=} m_i(\mathbf{q}_i). \tag{3.11}$$

Which when we make a few assumptions, like $\nabla^2 f_i$ being positive definite and taking the derivative with respect to $\mathbf{q}_i$, we find the Newton Direction to be,

$$\mathbf{q}_i = -(\nabla^2 f_i)^{-1} \nabla f_i. \tag{3.12}$$

When $\nabla^2 f_k$ is positive definite, Newton's method converges quickly but if it is not positive definite the resulting search direction may not be a descent direction. Also, if the difference between the true function and the model is too large, the Newton direction is not the most reliable.

Here the search direction will follow steepest-descent, while also employing a heavy-ball [26] or inertia factor, h, that can take on values [0,1]. By utilizing h, abrupt changes in the gradient will be diluted because previous search directions are also included in the calculation of the current search direction meaning,

$$\mathbf{q}_i = -\nabla_{\mathbf{x}} J_p(\mathbf{x}_{i-1}) + h\, \mathbf{q}_{i-1}. \tag{3.13}$$

The inclusion of h also influences the oscillation of the solution path, by including the previous gradients, we have a "heavier ball" which means it bounces less. But in the case that the inclusion of previous iterations are negatively affecting the search direction, by causing it to not be a descent direction, the current search direction is reset.

While *steepest descent* is a good method, the convergence can be rather slow, especially compared to Newton's method. A convergence rate better than Newton's method will not be attainable but determining the step-length, μ_k will either improve or deteriorate the convergence. One way to encourage convergence is by ensuring that the cost function is experiencing an acceptable reduction at each iteration. Which is exactly the purpose of a popular line search condition shown in (3.14). The *sufficient decrease* condition [42] evaluates the reduction in the cost function and ensures that it is proportional to both the step length and directional derivative, $\left(\nabla_{\mathbf{x}} J_p(\mathbf{x}_{i-1})\right)^T \mathbf{q}_i$. As (3.14) displays, the right-hand side takes on the form of, $mx + b$, a slope-intercept equation. In this case, the slope of

this equation is negative, therefore, we are evaluating the proposed step-size and ensuring that the result will be below the line defined by $J_p(\mathbf{x}_{i-1}) + c_1\,\mu_i\,\left(\nabla_{\mathbf{x}} J_p(\mathbf{x}_{i-1})\right)^T \mathbf{q}_i$

$$J_p(\mathbf{x}_{i-1} + \mu_i\,\mathbf{q}_i) \leq J_p(\mathbf{x}_{i-1}) + c_1\,\mu_i\,\left(\nabla_{\mathbf{x}} J_p(\mathbf{x}_{i-1})\right)^T \mathbf{q}_i. \tag{3.14}$$

Note that this only encourages convergence, it does not ensure convergence, and therefore this condition alone is a necessary but not sufficient condition. The sufficient decrease, also known as the *Armijo* condition, is typically paired with the curvature condition [42] that calculates the slope of the updated cost function to assess the progress in comparison with the previous iteration. Another option to pair with the sufficient decrease condition [42] is to use backtracking for calculation of the step size, which is the method chosen for optimization here. This backtracking step will evaluate the first Wolfe condition and if it is not met, will decrease the step size until the condition is met. Combining this information, the procedure for optimization is summarized in Table 1.

Table 1: GISL Gradient Optimization of parameterized waveforms [12]

1:	**Initialize**: $M, BT, \mathbf{B}, \mathbf{x}_0, p, N, \mathbf{q}_0 = \mathbf{0}_{N\times 1}, h, \mu_0, \rho_{up}, \rho_{down}$, and c
2:	**Repeat**:
3:	Evaluate: $J_p(\mathbf{x}_{i-1}), \nabla_{\mathbf{x}} J_p(\mathbf{x}_{i-1})$
4:	$\mathbf{q}_i = -\nabla_{\mathbf{x}} J_p(\mathbf{x}_{i-1}) + h\,\mathbf{q}_{i-1}$
5:	**If** $\left(\nabla_{\mathbf{x}} J_p(\mathbf{x}_{i-1})\right)^T \mathbf{q}_i \geq 0$
6:	$\mathbf{q}_i = -\nabla_{\mathbf{x}} J_p(\mathbf{x}_{i-1})$
7:	**End**
8:	**While** $J_p(\mathbf{x}_{i-1} + \mu_i\,\mathbf{q}_i) > J_p(\mathbf{x}_{i-1}) + c_1\,\mu_i\,\left(\nabla_{\mathbf{x}} J_p(\mathbf{x}_{i-1})\right)^T \mathbf{q}_i$
9:	$\mu_i = \rho_{down}\,\mu_i$
10:	**end**
11:	$\mathbf{x}_i = \mathbf{x}_{i-1} + \mu\,\mathbf{q}_i$
12:	$\mu = \rho_{up}\,\mu$
13:	$i = i + 1$
14:	**Until** $i = I$ **or** $\left\|\nabla_{\mathbf{x}} J_p(\mathbf{x}_i)\right\| < g_{min}$,

where ρ_{down} is the backtracking parameter and ρ_{up} increases in the step-size. Following this procedure is how the optimization was performed for the results found in chapter 4 and 5.

3.3.2 Gradient Derivation

The gradient of the GISL cost function was fully derived by Mohr. Therefore, it is not included and the reader should refer to [12] for reference.

3.3.2.1 Over-Coded Gradient Derivation

Here we want to utilize over-coded PCFM, but need a means of enforcing spectral containment. We suspect that by using similar techniques from [15], that by accounting for range straddling effects within the optimization, it will provide an implicit constraint on the resulting waveform's spectral footprint. In [15] subsample shifts were included in the GISL metric; for this thesis we will be acting similarly but instead of subsample shifts, we will be taking advantage of the Fourier relationship between a sample-shift and phase-shift. Therefore, also taking advantage of the DFT and inverse DFT matrices in (3.7) and including a phase-shift vector, **v**.

What is range straddling? As we know from previous sections, the receiver captures the signal, the ADC samples that returned signal, and matched filtering occurs. If the sampled signal does not contain the theoretical peak value, there will be a loss in SNR, which is known as *straddle loss* [1,2,43]. This occurs because the ADC is sampling on either side of the peak, meaning the peak occurs between two samples. The largest straddle loss occurs at a half-sample-shift, i.e., $\tau = 0.5$, and is calculated as,

$$L = 20 \cdot \log_{10} \left| \frac{r(\tau)}{r(0)} \right|_{\tau=0.5}. \tag{3.15}$$

In Figure 3-3, an example of an autocorrelation response sampled correctly and an autocorrelation response that includes a half-sample-shift is illustrated.

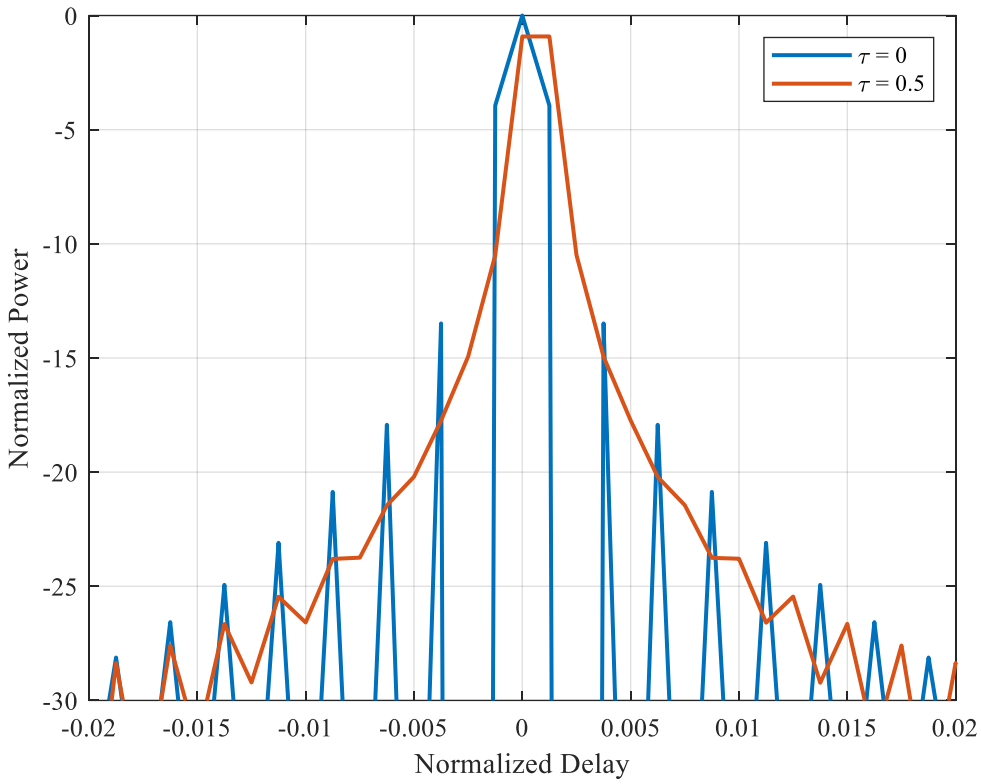

Figure 3-3: Autocorrelation with and without range-straddling

Our aim is to reduce this loss, which can be done by reducing the amplitude difference between the peak and nearest sample. Inherently by reducing this amplitude difference, we also end up widening the mainlobe. The mainlobe broadening will therefore implicitly constrain the spectrum, at least that is our hope.

The inclusion of $\mathbf{v}$ does slightly alter the GISL cost function and therefore, also effects the gradient.

$$\begin{aligned}\mathbf{r}_{\mathrm{L}} &= \mathbf{A}^{H}\left[\left((\mathbf{A}\bar{\mathbf{s}}) \odot \mathbf{v}\right) \odot (\mathbf{A}\bar{\mathbf{s}})^{*}\right] \\ &= \mathbf{A}^{H}(|\mathbf{A}\bar{\mathbf{s}}|^{2} \odot \mathbf{v}).\end{aligned} \tag{3.16}$$

In [12], the gradient derivation included a simplification due to the conjugate symmetry of the autocorrelation about zero-delay. But here, the addition of the phase-shift term $\mathbf{v}$ means that conjugate-symmetric characteristic does not hold anymore. Which makes the derivation more difficult to do if we employed the same methodology as used previously. Therefore, using (3.16) with

the GISL cost function, we can derive the gradient using an "inside-out" method by expanding out the terms in the cost function,

$$
\begin{aligned}
J_p &= \frac{\|\mathbf{w}_{\mathrm{SL}} \odot \mathbf{r}_L\|_p^2}{\|\mathbf{w}_{\mathrm{ML}} \odot \mathbf{r}_L\|_p^2} \\
&= \left(\frac{\mathbf{w}_{\mathrm{SL}}|\mathbf{r}_L|^p}{\mathbf{w}_{\mathrm{ML}}|\mathbf{r}_L|^p}\right)^{2/p} \\
&= \left(\frac{\mathbf{w}_{\mathrm{SL}}|\mathbf{A}^H(|\mathbf{A}\bar{\mathbf{s}}|^2 \odot \mathbf{v})|^p}{\mathbf{w}_{\mathrm{ML}}|\mathbf{A}^H(|\mathbf{A}\bar{\mathbf{s}}|^2 \odot \mathbf{v})|^p}\right)^{2/p} \\
&= \left(\frac{\mathbf{w}_{\mathrm{SL}}|\mathbf{A}^H(|\mathbf{A}(\exp(j\mathbf{B}\mathbf{x})|^2 \odot \mathbf{v})|^p}{\mathbf{w}_{\mathrm{ML}}|\mathbf{A}^H(|\mathbf{A}(\exp(j\mathbf{B}\mathbf{x})|^2 \odot \mathbf{v})|^p}\right)^{2/p}.
\end{aligned}
\tag{3.17}
$$

From (3.17), our goal is take the gradient of J_p with respect to the parameters in $\mathbf{x}$. The "inside-out" method breaks the cost function down into steps, from the inner most term that is a function of the parameters outwards. It relies heavily on the *complex chain rule* to determine the derivative at each subsequent stages and then piece it all back together. With that being said, the first stage of our cost function gradient, takes the partial derivative of the waveform phase with respect to the parameters, where $\mathbf{B} \in \mathbb{R}^{M\times N}$, $\boldsymbol{\phi} \in \mathbb{R}^M$

$\boldsymbol{\phi} = \mathbf{B}\mathbf{x}$:

$$
\begin{aligned}
\frac{\partial}{\partial x_n}\phi_m &= \frac{\partial \phi_m}{\partial x_n}\frac{\partial}{\partial \phi_m} + \frac{\partial \phi_m^*}{\partial x_n}\frac{\partial}{\partial \phi_m^*} \\
&= \frac{\partial \phi_m}{\partial x_n}\frac{\partial}{\partial \phi_m} + 0.
\end{aligned}
\tag{3.18}
$$

Due to the matrix multiplication $\mathbf{B}\mathbf{x}$ increasing the dimension from $\mathbb{R}^N \rightarrow \mathbb{R}^M$, in order evaluate the partial derivative of the phase vector with respect to the parameters, we have to utilize the Jacobian - $\mathbf{J}_{\boldsymbol{\phi}}(\mathbf{x})$, meaning,

$$\nabla_{\mathbf{x}} = \mathbf{J}_{\boldsymbol{\phi}}(\mathbf{x})\, \nabla_{\boldsymbol{\phi}}$$

$$= \begin{bmatrix} \frac{\partial \phi_1}{\partial x_1} & \cdots & \frac{\partial \phi_M}{\partial x_1} \\ \vdots & \ddots & \vdots \\ \frac{\partial \phi_1}{\partial x_N} & \cdots & \frac{\partial \phi_M}{\partial x_N} \end{bmatrix}$$

$$= \mathbf{B}^T \nabla_{\boldsymbol{\phi}}. \tag{3.19}$$

From (3.19), our next step will be evaluating the waveform gradient with respect to the phase, where the waveform is zero-padded and complex, $\bar{\mathbf{s}} \in \mathbb{C}^{2M}$,

$\bar{\mathbf{s}} = \exp(j\boldsymbol{\phi})$:

$$\nabla_{\boldsymbol{\phi}} = \mathbf{J}_{\bar{\mathbf{s}}}(\boldsymbol{\phi})\, \nabla_{\bar{\mathbf{s}}}$$

$$\frac{\partial}{\partial \phi_m}\, \bar{s}_i = \frac{\partial \bar{s}_i}{\partial \phi_m} \frac{\partial}{\partial \bar{s}_i} + \frac{\partial \bar{s}_i{}^*}{\partial \phi_m} \frac{\partial}{\partial \bar{s}_i{}^*}$$

$$= j\bar{s}_m \frac{\partial}{\partial \bar{s}_m} - j\bar{s}_m^* \frac{\partial}{\partial \bar{s}_m{}^*}$$

$$= 2\Im\left\{\bar{s}_m^*\, \frac{\partial}{\partial \bar{s}_m^*}\right\} = 2\,\Im\{\bar{\mathbf{s}}^* \odot \nabla_{\bar{\mathbf{s}}^*}\}. \tag{3.20}$$

And in (3.17) the waveform is being multiplied by the DFT matrix, therefore, $\mathbf{A}, \mathbf{g} \in \mathbb{C}^{2M}$

$\mathbf{g} = \mathbf{A}\bar{\mathbf{s}}$:

$$\nabla_{\bar{\mathbf{s}}^*} = \mathbf{J}_{\mathbf{g}}(\bar{\mathbf{s}}^*)\, \nabla_{\mathbf{g}}$$

$$\frac{\partial}{\partial \bar{s}_m^*}\, g_i = \frac{\partial g_i}{\partial \bar{s}_m^*} \frac{\partial}{\partial g_i} + \frac{\partial g_i{}^*}{\partial \bar{s}_m^*} \frac{\partial}{\partial g_i{}^*}$$

$$= 0 + \frac{\partial}{\partial g_i^*} \sum_j^{2M} \frac{\partial}{\partial \bar{s}_m^*} \left(a_{ij}^* \bar{s}_j^*\right)$$

$$= \frac{\partial}{\partial g_i^*} \sum_j^{2M} a_{im}^*$$

$$= \mathbf{A}^H\, \nabla_{\mathbf{g}^*}. \tag{3.21}$$

Taking this to evaluate $|\mathbf{A}\bar{\mathbf{s}}|^2 \in \mathbb{R}^{2M}$ we find the following,

$\mathbf{y} = |\mathbf{A}\bar{\mathbf{s}}|^2 = |\mathbf{g}|^2$:

$$\nabla_{\mathbf{g}^*} = \mathbf{J}_{\mathbf{y}}(\mathbf{g}^*)\,\nabla_{\mathbf{y}}$$

$$\frac{\partial}{\partial g_m^*} y_i = \frac{\partial y_i}{\partial g_m^*}\frac{\partial}{\partial y_i} + \frac{\partial y_i{}^*}{\partial g_m^*}\frac{\partial}{\partial y_i{}^*}$$

$$= \frac{\partial}{\partial g_m^*}\, g_i\, g_i^* \frac{\partial}{\partial y_i}$$

$$= g_m \frac{\partial}{\partial y_m}$$

$$= \mathbf{g} \odot \nabla_{\mathbf{y}}. \tag{3.22}$$

Still following this inside-out method, $|\mathbf{A}\bar{\mathbf{s}}|^2$ is then phase-shifted making the next stage and due to the phase shift vector, we now have, $\mathbf{v}, \mathbf{h} \in \mathbb{C}^{2M}$

$\mathbf{h} = |\mathbf{A}\bar{\mathbf{s}}|^2 \odot \mathbf{v} = \mathbf{y} \odot \mathbf{v}$:

$$\nabla_{\mathbf{y}} = \mathbf{J}_{\mathbf{h}}(\mathbf{y})\,\nabla_{\mathbf{h}}$$

$$\frac{\partial}{\partial y_m} h_i = \frac{\partial h_i}{\partial y_m}\frac{\partial}{\partial h_i} + \frac{\partial h_i{}^*}{\partial y_m}\frac{\partial}{\partial h_i{}^*}$$

$$= \frac{\partial}{\partial y_m}\, y_i\, v_i \frac{\partial}{\partial h_i} + \frac{\partial}{\partial y_m} y_i\, v_i^* \frac{\partial}{\partial h_i{}^*}$$

$$= v_m \frac{\partial}{\partial h_m} + v_m^* \frac{\partial}{\partial h_m^*}$$

$$= 2\Re\left\{v_m^* \frac{\partial}{\partial h_m^*}\right\} = 2\,\Re\{\mathbf{v}^* \odot \nabla_{\mathbf{h}^*}\}. \tag{3.23}$$

The next stage is the autocorrelation function previously defined in (3.16),

$\mathbf{r} = \mathbf{A}^H(|\mathbf{A}\bar{\mathbf{s}}|^2 \odot \mathbf{v}) = \mathbf{A}^H\,\mathbf{h}$:

$$\nabla_{\mathbf{h}^*} = \mathbf{J}_{\mathbf{r}}(\mathbf{h}^*)\,\nabla_{\mathbf{r}}$$

$$\frac{\partial}{\partial h_m^*} r_i = \frac{\partial r_i}{\partial h_m^*}\frac{\partial}{\partial r_i} + \frac{\partial r_i^*}{\partial h_m^*}\frac{\partial}{\partial r_i^*}$$

$$= \frac{\partial}{\partial r_i^*}\sum_j^{2M}\frac{\partial}{\partial h_m^*}\left(a_{ij}\,h_j^*\right)$$

$$= \frac{\partial}{\partial r_i^*}\sum_j^{2M} a_{im}$$

$$= \mathbf{A}\,\nabla_{\mathbf{r}^*}. \tag{3.24}$$

Again, using the same guidelines as discussed previously when dealing with a real-valued function of a complex variable, we find,

$\boldsymbol{\eta} = |\mathbf{r}|^p = (\mathbf{r} \odot \mathbf{r}^*)^{(p/2)}$:

$$\nabla_{\mathbf{r}^*} = \mathbf{J}_{\boldsymbol{\eta}}(\mathbf{r}^*)\,\nabla_{\boldsymbol{\eta}}$$

$$\frac{\partial}{\partial r_m^*}\eta_i = \frac{\partial \eta_i}{\partial r_m^*}\frac{\partial}{\partial \eta_i} + \frac{\partial \eta_i{}^*}{\partial r_m^*}\frac{\partial}{\partial \eta_i{}^*}$$

$$= \frac{\partial}{\partial r_m^*}\left(r_i\,r_i^*\right)^{p/2}\frac{\partial}{\partial \eta_i}$$

$$= \frac{p}{2}\left(r_m\,r_m^*\right)^{(p/2-1)}\frac{\partial}{\partial r_m^*}\left(r_i\,r_i^*\right)\frac{\partial}{\partial \eta_i}$$

$$= \frac{p}{2}\left(r_m\,r_m^*\right)^{(p/2-1)} r_m\,\frac{\partial}{\partial\,\eta_m} = \frac{p}{2}\,|\mathbf{r}|^{(p-2)} \odot \mathbf{r} \odot \nabla_{\boldsymbol{\eta}}. \tag{3.25}$$

Finally, we are to the final derivation and evaluate the derivative of the cost function with respect to $\boldsymbol{\eta}$,

$$\frac{\partial}{\partial \eta_m} J_p = \frac{\partial}{\partial \eta_m}\left[\left(\frac{\sum_i^{2M} w_{\mathrm{SL},i}\,\eta_i}{\sum_j^{2M} w_{\mathrm{ML},j}\,\eta_j}\right)^{2/p}\right]$$

$$= \frac{2}{p}\left(\frac{\sum_i^{2M} w_{\mathrm{SL},i}\,\eta_i}{\sum_j^{2M} w_{\mathrm{ML},j}\,\eta_j}\right)^{2/p-1} \frac{\partial}{\partial \eta_m}\left(\frac{\sum_i^{2M} w_{\mathrm{SL},i}\,\eta_i}{\sum_j^{2M} w_{\mathrm{ML},j}\,\eta_j}\right)$$

$$= \frac{2}{p}\,J_p\left(\frac{\sum_i^{2M} w_{\mathrm{SL},i}\,\eta_i}{\sum_j^{2M} w_{\mathrm{ML},j}\,\eta_j}\right)^{-1} \frac{\left(\sum_j^{2M} w_{\mathrm{ML},j}\,\eta_j\right) w_{\mathrm{SL},m} - \left(\sum_i^{2M} w_{\mathrm{SL},i}\,\eta_i\right) w_{\mathrm{ML},m}}{\left(\sum_j^{2M} w_{\mathrm{ML},j}\,\eta_j\right)^2}$$

$$= \frac{2}{p}\,J_p\,\frac{\left(\sum_j^{2M} w_{\mathrm{ML},j}\,\eta_j\right) w_{\mathrm{SL},m} - \left(\sum_i^{2M} w_{\mathrm{SL},i}\,\eta_i\right) w_{\mathrm{ML},m}}{\left(\sum_i^{2M} w_{\mathrm{SL},i}\,\eta_i\right)\left(\sum_j^{2M} w_{\mathrm{ML},j}\,\eta_j\right)}$$

$$= \frac{2}{p}\,J_p\left(\frac{w_{\mathrm{SL},m}}{\sum_i^{2M} w_{\mathrm{SL},i}\,\eta_i} - \frac{w_{\mathrm{ML},m}}{\sum_j^{2M} w_{\mathrm{ML},j}\,\eta_j}\right) = \frac{2}{p}\,J_p\left(\frac{\mathbf{w}_{\mathrm{SL}}}{\mathbf{w}_{\mathrm{SL}}^T|\mathbf{r}|^p} - \frac{\mathbf{w}_{\mathrm{ML}}}{\mathbf{w}_{\mathrm{ML}}^T|\mathbf{r}|^p}\right). \tag{3.26}$$

Piecing everything back together now,

$$\frac{\partial}{\partial \mathbf{x}_n} J_p = 4\,J_p\,\mathbf{B}^T\,\Im\left\{\bar{\mathbf{s}}^* \odot \mathbf{A}^H\left[(\mathbf{A}\bar{\mathbf{s}}) \odot \Re\left\{\mathbf{v}^* \odot \mathbf{A}\left(\left(\frac{\mathbf{w}_{\mathrm{SL}}}{\mathbf{w}_{\mathrm{SL}}^T|\mathbf{r}|^p} - \frac{\mathbf{w}_{\mathrm{ML}}}{\mathbf{w}_{\mathrm{ML}}^T|\mathbf{r}|^p}\right) \odot |\mathbf{r}|^{(p-2)} \odot \mathbf{r}\right)\right\}\right]\right\}. \tag{3.27}$$

Chapter 4 Simulation Results

While waveform implementations like the PCFM and CE-OFDM have a span for their parameters and this plays a role in spectral containment; it was observed in [12] that when randomly initializing within this span can still produce waveforms that have diminished spectral containment. But there is also a need for good initializations because of the effect it has on the optimization, therefore, a waveform that has already undergone spectral shaping will be used for the initialization. The pseudo-random optimized FM (PRO-FM) [35] waveform uses a spectral template based on a shaping parameter to perform spectral shaping via alternating time-frequency projections. The shaping parameter will vary the spectral template from a regular Gaussian spectral density to a rectangular spectral density. Using PRO-FM to initialize 3000 waveforms, all with a $BT = 200$, and $4\times$

oversampling (relative to the 3-dB bandwidth), least-squares is then used to map the phase of the PRO-FM waveform into the parameters for each quasi-basis type. For example, examining the discretized phase of the kth PRO-FM waveform,

$$\phi_{PRO,k} \quad \vdots \quad \xrightarrow{LS\{\mathbf{B}_\alpha\}} \mathbf{x}_{\alpha,k} \quad \vdots \quad \xrightarrow{LS\{\mathbf{B}_\beta\}} \mathbf{x}_{\beta,k} \quad \vdots \quad \xrightarrow{LS\{\mathbf{B}_\gamma\}} \mathbf{x}_{\gamma,k}. \tag{4.1}$$

Using the procedure laid out in Table 1, the GISL gradient optimization was then performed for the case of $p = 8$, which approximates a PSL metric. The convergence behavior when optimizing one waveform for each quasi-basis for a max of 10^6 iterations, typifies the behavior that can be expected when larger waveform sets are optimized. Figure 4-1 illustrates this convergence behavior and we see that even though all three parameterized structures were initialized with the same PRO-FM waveform, there is a difference in starting point. For which we point back to the least-squares mapping that was utilized to determine the parameters for each quasi-basis type. There will be some degradation introduced through this process, which we will see in some of the results later. Although we are initializing with a waveform that has previously undergone a different optimization procedure, the first-order and Fourier cases were still able to achieve a roughly 10 dB improvement in the cost function. But separating the converged upon solution of these two cases is about 10^2 iterations. Meanwhile, as Fourier begins to flat line is when second-order begins to slowly decline, with no notable improvement occurring until 10^4 iterations.

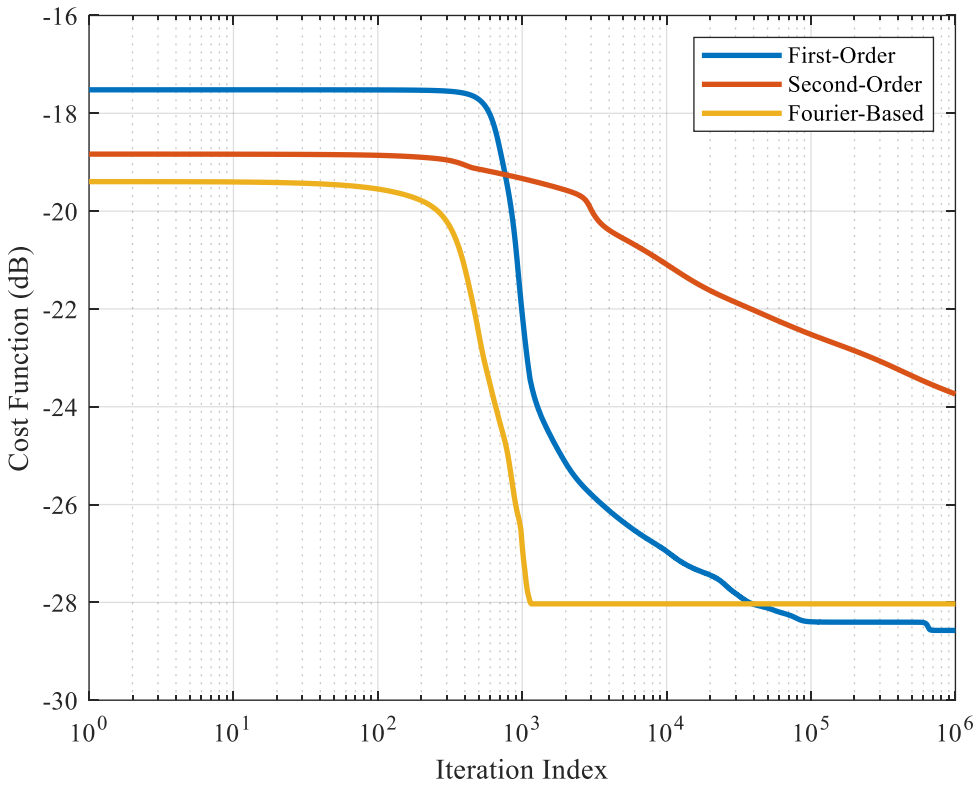

Figure 4-1: Convergence behavior of first-order, second-order, and Fourier quasi-bases using gradient based optimization

For the following results, we are evaluating each quasi-basis type when 3000 waveforms are used for the initialization and the optimization is run for a max of 9000 iterations. Since our cost function has to do with sidelobe levels, it is rather important to evaluate the autocorrelation behavior. Figure 4-2 illustrates both the root-mean-square (RMS) and coherent combining, i.e., slow-time processing of the 3000 unique autocorrelations for each case. Due to the reduction in iterations performed, the RMS and coherent combining results in figure 4.2 display similar outcomes for each quasi-basis type. The Fourier case at 9000 iterations was about 1 dB better than first-order, and first-order was 6 dB below second-order, which is nearly synonymous with the results we see in Figure 4-2. While the sidelobe level is an important attribute to examine, another feature of the autocorrelations appears when we zoom into the mainlobe region. In Figure 4-3 the mainlobe close-up reveals shoulder lobes that are present to varying degrees for all three quasi-bases, the local minima associated with this

effect, poses an explanation for the differing convergence rates. These shoulder lobes are an artifact of the super-Gaussian shaping used for the PRO-FM initialization. This highlights the proficiency of the Fourier quasi-basis to suppress those shoulder lobes, while second-order struggles to make any significant reduction in them. As stated previously, shoulder lobes are an artifact of a super-Gaussian power spectrum, therefore an attribute associated with better spectral containment.

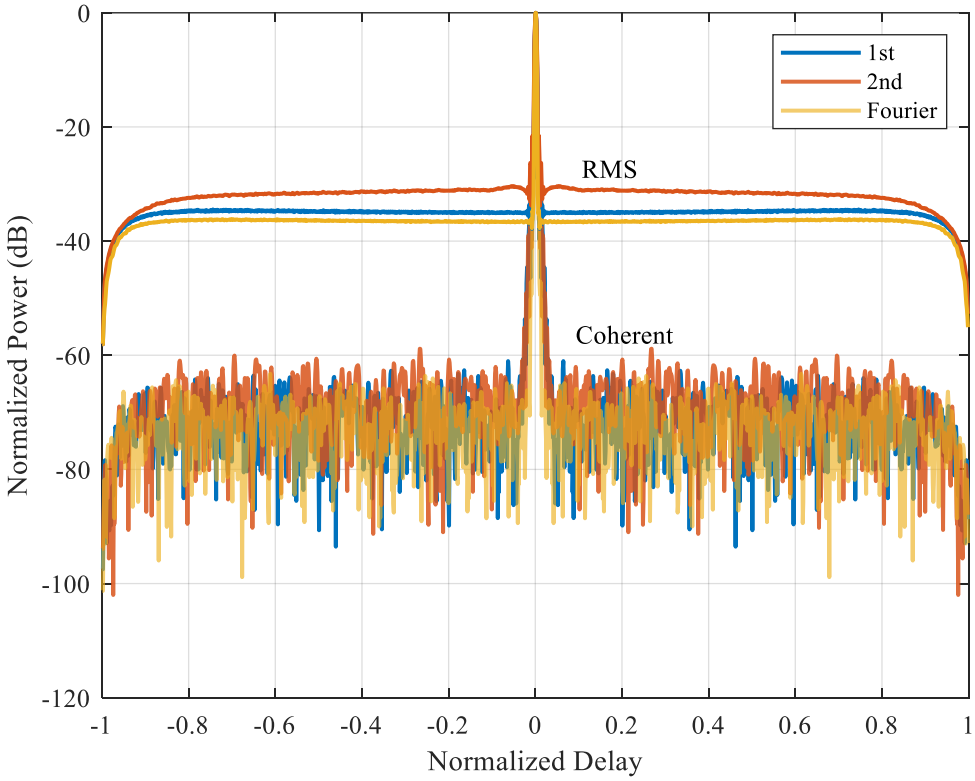

Figure 4-2: RMS and coherent combination of autocorrelations for 3000 unique waveforms for first and second-order PCFM and Fourier quasi-bases

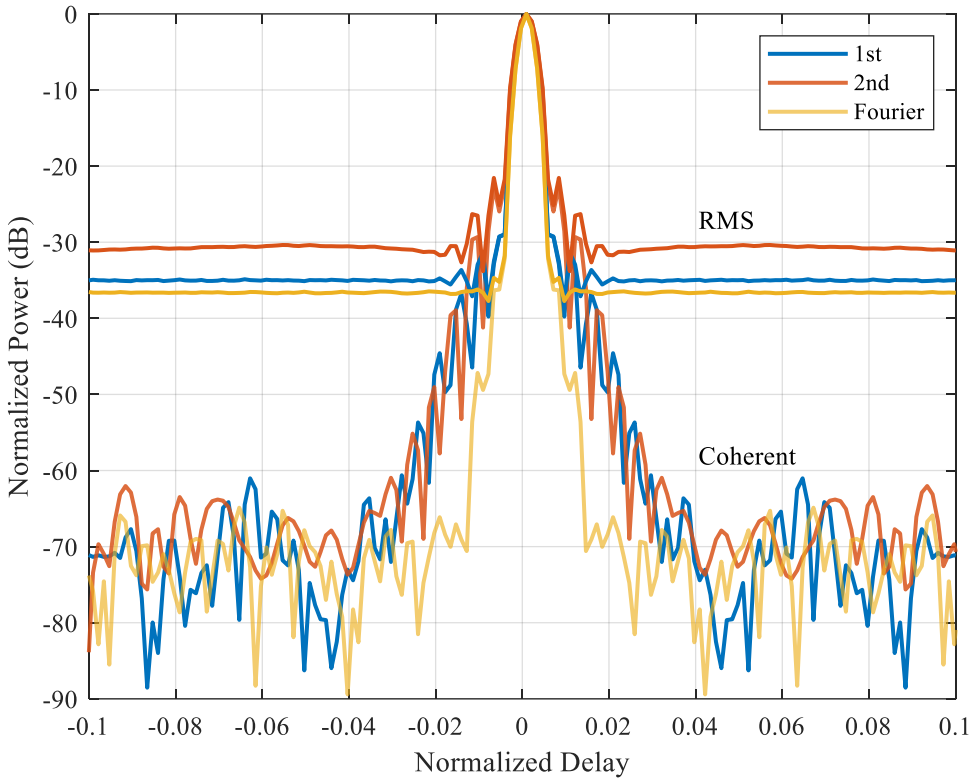

Figure 4-3: RMS and coherent combination of autocorrelations for 3000 unique waveforms optimized for first and second-order PCFM and Fourier quasi-bases (mainlobe close-up)

The autocorrelation is important to examine because it provides us with knowledge regarding the waveforms ability to resolve multiple targets within close proximity, i.e., the *range resolution* and target detectability. While important, this means nothing if the transmitted or received spectrum is essentially white noise. Therefore, we also need to examine the power spectral density (PSD) of all the quasi-basis types. The differing sidelobe levels we saw previously in Figure 4-2 and Figure 4-3 are better understood once we explore the PSD's illustrated in Figure 4-4, Figure *4-5*, and Figure *4-6*. Each of the figures depicts the averaging across the set of 3000 waveforms for each quasi-basis type. For instance, we previously saw that second-order had the highest sidelobe level, along with a slightly wider mainlobe, while the PSD (Figure 4-5) exhibits better spectral containment than both the PRO-FM initialization and the other two quasi-basis types. But the shoulder lobe characteristics that we

saw with first and second-order PCFM are generally associated with better spectral containment. Especially when we examine the roll-off region, we see that second-order is superior to both first-order and Fourier, almost following the roll-off exactly from 3-dB to 10-dB. Previously, Fourier had the best results for the autocorrelation, but we see that the spectrum has suffered, by expanding to the typical random CE-OFDM response of a Gaussian PSD.

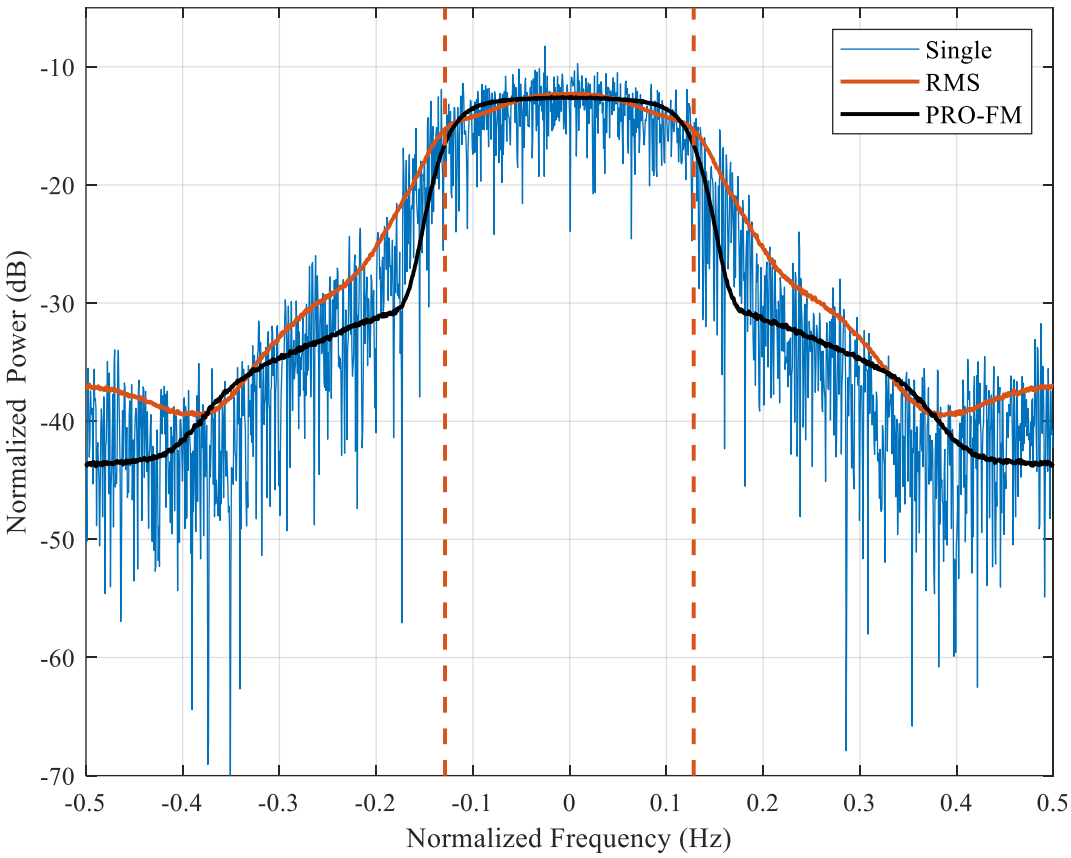

Figure 4-4: Average spectral density over 3000 waveforms using $p = 8$ norm for first-order PCFM quasi-basis

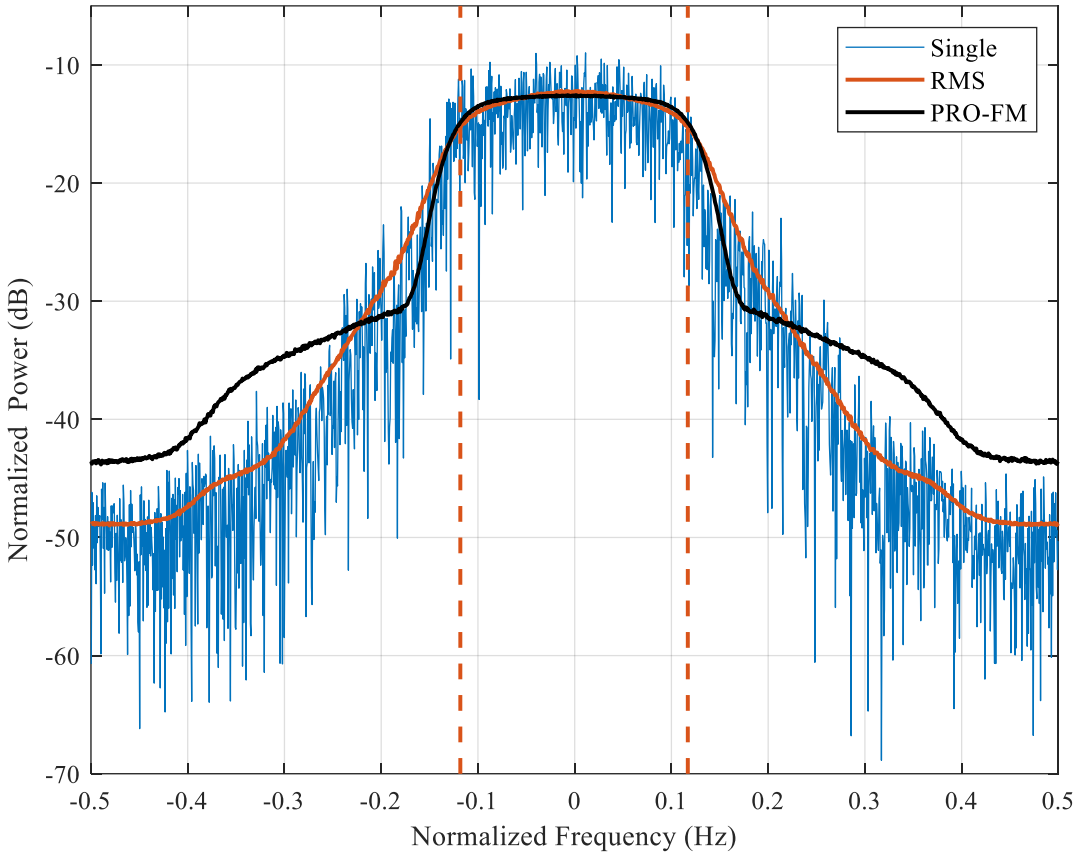

Figure 4-5: Average spectral density over 3000 waveforms optimized using $p = 8$ norm for second-order PCFM quasi-basis

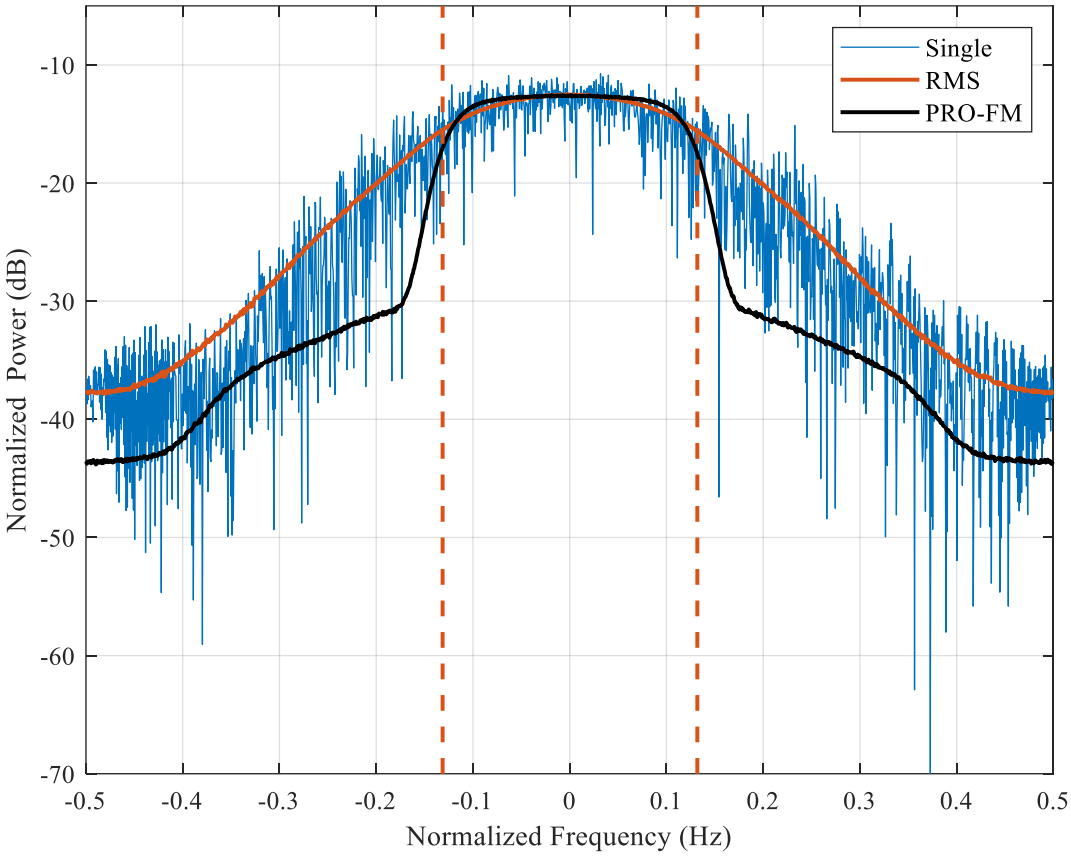

Figure 4-6: Average spectral density over 3000 waveforms optimized using $p = 8$ norm for Fourier quasi-basis

Spectral containment is extremely important, especially in the context of physically realizable waveforms. The signal will undergo spectral filtering due to up-conversion, amplification, and the actual antenna for an analog system. If the waveform is not meeting the spectral considerations, not only will distortion be introduced into the signal, but energy will be dissipated and if severe enough may cause damage to the radar system. The distortion brought on by not meeting the spectral limits will especially cause issues when the signal is passed through the high-power amplifier that typically operates in saturation, which could damage the system. On the other hand, for a digital system the bandwidth is limited by the sampling rate. Therefore, the slow roll-off illustrated for the Fourier

quasi-basis will necessitate the need for higher over-sampling of the discretized waveform representation, which may hinder any use for wideband systems.

The last waveform characteristics we want to examine are the instantaneous phase and frequency behavior. We know that because we are dealing with FM waveforms, the instantaneous phase for each quasi-bases will be continuous. But as we see in Figure 4-7, there is some difference between the behaviors of each quasi-basis type. First-order PCFM exhibits a piecewise linear phase trajectory, which is due to the quasi-basis structure that we showed back in (2.4) and Figure 2-3, that linearly ramps up before remaining constant. Meanwhile, second-order has a smoother undulating behavior, due to the quadratic phase trajectories previously discussed in section 2.2.2, that allows it to perfectly realize the LFM waveform. The infinite differentiability from the sine and cosine terms the form the Fourier quasi-basis also permit it to possess smooth rolling phase trajectories.

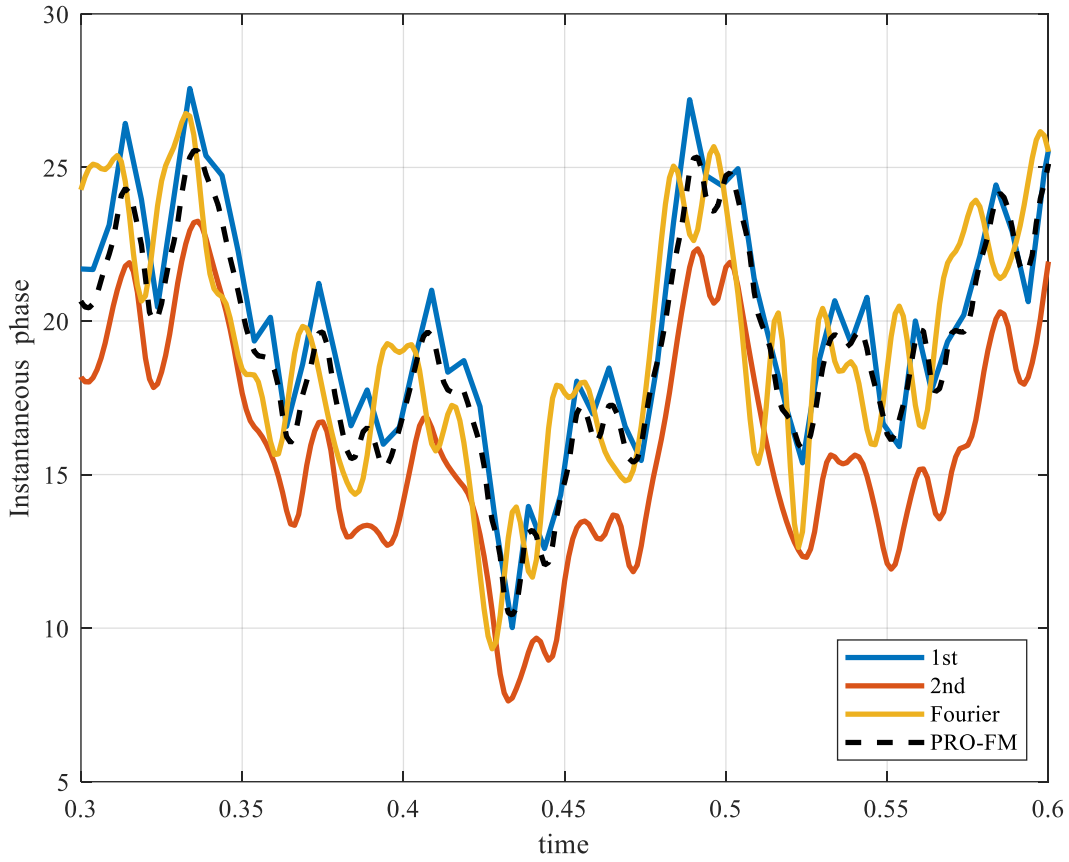

Figure 4-7: Close-up section of instantaneous phase of a single optimized waveform for first and second-order PCFM and Fourier quasi-bases with a PRO-FM initialization

We can obtain the instantaneous frequency by taking the sample-to-sample difference of the individual instantaneous phase functions shown in Figure 4-7. In Figure 4-8, we have the instantaneous frequencies of all three quasi-basis shown against the PRO-FM waveform used for initialization. From this, we see that the first-order PCFM illustrates flat regions immediately followed by discontinuities, which is in agreeance with the groundwork laid out in section 2.2.1. Again, this is due to the use of a rectangular shaping filter that appears in (2.1). Second-order also uses a rectangular shaping filter, but due to the additional integration stage in (2.8), we see in Figure 4-8 that second-order now takes on a piecewise linear instantaneous frequency. The Fourier quasi-basis remains infinitely differentiable; therefore, it still maintains a smooth instantaneous frequency.

Lastly, we do see that the frequency excursions of first-order PCFM and Fourier, do expand past those of PRO-FM, conforming to the expanded 3-dB bandwidth that we saw in Figure 4-4 - Figure 4-6.

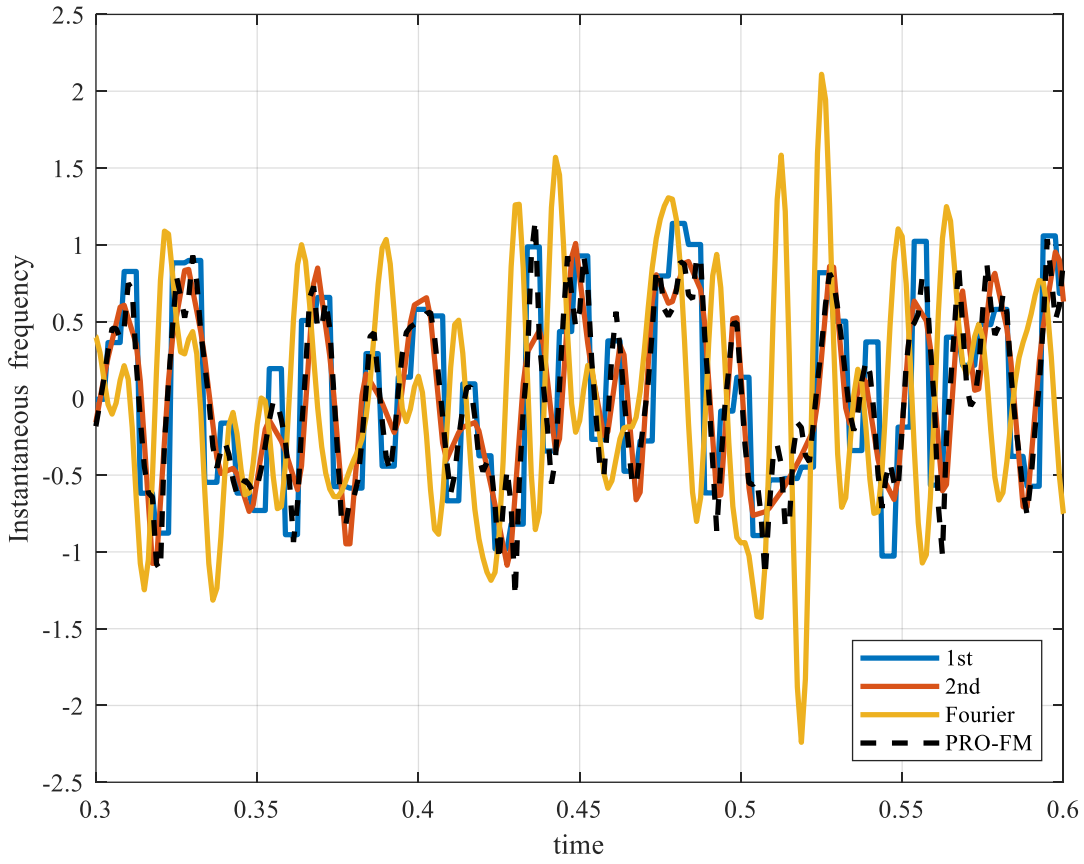

Figure 4-8: Close-up section of instantaneous phase of a single optimized waveform for first and second-order PCFM and Fourier quasi-bases with a PRO-FM initialization

4.1 Over-Coded $L = 2$

For the over-coded simulation, an over-coding factor of $L = 2$, was evaluated. PRO-FM and a least-squares in phase was still employed to initialize the waveform sets for the three quasi-basis types. Utilizing over-coding increases the number of parameters and the size of the quasi-basis, therefore the number of waveforms evaluated was decreased to 1000. As discussed previously, over-coded waveforms tend to expand spectrally during optimization, therefore, the gradient defined in

(3.27), was used with the procedure laid out in Table 1. The optimization was performed for a maximum of 9000 iterations. While the pattern of the convergence behavior is similar to Figure 4-1, the Fourier quasi-basis is fully converged by 300 iterations. Operating in about half the iterations used in the previous optimization. For first-order most of the improvement is done by 100 iterations, but continues decreasing around 2 dB per decade thereafter. Due to the decrease in iterations executed for the $L = 2$ convergence behavior versus the results in Figure 4-1, both first-order and second-order have not fully converged. Lastly, second-order again is very slow to make improvement, not even decreasing 2 dB after 9000 iterations. It is important to point out that the starting point for the cost functions are higher than we previously saw with no over-coding. But when we examine the convergence at 9000 iterations for the previous case, we do see that both first-order and Fourier have decreased further than the $L = 1$ case.

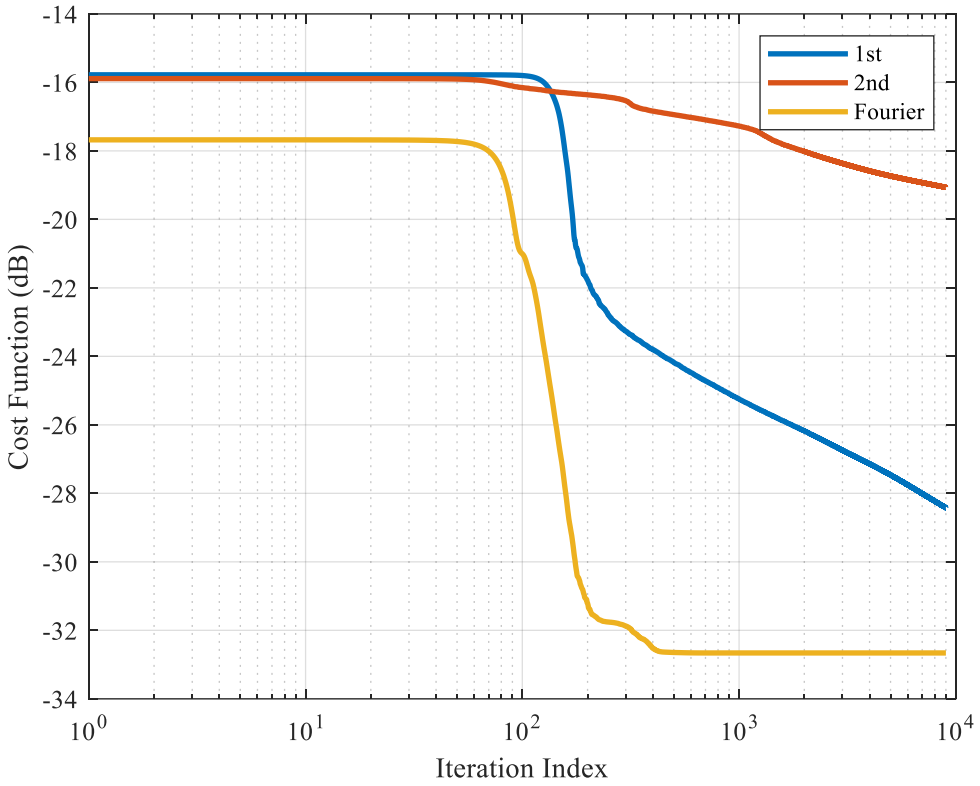

Figure 4-9: GISL cost function convergence for $L = 2$ over-coded first and second-order PCFM and Fourier quasi-bases over 9000 gradient-descent iterations for $p = 8$

Interestingly, due to the increase in convergence rate for the over-coded case, the resulting optimized autocorrelations for first-order and Fourier are remarkably similar to Figure 4-2. In fact, in terms of the RMS autocorrelation, that sidelobe level could be considered better than previous results. While this is promising, we still need to assess the optimized PSD behavior. Synonymous with previous behavior, second-order sidelobe levels are higher compared to the other quasi-bases, but as opposed to the $L = 1$ case, they are about 10 dB higher than the first-order and Fourier quasi-bases.

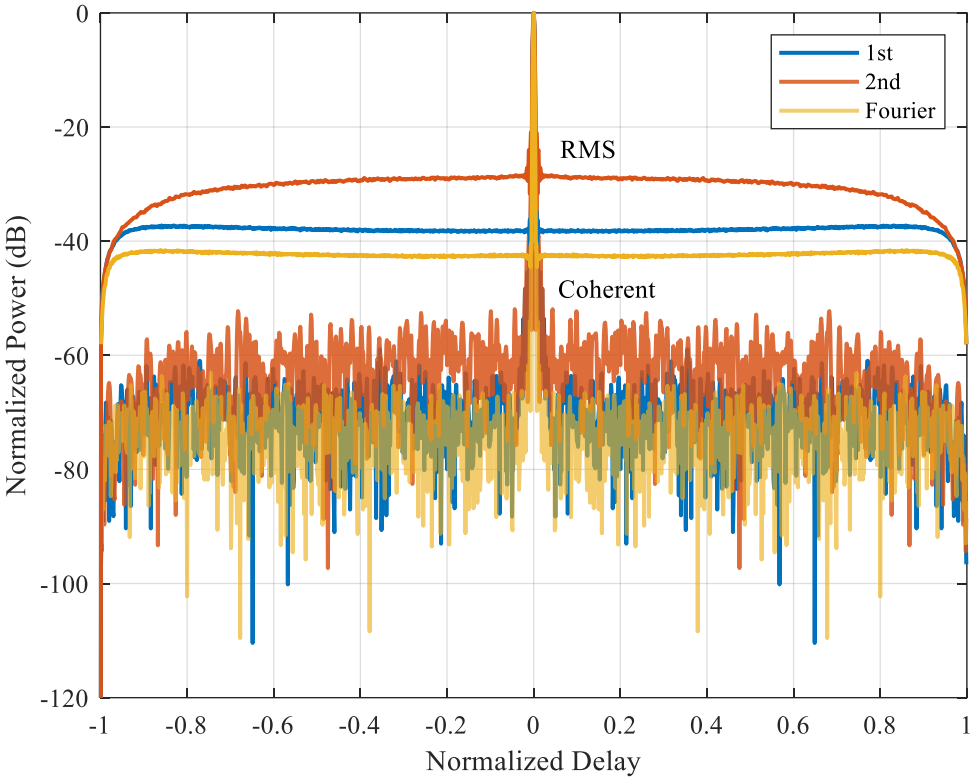

Figure 4-10: RMS and coherent combination of autocorrelations for 1000 unique waveforms optimized for $L = 2$ over-coded first and second-order PCFM and Fourier quasi-bases

Evaluation of the mainlobe region demonstrates that once again, shoulder lobes are the cause of the slower second-order convergence. Meanwhile, first-order and Fourier were both able to largely suppress this characteristic.

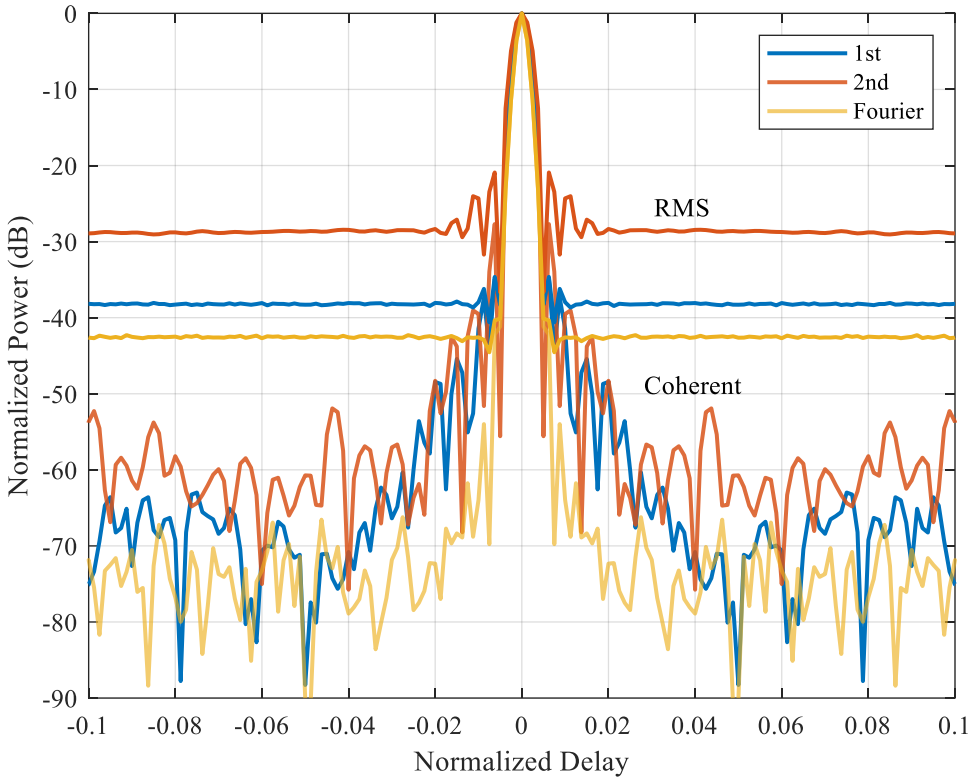

Figure 4-11: RMS and coherent combination of autocorrelations for 1000 waveforms optimized for $L = 2$ over-coded first and second-order PCFM and Fourier quasi-bases (mainlobe close-up)

Recall, as we saw previously, Fourier was largely able to suppress the shoulder lobes, but this was at the cost of a spectral containment. That ability is no different for the over-coded case. In Figure 4-12, the average PSD of 1000 over-coded first-order PCFM waveforms is compared against the average PSD from the PRO-FM initialization. It is hard to discern how much spread has occurred when we compare the 3 dB bandwidth from Figure 4-3. But when the edges are evaluated, we see the roll-off is much more gradual for the $L = 2$ over-coded case, tending more towards a Gaussian PSD.

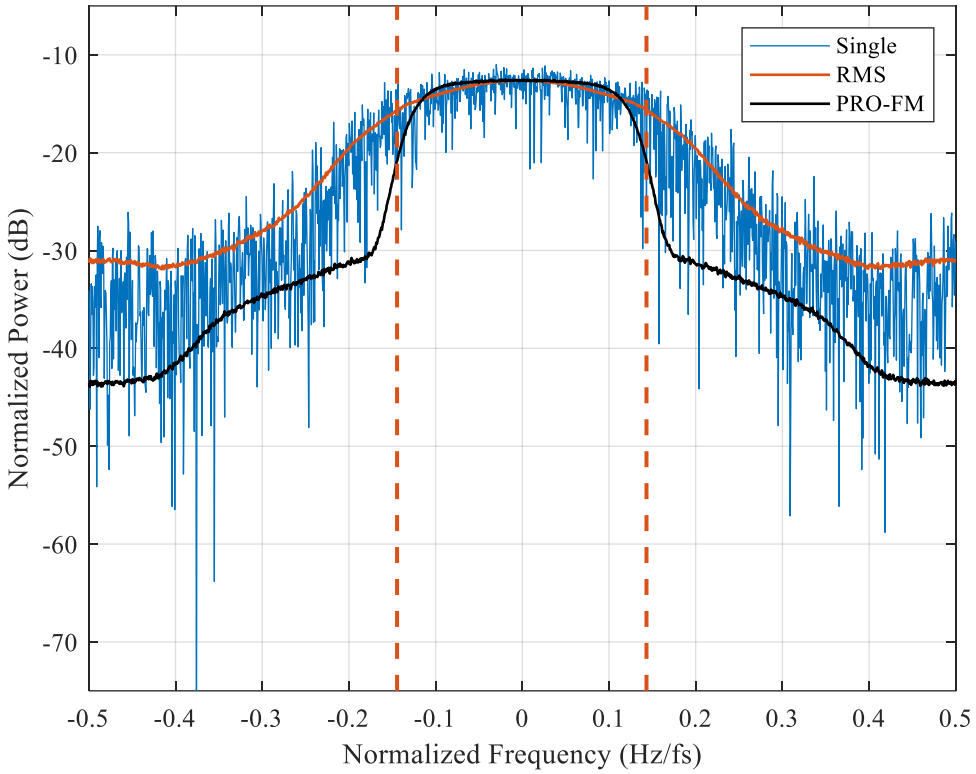

Figure 4-12: Average spectral density over 1000 waveforms optimized using $p = 8$ norm for $L = 2$ over-coded first-order PCFM quasi-basis

Regarding second-order, we saw in Figure *4-11* that the shoulder lobes were still present, but at first glance the average PSD in Figure *4-13* appears to have very poor spectral containment. Meanwhile, the PSD from a single waveform contradicts what the average is depicting. Therefore, evaluating the individual spectral densities from a small subset of these waveforms, reveals that it is not that the spectrum is spreading, but instead that some of the optimized waveforms are producing PSDs that are shifted slightly off baseband, as shown in Figure 4-14. Therefore, taking these optimized waveforms, we can simply shift them back to baseband by changing that final parameter in $\mathbf{x}_\beta$. Revealing in Figure 4-15, that the spectrum maintains tighter containment than both the first and Fourier quasi-bases. While the spectrum is still contained, the results from $L = 2$ over-coded are still inferior to the results shown in Figure 4-4.

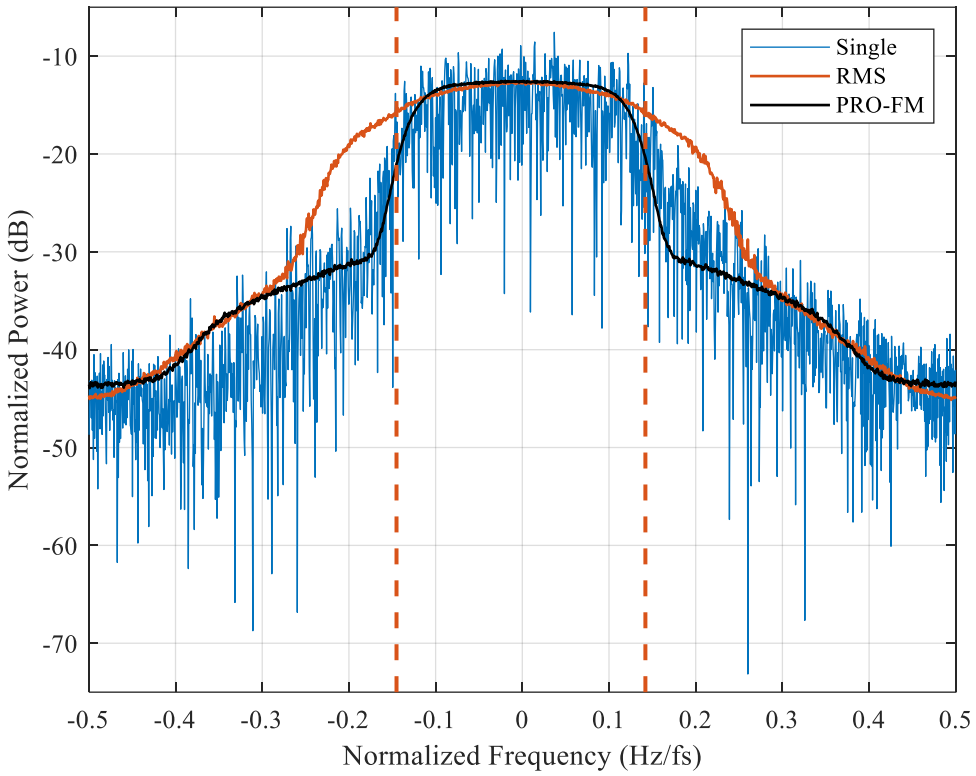

Figure 4-13: Average spectral density over 1000 waveforms optimized using $p = 8$ norm for $L = 2$ over-coded second-order PCFM quasi-basis

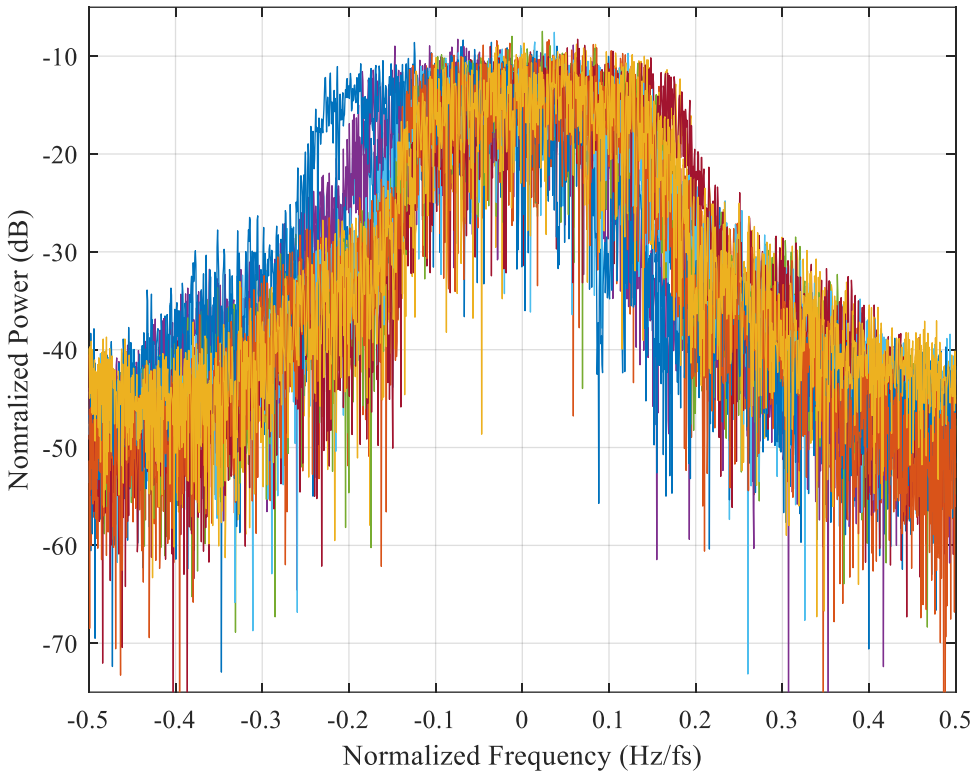

Figure 4-14: Spectral densities of a subset of the 1000 waveforms optimized using $p = 8$ norm for $L = 2$ over-coded second-order PCFM quasi-basis

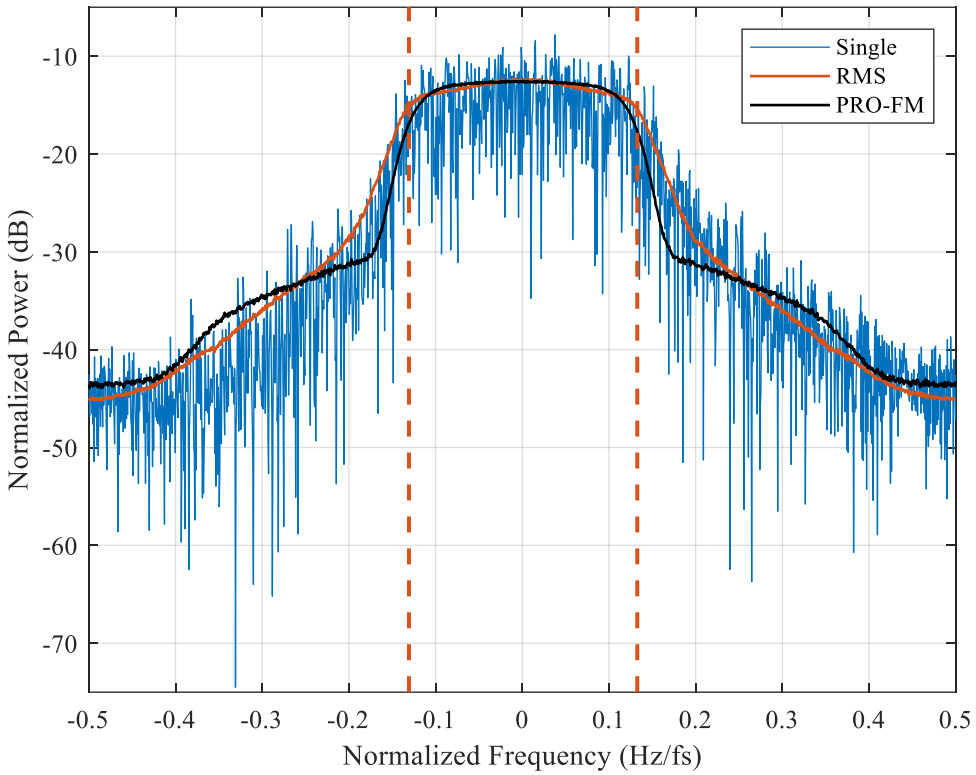

Figure 4-15: Average spectral density over 1000 waveforms optimized using $p = 8$ norm for $L = 2$ over-coded second-order PCFM quasi-basis (individual PSDs shifted back to baseband)

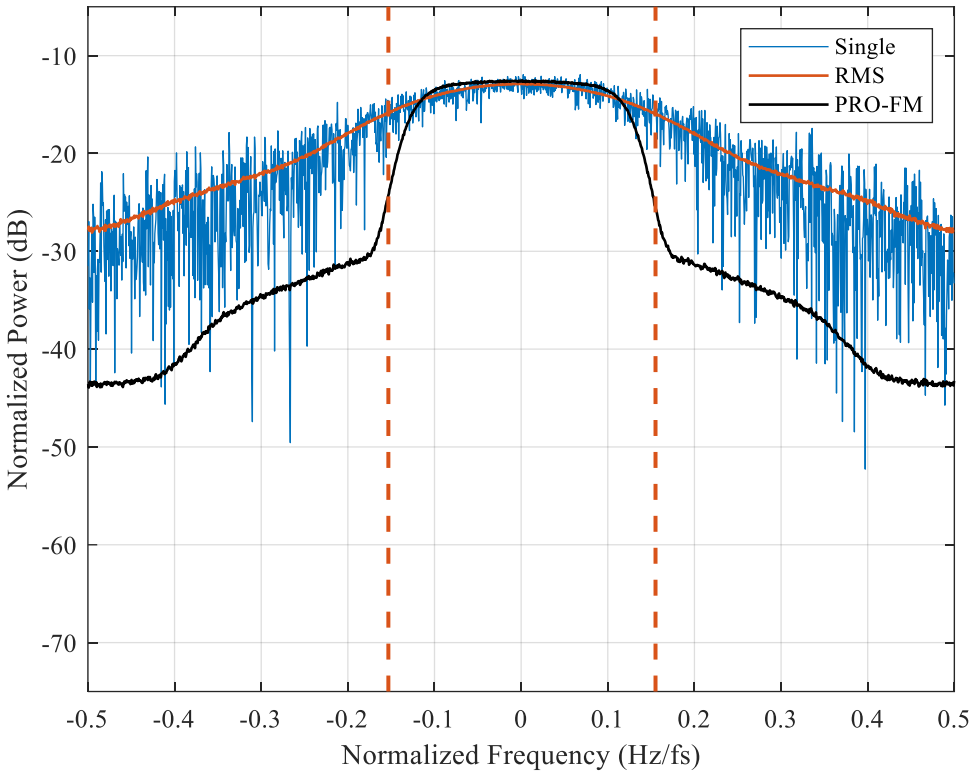

Figure 4-16: Average spectral density over 1000 waveforms optimized using $p = 8$ norm for $L = 2$ over-coded Fourier quasi-basis

Finally, the Fourier PSD is displayed in Figure 4-16. Although the 3 dB bandwidth is a good metric to evaluate, it may not always tell the full story. From Fourier's PSD, the 3 dB bandwidth is not much worse than second-orders, but the roll-off region is. In terms of spectral containment Fourier's is very poor, possessing significant degradation at the roll-off edges and barely maintaining any separation from the noise floor. While the autocorrelation for Fourier has low sidelobes and is great for target detection, the PSD exposes the difficulty hardware will have with this optimized waveform.

The final attribute that is instructive to examine, are the instantaneous phase and frequency behavior for each quasi-basis class, as shown in Figure 4-17 and Figure 4-18. For both the instantaneous phase and frequency examples illustrated here, the second-order case was shifted back to baseband prior to calculation. Or else we would see the instantaneous phase of second-order well outside the bounds shown here. The behavior of the instantaneous phase that we see here, in

terms of smoothness, is the same as we saw previously. The instantaneous frequency exposes just how much the bandwidth is expanding for both the first-order and Fourier cases. First-order's instantaneous frequency nearly expands by 1.6 times the amount, while Fourier is approximately 2.2 times the frequency excursions of the frequency excursions of the PRO-FM initialization.

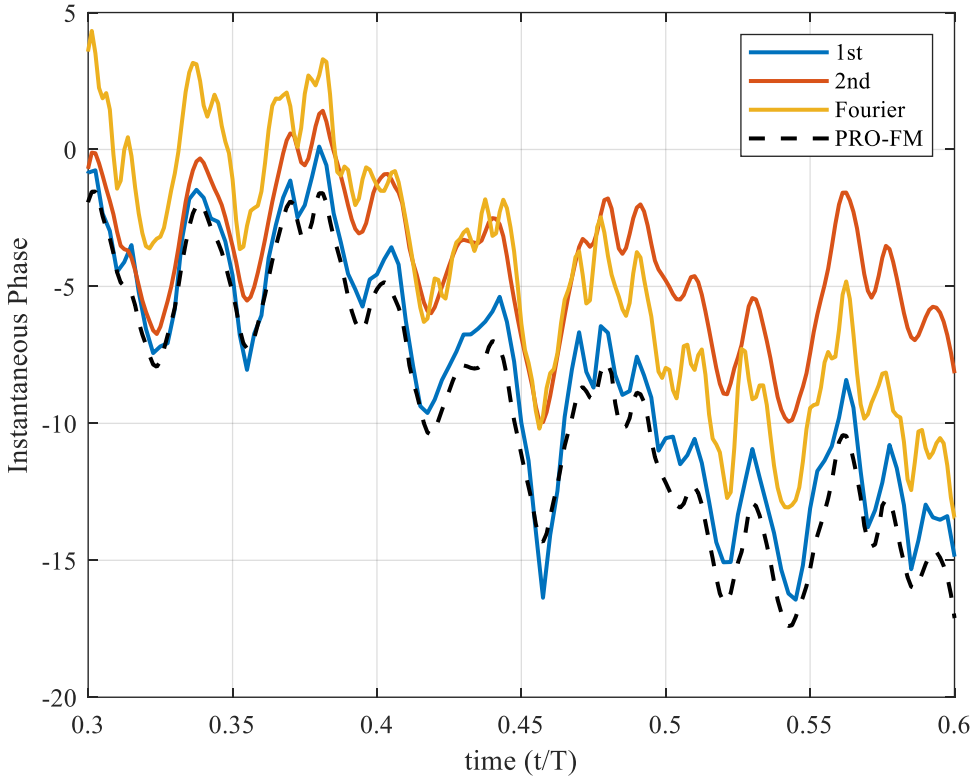

Figure 4-17: Close-up section of instantaneous phase of a single waveform optimized for $L = 2$ over-coded first and second-order PCFM (individual waveforms shifted back to baseband) and Fourier quasi-bases, compared to PRO-FM initialization

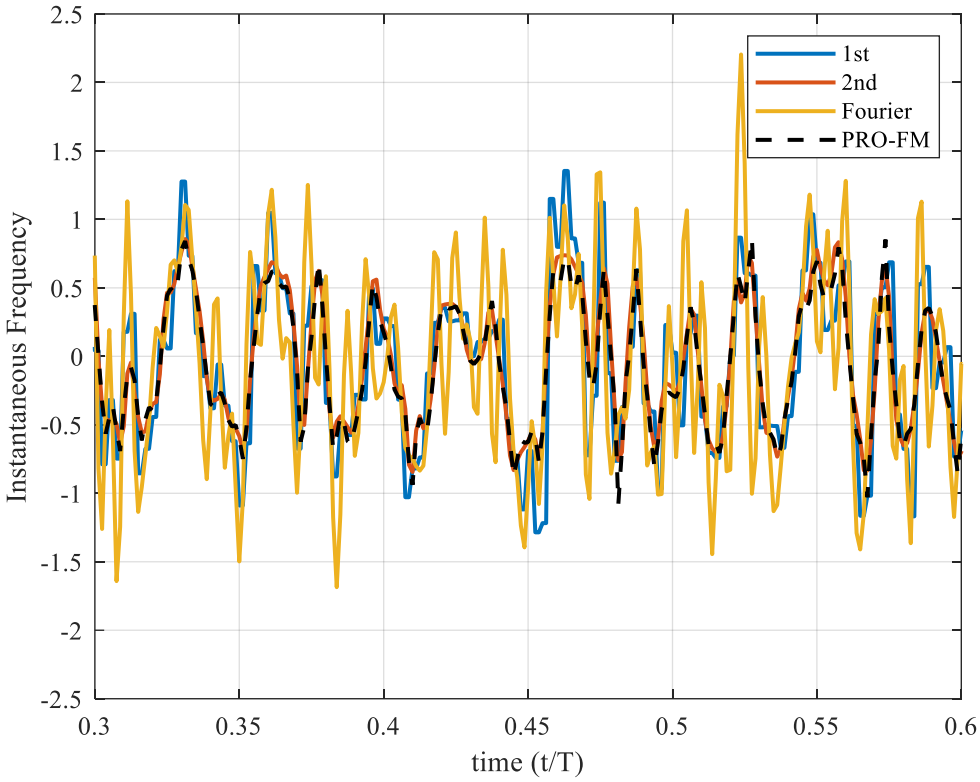

Figure 4-18: Close-up section of instantaneous frequency of a single waveform optimized for $L = 2$ over-coded first and second-order PCFM (individual waveforms shifted back to baseband) and Fourier quasi-bases, compared to PRO-FM initialization

4.2 Over-Coded $L = 4$

When the over-coding factor L is increased to 4, we are now dealing with a fully over-coded waveform, thus a true basis. All other waveform/optimization parameters are kept the same, the only thing changed here was L. Most of the attributes examined such as cost function convergence, autocorrelation behavior, and instantaneous phase have the same behavior as the $L = 2$ case. Where the biggest difference lies in the PSD's of the first-order basis. While difficult to definitively tell from the 3 dB bandwidth lines, the spectral spread is clear when the roll-off region is under question. The noise floor for the first-order basis continues to roll-off for the $L = 4$ case as opposed to stopping around -30 dB. The instantaneous frequency plot highlights how much the spectrum has spread for

the first-order case, expanding by approximately 1.7 times the frequency excursions of the PRO-FM initialization. All other attributes previously examined for the $L = 2$ case are displayed for $L = 4$, but do not possess glaring differences like the PSDs and instantaneous frequency plots. Unfortunately, the analysis for $L = 4$ of the Fourier basis has been left out.

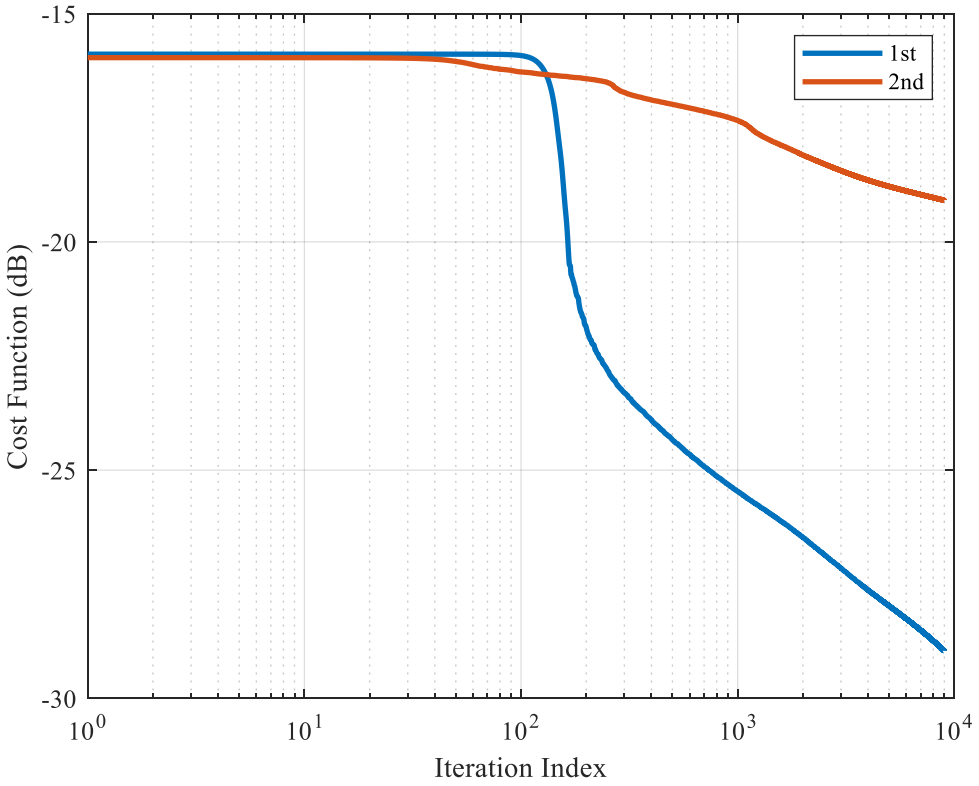

Figure 4-19: GISL cost function convergence for $L = 4$ over-coded first-order PCFM and second-order PCFM quasi-bases over 9000 gradient-descent iterations for $p = 8$

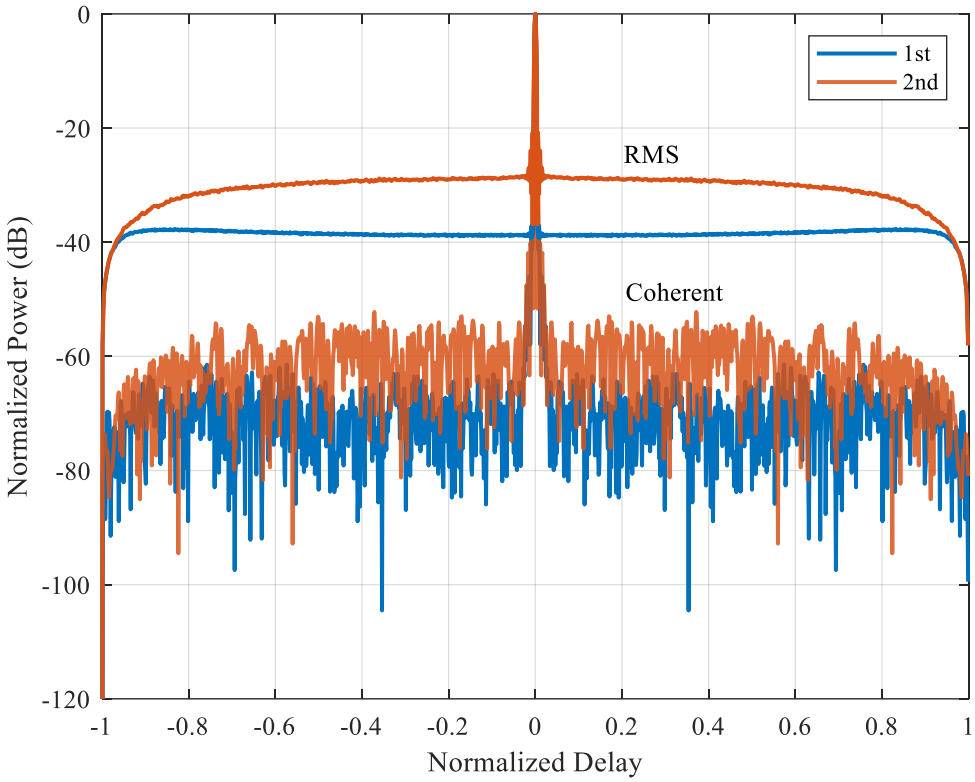

Figure 4-20: RMS and coherent combination of autocorrelations for 1000 unique waveforms optimized for $L = 4$ over-coded first and second-order PCFM quasi-bases

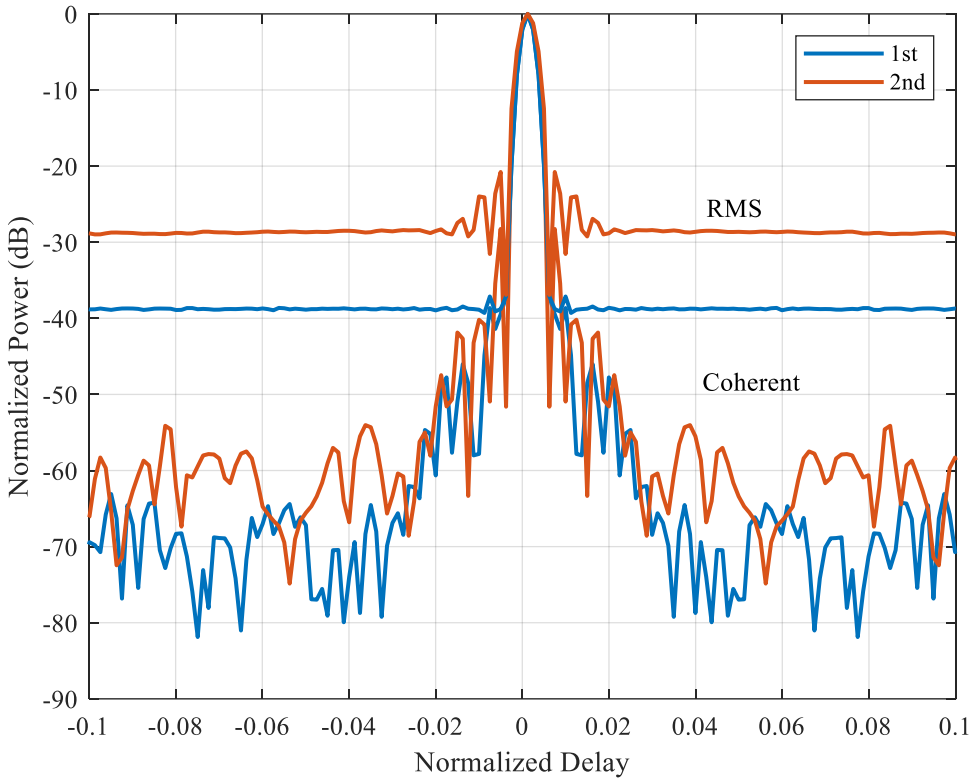

Figure 4-21: RMS and coherent combination of autocorrelations for 1000 unique waveforms optimized for $L = 4$ over-coded first and second-order PCFM quasi-bases (mainlobe close-up)

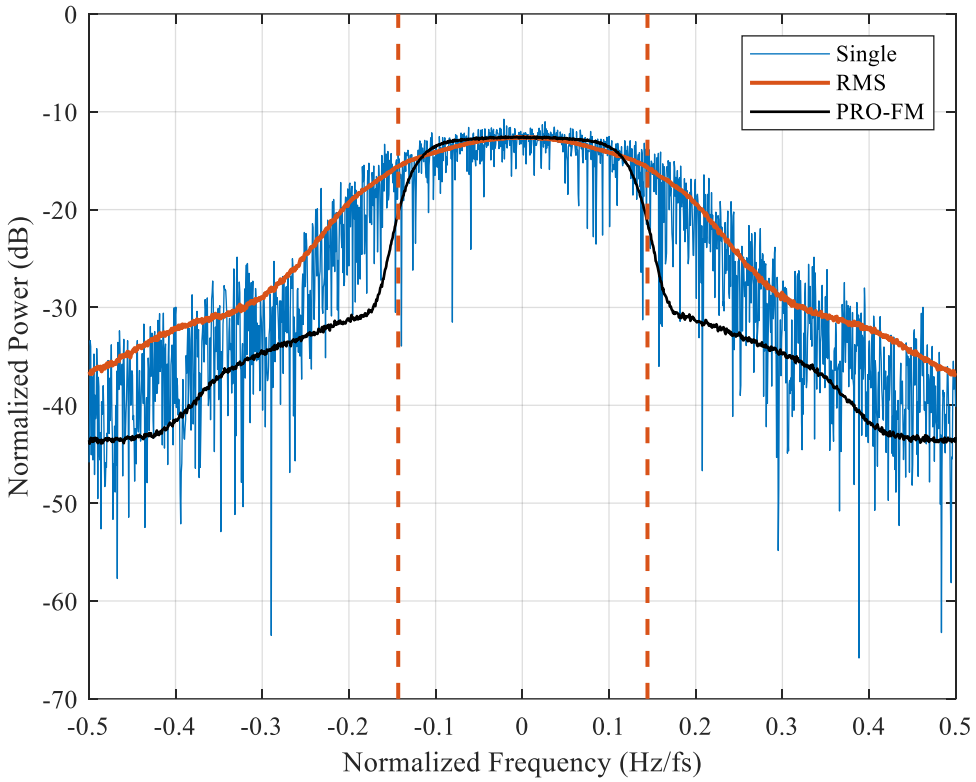

Figure 4-22: Average spectral density over 1000 waveforms optimized using $p = 8$ norm for $L = 4$ over-coded first-order PCFM quasi-basis

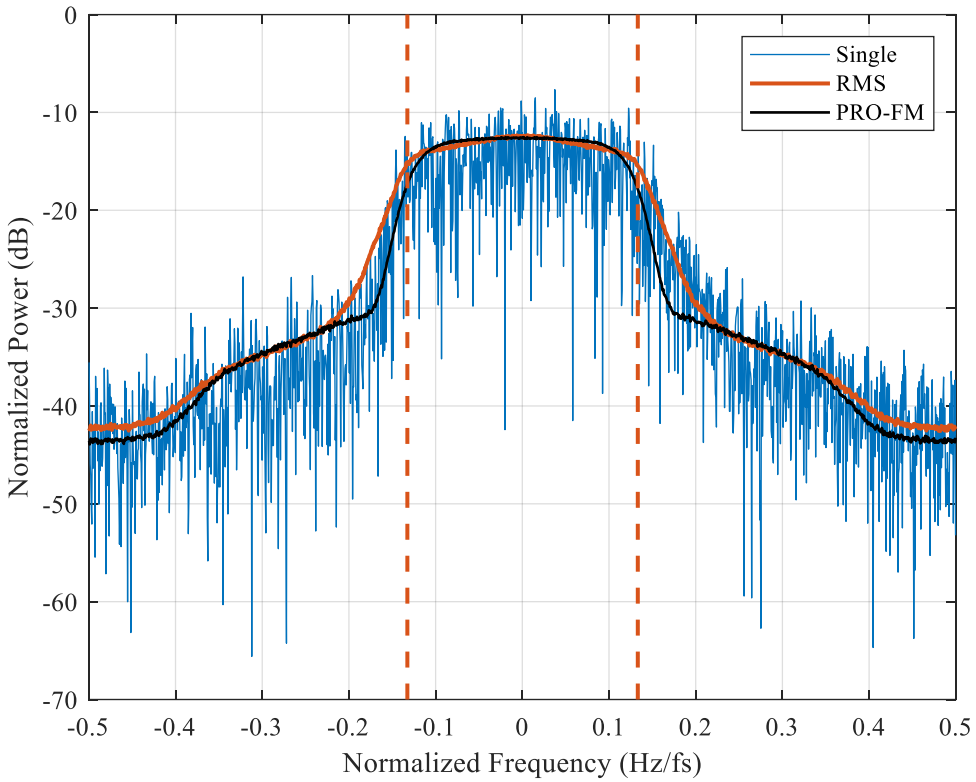

Figure 4-23: Average spectral density over 1000 waveforms optimized using $p = 8$ norm for $L = 4$ over-coded second-order PCFM quasi-basis (individual PSDs shifted back to baseband)

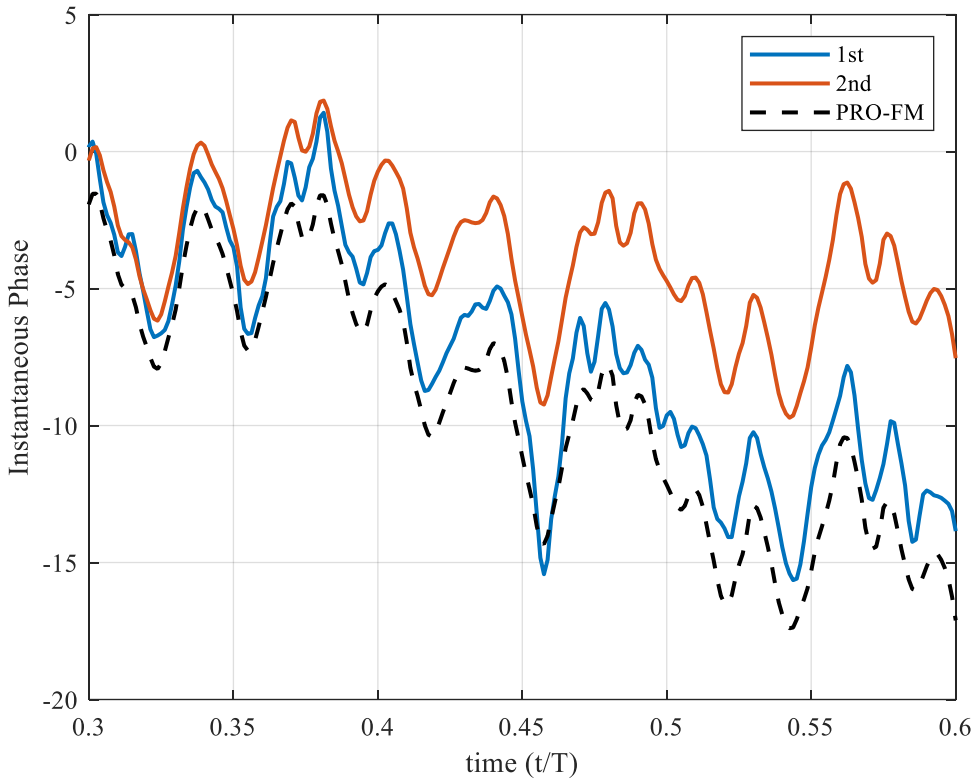

Figure 4-24: Close-up section of instantaneous phase of a single waveform optimized for $L = 4$ over-coded first and second-order PCFM (individual waveforms shifted back to baseband) quasi-bases compared to PRO-FM initialization

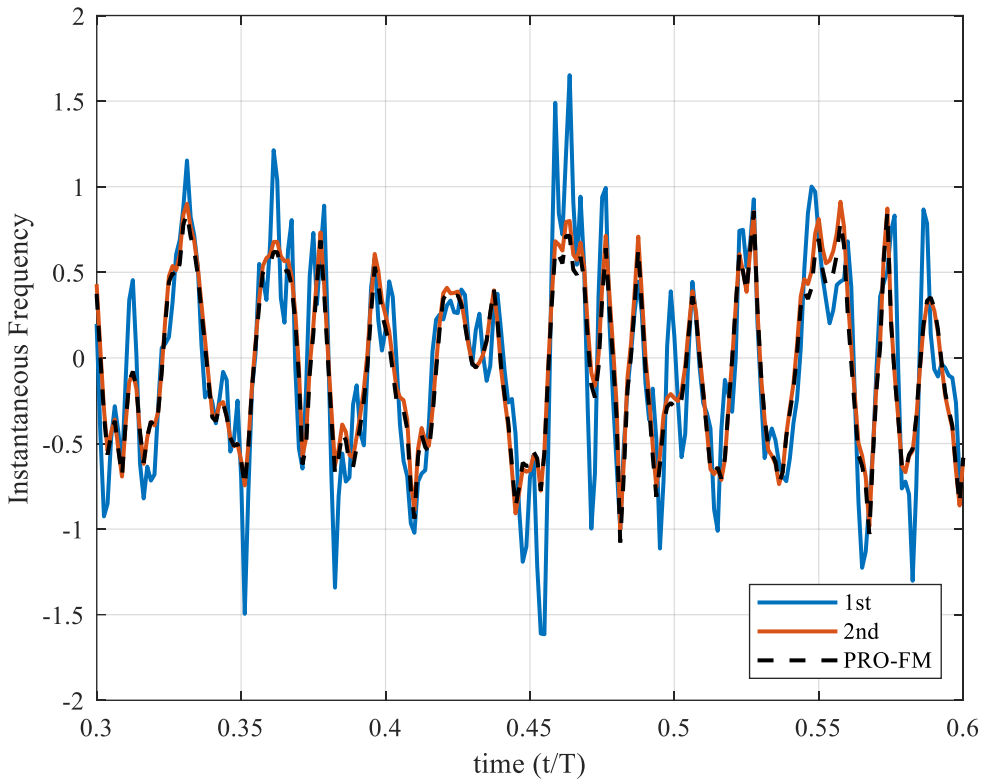

Figure 4-25: Close-up section of instantaneous frequency of a single waveform optimized for L=4 over-coded first and second-order PCFM (individual waveforms shifted back to baseband) quasi-bases compared to PRO-FM initialization

Chapter 5 Open-Air Experimental Results

All of the results shown thus far, are a great starting point, but they are simulated. We want to ensure that the resulting optimized waveforms are physically realizable, therefore, the final step is evaluating them experimentally. The optimized waveforms were first interleaved to guarantee that the illuminated environment was almost identical for each quasi-basis type. To test the robustness of the physical implementation, we first need to perform interpolation via spline interpolation of the phase to a sample rate of 10 GSamples/sec that corresponds to the transmitter sampling frequency. The resulting interpolated waveform was then digitally upconverted to a center frequency of 3.45 GHz with a pulse repetition interval of 22 μs.

Experimental data was collected in lovely Lawrence, KS, from the roof of Nichols Hall at the University of Kansas. The transmitter and receiver were directed towards the intersection of 23rd and Iowa. The interpolated waveforms were loaded on the Tektonic AWG7002A arbitrary waveform generator (AWG), passed through a bandpass filter and RF amplifier before being transmitted out. Once the receiver collected the returned signal, it was then passed through another bandpass filter and low noise amplifier, before being collected on the Rhode & Schwarz real-time spectrum analyzer at 200 MSamples/sec.

Using loopback data collected at the time of the experimental data collect, a match filter was then applied to the received signals to perform pulse compression. A -35-dB Taylor window was also applied in Doppler to alleviate Doppler spread. Since the radar system was on a stationary platform simple projection-based clutter cancellation was performed. This clutter cancellation technique forms a clutter matrix based on a given small radial velocity and performs singular value decomposition to calculate the projection matrix that the experimental data will be directed away from. Lastly, Doppler processing was performed.

As we saw previously, all three quasi-bases performed well in simulation. These next results will show that not surprisingly, all three quasi-bases also yield physically realizable waveforms that are amenable to hardware. Upon visual inspection, there is hardly a discernable difference between the resulting range-velocity maps illustrated in Figure 5-1 – Figure 5-3. Upon evaluation of the background floor, it is revealed that second-order is about 2-dB higher than first-order and Fourier. Recall that second-order was not completely converged following the optimization, which led to a higher sidelobe response that was shown in Figure 4-2 and Figure 4-3, thus the higher background floor.

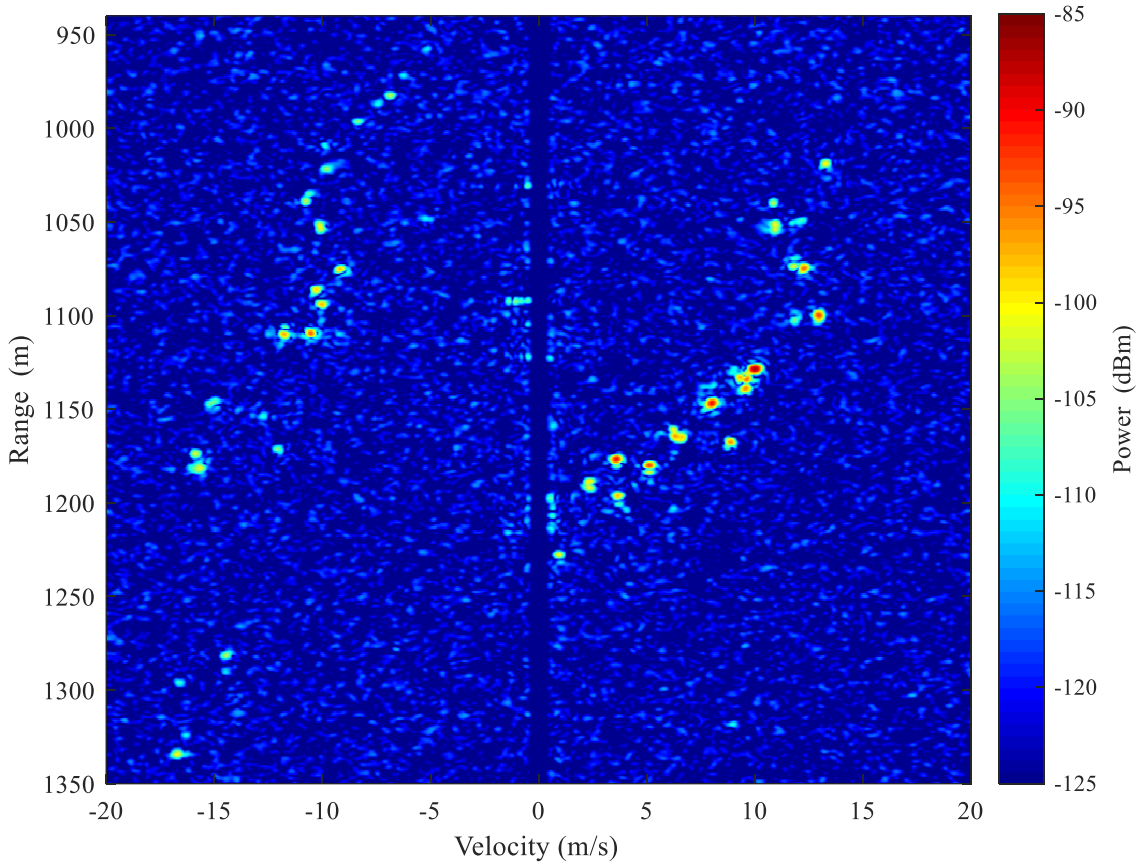

Figure 5-1: Open-air range-velocity response after simple clutter cancellation using 3000 unique first-order PCFM optimized waveforms

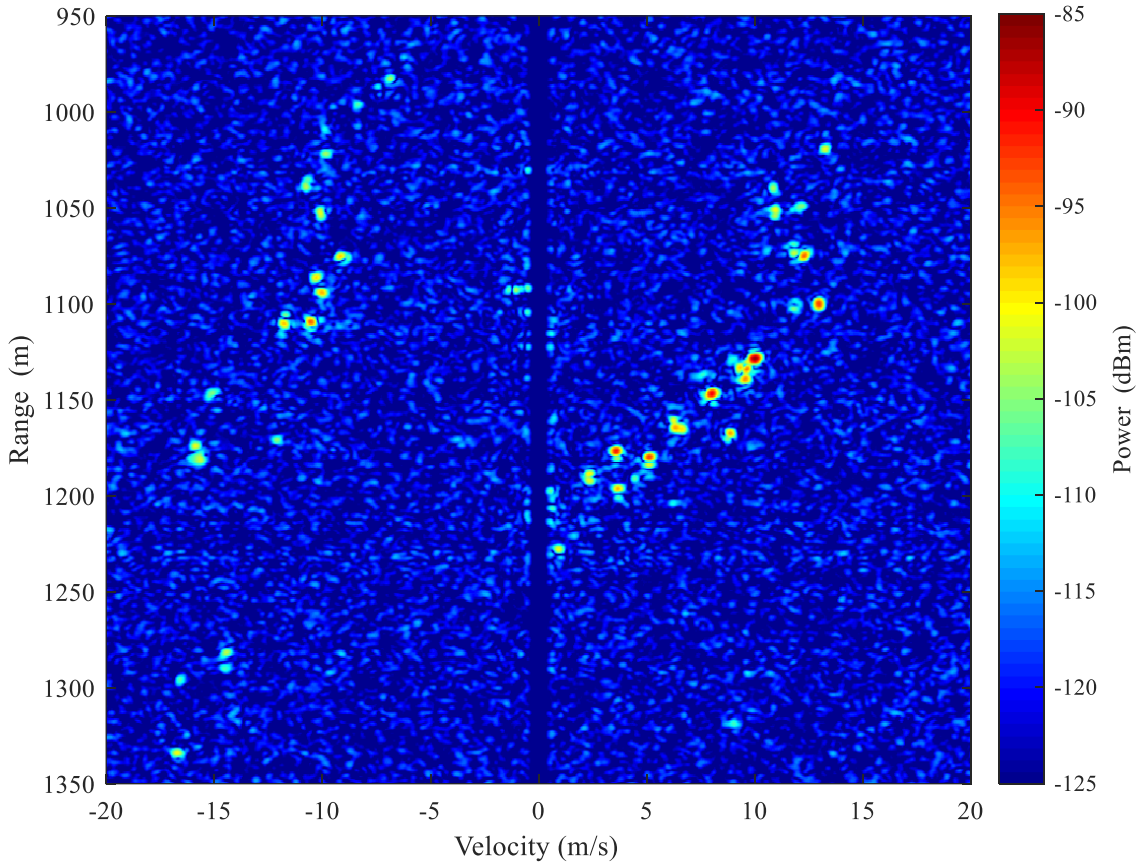

Figure 5-2: Open-air range-velocity response after simple clutter cancellation using 3000 unique second-order PCFM optimized waveforms

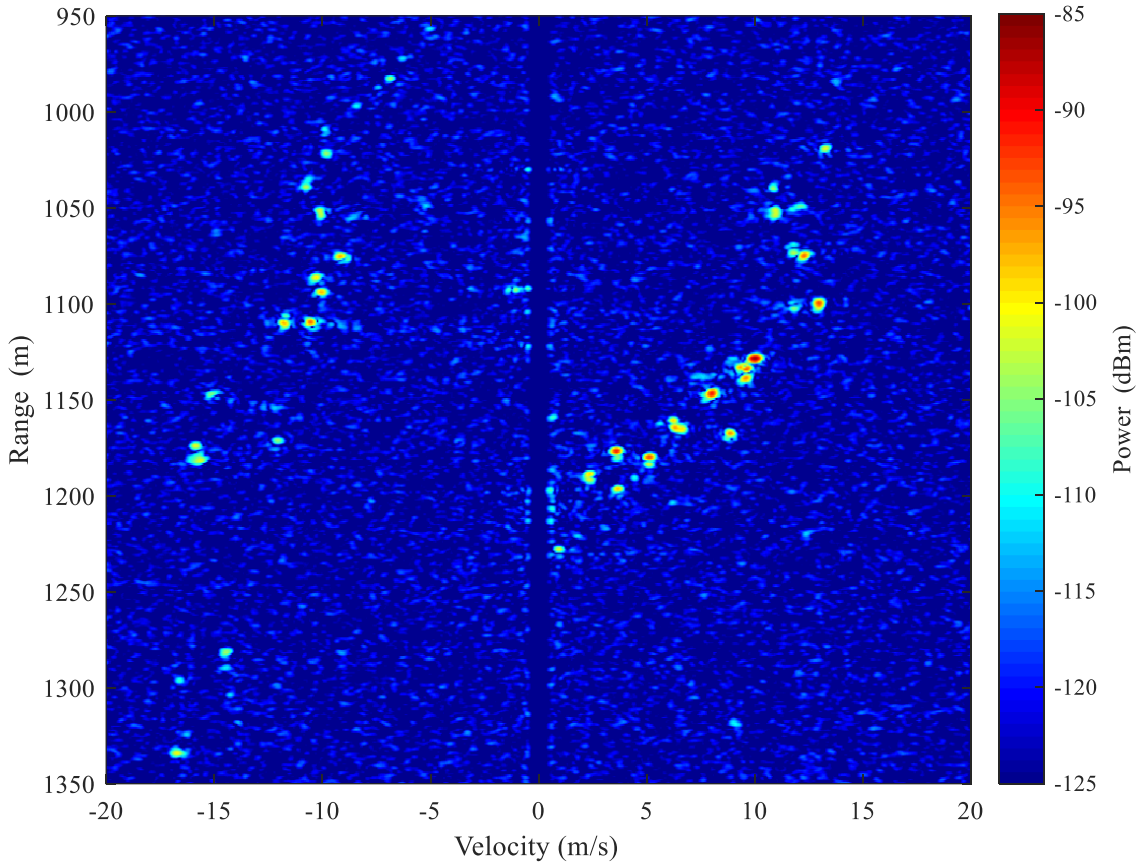

Figure 5-3: Open-air range-velocity response after simple clutter cancellation using 3000 unique Fourier optimized waveforms

Chapter 6 Conclusions and Future Work

Leveraging a recent *p*-norm based gradient-descent method for optimizing parameterized FM waveforms, the impact of selecting different quasi-bases for this parameterization was examined. Several results highlight them importance for a given quasi-basis to be sufficiently oversampled. Despite similarities in calculated 3 dB bandwidth between the quasi-bases examined, out-of-band spectral roll-off exposed the potential limitations of using higher over-coding factors in hardware, especially with first-order and Fourier quasi-basis. Despite the expectation that imposing range-straddling in the waveform design would implicitly impose spectral constraints for implementation

of an over-coded waveform, this was inherently not the case especially when employing the first-order and Fourier quasi-bases.

6.1 Future Work

From [16] the span of the parameters for first-order, second-order, and all the way up to third-order PCFM was derived. Initializing a first-order PCFM within the derived bounds of $[-\pi, +\pi]$, results in a waveform that is spectrally contained. But when we initialize second-order between that have a sense of "memory" or within the bounds of $[-2\pi, +2\pi]$, spectral containment is off the table. In fact in [16], there was the assumption of a constant frequency during each T_p interval that was made in order to determine the permissible second-order and third-order parameter values. This assumption is clearly not the case for second or higher-orders of PCFM. In fact, when PRO-FM is used to initialize the parameters of the second-order waveform often times the maximum and minimum parameters lie outside of these defined bounds. Indicating that more exploration into the appropriate bounds for initializing the second-order PCFM parameters needs to be done.

It was also the hope that by including range straddling into the waveform design process, this would implicitly impose spectral containment as was shown in [15]. While the range-straddling implemented through the derivation was shown to be successful in the case of the second-order quasi-basis case, it was not as successful for the first and Fourier quasi-bases. Experimentation using an ad-hoc approach to impose spectral containment was explored, where the autocorrelation became,

$$\mathbf{r} = \mathbf{A}^H\left[\left((\mathbf{A}\bar{\mathbf{s}}) \odot \mathbf{v}^* + (\mathbf{A}\bar{\mathbf{s}}) \odot \mathbf{v} + (\mathbf{A}\bar{\mathbf{s}})\right) \odot (\mathbf{A}\bar{\mathbf{s}})^*\right). \tag{6.1}$$

Therefore, by including both the forward and backward phase-shift vector, the relationship of conjugate-symmetry was maintained, allowing the use of the gradient derived in [12]. Early simulation indicated that this did implicitly provide a constraint on the spectrum. This was a very ad-hoc method for the optimization and it would be better if instead of using the sum of the phase-shifts in the autocorrelation, to use the three separate GISL cost functions for each phase-shift case.

References

[1] M. A. Richards, J. Scheer, W. A. Holm, and W. L. Melvin, *Principles of modern radar.* SciTech, 2010.

[2] M. A. Richards, *Fundamentals of radar signal processing*. McGraw-Hill Education, 2005.

[3] Swords, S. S., *Technical History of the Beginnings of RADAR*. Peter Peregrinus Ltd., London, 1986.

[4] S.D. Blunt, E.L. Mokole, "An overview of radar waveform diversity," *IEEE Aerospace & Electronic Systems Mag.*, vol. 31, no. 11, pp. 2-42, Nov. 2016

[5] B.M. Horton, "Noise-modulated distance measuring systems," *Proc. IRE*, vol. 47, no. 5, pp. 821-828, May 1959.

[6] S.R.J Axelsson, "Random noise radar/sodar with ultrawideband waveforms," *IEEE Trans. Geoscience & Remote Sensing*, vol. 45, no. 5, pp. 1099-1114, May 2007.

[7] T.B. Whiteley, D.J. Adrian, "Random FM autocorrelation fuze system," U.S. Patent #4,220,952, issued 2 Sept. 1980, filed 17 Feb. 1956.

[8] S.R.J. Axelsson, "Noise radar using random phase and frequency modulation," *IEEE Trans. Geoscience & Remote Sensing*, vol. 42, no. 11, pp. 2370-2384, Nov. 2004.

[9] L. Pralon, B. Pompeo, J.M. Fortes, "Stochastic analysis of random frequency modulated waveforms for noise radar systems," *IEEE Trans. Aerospace & Electronic Systems*, vol. 51, no. 2, pp. 1447-1461, Apr. 2015.

[10] S.D. Blunt, et al., "Principles & applications of random FM radar waveform design," *IEEE Aerospace & Electronic Systems Mag.*, vol. 35, no. 10, pp. 20-28, Oct. 2020

[11] S.D. Blunt, E.S. Perrins, eds. *Radar & Communication Spectrum Sharing*, SciTech Publishing, 2018.

[12] C.A. Mohr, P.M. McCormick, C.A. Topliff, S.D. Blunt, J.M. Baden, "Gradient-based optimization of PCFM radar waveforms," *IEEE Trans. Aerospace & Electronic Systems*, vol. 57, no. 2, pp. 935-956, Apr. 2021.

[13] N. Levanon, E. Mozeson, *Radar Signals*. John Wiley & Sons, 2004.

[14] S.D. Blunt, M. Cook, J. Jakabosky, J.D. Graaf, E. Perrins, "Polyphase-coded FM (PCFM) radar waveforms, part I: implementation," *IEEE Trans. Aerospace & Electronic Systems*, vol. 50, no. 3, pp. 2218-2229, July 2014.

[15] P.M. McCormick, S.D. Blunt, "Gradient-based coded-FM waveform design using Legendre polynomials," *IET Intl. Conf. Radar Systems*, Belfast, UK, Oct. 2017.

[16] P.S. Tan, J. Jakabosky, J. Stiles, S. Blunt, "Higher-order implementations of polyphase-coded FM radar waveforms," *IEEE Trans. Aerospace & Electronic Systems*, vol. 55, no. 6, pp. 2850-2870, Dec. 2019.

[17] B. White, M.B. Heintzelman, S.D. Blunt, "Alternative 'bases' for gradient-based optimization of parameterized FM radar waveforms," *IEEE Radar Conf.*, San Antonio, TX, May 2023.

[18] J. Jakabosky, S. D. Blunt, and B. Himed, "Optimization of "over-coded" radar waveforms," in 2014 IEEE Radar Conference, pp. 1460–1465, May 2014

[19] C.-D. Chung, S.-M. Cho, "Constant-envelope orthogonal frequency division multiplexing modulation," *Proc. APCC/OECC*, Beijing, China, Oct. 1999.

[20] S.C. Thompson, A.U. Ahmed, J.G. Proakis, J.R. Zeidler, "Constant envelope OFDM phase modulation: spectral containment signal space properties and performance," *IEEE Military Communications Conf.*, Monterey, CA, Oct./Nov. 2004.

[21] S.C. Thompson, J.P. Stralka, "Constant envelope OFDM for power-efficient radar and data communications," *Intl. Waveform Diversity & Design Conf.*, Kissimmee, FL, Feb. 2009.

[22] E.R. Biehl, C.A. Mohr, B. Ravenscroft, S.D. Blunt, "Assessment of constant envelope OFDM as a class of random FM radar waveforms," *IEEE Radar Conf.*, Florence, Italy, Sept. 2020.

[23] D.A. Hague, "Adaptive transmit waveform design using multitone sinusoidal frequency modulation," *IEEE Trans. Aerospace & Electronic Systems*, vol. 57, no. 2, pp. 1274-1287, April 2021.

[24] D.G. Felton, D.A. Hague, “Characterizing the ambiguity function of the constant-envelope OFDM waveforms,” *IEEE Radar Conf.*, San Antonio, TX, May 2023.

[25] T.J. Kramer, E.R. Biehl, M.B. Heintzelman, S.D. Blunt, E.D. Steinback, “Compact parameterization of nonrepeating FMCW waveforms,” *IEEE Radar Conf.*, San Antonio, TX, May 2023.

[26] E. Ghadimi, R. Feyzmahdavian, M. Johansson, “Global convergence of the heavy-ball method for convex optimization,” *European Control Conf.*, Linz, Austria, July 2015.

[27] P.M. McCormick, S.D. Blunt, “Nonlinear conjugate gradient optimization of polyphase-coded FM radar waveforms,” In *Proc*. *IEEE Radar Conf.*, Seattle, WA, USA, May 2017.

[28] J.B. Anderson, T. Aulin, C. Sunberg, *Digital Phase Modulation*. Plenum Press, 1986.

[29] D.G. Felton, D.A. Hague, “Gradient-based optimization of constant envelope OFDM waveforms,” *IEEE Radar Conf.*, San Antonio, TX, May 2023.

[30] K.S. Shanmugan and A.M. Breipohl, *Random signal: detection, estimation, and data analysis*. Wiley, 1988

[31] D.A. Hague, "Transmit waveform design using Multi-Tone Sinusoidal Frequency Modulation," *IEEE Radar Conf*, Seattle, WA, May 2017.

[32] J.W. Brown, R.V. Churchill, *Complex Variables and Applications*, New York, NY, McGraw-Hill, 1996.

[33] R. Remmert, *Theory of Complex Functions*, Trans. R.B. Burckel, Springer-Verlag New York, New York, NY, 1991.

[34] S.D. Blunt, J. Jakabosky, M. Cook. J. Stiles, S. Seguin, E.L. Mokole, “Polyphase-coded FM (PCFM) radar waveforms, part II: optimization,” *IEEE Trans. Aerospace & Electronic Systems*, vol. 50, no. 3, pp. 2230-2241, July 2014.

[35] J. Jakabosky, S.D. Blunt, B. Himed, “Spectral-shape optimized FM noise radar for pulse agility,” *IEEE Radar Conf.*, Philadelphia, PA, May 2016.

[36] C.A. Mohr, P.M. McCormick, S.D. Blunt, C. Mott, “Spectrally-efficient FM noise radar waveforms optimized in the logarithmic domain,” *IEEE Radar Conf.*, Oklahoma City, OK, Apr. 2018.

[37] C.A. Mohr, S.D. Blunt, “Designing random FM radar waveforms with compact spectrum,” *IEEE Intl. Conf. Acoustics, Speech & Signal Processing*, Toronto, Canada, June 2021.

[38] C. A. Mohr, S. D. Blunt, "FM Noise Waveforms Optimized According to a Temporal Template Error (TTE) Metric," *IEEE Radar Conf.*, Boston, MA, Apr. 2019.

[39] C.C. Jones, C.A. Mohr, P.M. McCormick, S.D. Blunt, “Complementary frequency modulated radar waveforms and optimized receive processing,” *IET Radar, Sonar & Navigation*, vol. 15, no. 7, pp. 708-723, Apr. 2021.

[40] C. A. Mohr, S. D. Blunt, "Design and Generation of Stochastically Defined, Pulsed FM Noise Waveforms," *IEEE Intl. Radar Conf.*, Toulon, France, Sept. 2019.

[41] M.B. Heintzelman, T.J. Kramer, S.D. Blunt, “Experimental evaluation of super-Gaussian-shaped random FM waveforms,” *IEEE Radar Conf.*, New York City, NY, Mar. 2022.

[42] J. Nocedal, S. Wright, *Numerical Optimization*. Vienna, Austria, Springer, 2006.

[43] A. M. Klein and M. T. Fujita, "Detection Performance of Hard-Limited Phase-Coded Signals," *IEEE Transactions on Aerospace and Electronic Systems*, vol. AES-15, no. 6, pp. 795-802, Nov. 1979.